

CHARACTERIZING AN UNCONVENTIONAL RESERVOIR WITH CONVENTIONAL  
SEISMIC DATA: A CASE STUDY USING SEISMIC INVERSION FOR THE VACA  
MUERTA FORMATION, NEUQUEN BASIN, ARGENTINA

by

Jorge E. Fernandez-Concheso M.

© Copyright by Jorge E. Fernandez-Concheso M., 2015

All Rights Reserved

A thesis submitted to the Faculty and the Board of Trustees of the Colorado School of Mines in partial fulfillment of the requirements for the degree of Master of Science (Geophysics).

Golden, Colorado

Date \_\_\_\_\_

Signed: \_\_\_\_\_  
Jorge E. Fernandez-Concheso M.

Signed: \_\_\_\_\_  
Dr. Thomas L. Davis  
Thesis Advisor

Golden, Colorado

Date \_\_\_\_\_

Signed: \_\_\_\_\_  
Dr. Terence K. Young  
Professor and Head  
Department of Geophysics

## ABSTRACT

Reservoir characterization for unconventional shale plays ideally requires multi-component, wide-azimuth, long-offset surface seismic data. These data are generally not available, especially in exploration or pre-development stages. Furthermore, it is common to have only a few wells over a large area, along with non-existent or scarce microseismic, engineering and production data. This thesis presents a methodology and workflow to deal with these circumstances of limited data availability. By using a narrow-azimuth, regional P-wave seismic volume and integrating it with wireline logs, cuttings and PLT data, the variability in the geomechanical properties of the Vaca Muerta Formation in Argentina's Neuquen Basin, and their relationships with lithology, stress state and total organic content, were analyzed.

Post-stack and pre-stack inversions were performed on the seismic volume. The uncertainties inherent from limited well control in the estimation of elastic properties were investigated using blind well testing. Sensitivity and error analysis was conducted on post-stack vs pre-stack derived P-impedance, the choice of the inversion algorithm (model-based vs sparse-spike) and the definition of the low frequency model (simple kriging model vs complex model derived from multi-attribute stepwise regression) were examined. Also, the use of isotropic AVA equations to approximate the anisotropic (VTI) behaviour of the reservoir was evaluated, using estimates of Thomsen parameters and simple AVA modelling.

The integration of the inversion results with the petrophysical analysis and the mechanical stratigraphy work by Bishop (2015), suggests that the rock composition has the largest influence on the geomechanical behaviour of the reservoir. Overpressure is also a major driving factor in that it controls changes in elastic properties. Bishop's cluster analysis was used to identify good quality rock classes. The probabilistic interpretation of these rock classes from seismic inversion provides a quantitative measure of uncertainty and guides the selection of potential drilling targets.

## TABLE OF CONTENTS

ABSTRACT . . . . .	iii
LIST OF FIGURES . . . . .	vii
LIST OF TABLES . . . . .	xiv
LIST OF ABBREVIATIONS . . . . .	xv
ACKNOWLEDGMENTS . . . . .	xvii
DEDICATION . . . . .	xix
CHAPTER 1 INTRODUCTION . . . . .	1
1.1 Objectives . . . . .	3
1.2 The Neuquen Basin . . . . .	3
1.2.1 Basin evolution . . . . .	4
1.2.2 Regional structure and tectonics . . . . .	5
1.2.3 The Quintuco . . . . .	6
1.2.4 The Vaca Muerta . . . . .	7
1.3 Study area and data available . . . . .	9
1.3.1 Seismic data . . . . .	10
1.3.2 Well data . . . . .	12
1.4 Previous studies . . . . .	13
1.5 Methodology of this work . . . . .	17
CHAPTER 2 DATA PRE-CONDITIONING . . . . .	18
2.1 Well log quality control . . . . .	18

2.2	Synthetic log generation . . . . .	19
2.3	Pre-stack seismic gather conditioning . . . . .	20
2.4	Angle stacks and data alignment . . . . .	21
2.5	Acquisition footprint removal . . . . .	24
2.6	Summary . . . . .	25
CHAPTER 3 SEISMIC INVERSION . . . . .		28
3.1	Theory . . . . .	29
3.1.1	Post-stack and pre-stack inversion . . . . .	30
3.1.2	Sparse-spike and model-based inversion . . . . .	31
3.2	Stacked data interpretation . . . . .	35
3.3	Low frequency model . . . . .	39
3.3.1	Standard model . . . . .	40
3.3.2	Complex model . . . . .	42
3.3.3	Qualitative comparison . . . . .	43
3.4	Post-stack inversion . . . . .	45
3.4.1	Well tie and wavelet estimation . . . . .	45
3.4.2	Inversion parameters . . . . .	47
3.5	Pre-stack inversion . . . . .	50
3.5.1	Well ties and angle-dependent wavelet estimation . . . . .	51
3.5.2	Inversion parameters . . . . .	51
3.6	Inversion results and quality control . . . . .	52
3.7	Summary . . . . .	62
CHAPTER 4 SENSITIVITY ANALYSIS OF INVERSION RESULTS . . . . .		66

4.1	Post-stack versus pre-stack P-impedance . . . . .	66
4.2	CSSI versus model-based inversion . . . . .	68
4.3	Standard LFM versus Complex LFM . . . . .	72
4.4	Effect of VTI anisotropy in AVO inversion . . . . .	75
4.4.1	Estimation of Thomsen parameters . . . . .	76
4.4.2	Reflectivity modelling for the Lower Vaca Muerta-Tordillo interface . . .	79
CHAPTER 5 INTERPRETATION AND INTEGRATION OF INVERSION RESULTS . . . . .		81
5.1	Relationships between elastic parameters, mineralogy and organic content . . .	81
5.2	Integration with mechanical stratigraphy . . . . .	87
5.2.1	Rock class properties . . . . .	88
5.2.2	Rock class probability from seismic inversion volumes . . . . .	90
5.3	Link of velocities with effective stress/pore pressure . . . . .	95
5.4	Interpretation of good quality rock classes . . . . .	98
CHAPTER 6 CONCLUSIONS AND RECOMMENDATIONS . . . . .		104
6.1	Recommendations for future research . . . . .	105
REFERENCES CITED . . . . .		108

## LIST OF FIGURES

Figure 1.1	Location map of the Neuquen Basin, along with the most notable hydrocarbon basins in the southern part of South America . . . . .	4
Figure 1.2	Stratigraphic column of the Neuquen Basin, highlighting the Quintuco and Vaca Muerta Formations. Modified from Howell et al. . . . .	5
Figure 1.3	Top: Map of the Neuquen Basin showing the location of four main zones classified by stress regime. Bottom right: table with associated stress gradients for each zone. Modified from Garcia et al. . . . .	7
Figure 1.4	Schematic NW-SE section of the Central Neuquen Basin, showing the sequence geometries of the carbonate ramp, and prograding clinoforms of the Quintuco and Vaca Muerta . . . . .	8
Figure 1.5	Type Log of the Quintuco and Vaca Muerta units in the study area. . . .	10
Figure 1.6	Map of RCP study area. The red polygon encloses the Wintershall block, and the blue polygon encompasses the area of the seismic survey. .	11
Figure 1.7	(a) Map of kerogen fraction distribution derived from pre-stack inversion and petrophysical logs . (b) Seismic cross-section color coded by the zones derived from the LMR rock mechanics template, showing a proposed well location . . . . .	14
Figure 1.8	3D view of modelled mechanical clusters for the Quintuco and Vaca Muerta . . . . .	15
Figure 1.9	Cross section of P-impedance volume, showing geobodies of clusters 1 and 2, interpreted as high quality rock. Montney Shale, Pouce Coupe Field, Canada . . . . .	16
Figure 1.10	Workflow of the research presented in this thesis. . . . .	17
Figure 2.1	Histograms of elastic-property logs for the four wells in the Quintuco-Vaca Muerta interval. Left: bulk density. Center: compressional slowness. Right: shear slowness. . . . .	19

Figure 2.2	Crossplot of bulk density vs P-wave velocity for the Quintuco interval in wells A and C. The dotted black line represents the best-fit power-law trendline, and the corresponding equation and correlation value are shown in the box on the bottom right. . . . .	20
Figure 2.3	Pre-stack migrated offset gathers around Well A. (a) Original data. (b) Data after muting and Radon de-noising. (c) Improved data after RMO, showing flatter events for AVO inversion. . . . .	21
Figure 2.4	(a) Inline plot of the migration velocity field used for the offset-incidence angle conversion of the pre-stack gathers. (b) Angle gathers around Well A. Traces go from 2 to 44 degrees, in 2 degree increments. Note the lack of data from 38 to 44 degrees close to the base of the Vaca Muerta. . . . .	22
Figure 2.5	Inlines of the four sub-stacks generated for pre-stack simultaneous inversion. . . . .	23
Figure 2.6	Inlines of time-shift volumes applied to the Near-Mid, Mid-Far and Far stack, with the Near stack as the benchmark volume. Negative values indicate an shift upward; positive values represent a downward shift. . . .	24
Figure 2.7	Time slices of raw seismic amplitudes in the northeastern part of the survey, extracted inside the Vaca Muerta interval. (a) Original data. Note the striping pattern in the east-west and north-south directions. (b) Data after application of the Footprint Removal process. . . . .	26
Figure 3.1	Schematic representation of the convolutional model . . . . .	29
Figure 3.2	Generalized workflows for seismic inversion. Top: post-stack. Bottom: pre-stack. Modified from Dueñas. . . . .	32
Figure 3.3	Comparison of trace-based vs model-based seismic inversion workflows . .	33
Figure 3.4	Reference inline of full stack seismic data with main horizons interpreted. The relative location of this section is depicted by the thick black line on the base map to the right. . . . .	36
Figure 3.5	Time structure map of the Top Quintuco. . . . .	37
Figure 3.6	Time structure map of the Lower Quintuco. . . . .	37
Figure 3.7	Time structure map of the Top Vaca Muerta. . . . .	38
Figure 3.8	Time structure map of the Middle Vaca Muerta. . . . .	38

Figure 3.9	Time structure map of the Base Vaca Muerta. . . . .	39
Figure 3.10	2D section plot of well weights for global kriging (range=30,000 m). . . . .	42
Figure 3.11	Stepwise regression error plot for the P-impedance model. The 2 in the x-axis means the use of attributes 1 and 2 listed on the right, the 3 means the use of attributes 1, 2 and 3, and so on. . . . .	44
Figure 3.12	Stepwise regression error plot for the S-impedance model. . . . .	44
Figure 3.13	Inline of the P-impedance low-frequency models. Left: complex model. Right: standard model. . . . .	45
Figure 3.14	Inline of the S-impedance low-frequency models. Left: complex model. Right: standard model. . . . .	46
Figure 3.15	Wavelets estimated for the zero-offset well tie for post-stack inversion. Red: Well A wavelet. Blue: Well B wavelet. Black: multi-well wavelet. . . . .	47
Figure 3.16	Full stack seismic-well tie for Well A. . . . .	48
Figure 3.17	Full stack seismic-well tie for Well B. . . . .	48
Figure 3.18	Full stack seismic-well tie for Well C. . . . .	49
Figure 3.19	Full stack seismic-well tie for Well D. . . . .	49
Figure 3.20	Bandwidth of the full stack. The high-cut filter applied to the low-frequency model is shown in red, and the bandpass filter applied to the post-stack inversion result is shown in cyan. The merge cut-off frequency is 10 Hz. . . . .	50
Figure 3.21	Wavelets estimated for each of the four partial stacks. Near stack: blue. Near-Mid stack: red. Mid-Far stack: green. Far stack: black. . . . .	52
Figure 3.22	Well ties for partial angle stacks in Well A. . . . .	53
Figure 3.23	Well ties for partial angle stacks in Well B. . . . .	53
Figure 3.24	Well ties for partial angle stacks in Well C. . . . .	54
Figure 3.25	Well ties for partial angle stacks in Well D. . . . .	54

Figure 3.26	Bandwidth of the Near stack. The high-cut filter applied to the low frequency model is shown in red, and the bandpass filter applied to the pre-stack inversion result is shown in cyan. The merge cut-off frequency is 10 Hz. . . . .	55
Figure 3.27	Maps of average seismic-synthetic correlation for the inversion window (Quintuco and Vaca Muerta) on each partial angle stack. . . . .	56
Figure 3.28	Inline of band-limited inverted P-impedance (10-70 Hz). Left: post-stack. Right: pre-stack. The well log has a 10-70 Hz bandpass filter. . . . .	57
Figure 3.29	Inline section of band-limited inverted S-impedance (10-70 Hz). The well log has a 10-70 Hz bandpass filter. . . . .	58
Figure 3.30	Inline of full-bandwidth inverted P-impedance (0-70 Hz). Left: post-stack. Right: pre-stack. The well log has a 70 Hz high-cut filter. . . . .	59
Figure 3.31	Inline of full-bandwidth inverted S-impedance (0-70 Hz). The well log has a 70 Hz high-cut filter. . . . .	59
Figure 3.32	Pseudo-logs extracted from the full-bandwidth P-impedance post-stack (blue curves) and pre-stack inversion (red curves), compared with the high-cut (70 Hz) filtered well logs (black curves) for all wells. . . . .	60
Figure 3.33	Pseudo-logs extracted from the band-limited P-impedance post-stack (blue curves) and pre-stack inversion (red curves), compared with the bandpass(10-70 Hz) filtered well logs (black curves) for all wells. . . . .	60
Figure 3.34	Pseudo-logs extracted from the full-bandwidth S-impedance inversion (blue curves), compared with the high-cut (70 Hz) filtered well logs (black curves) for all wells. . . . .	61
Figure 3.35	Pseudo-logs extracted from the band-limited S-impedance inversion (blue curves), compared with the bandpass(10-70 Hz) filtered well logs (black curves) for all wells. . . . .	62
Figure 3.36	Maps of extracted P-impedance from post-stack and pre-stack inversion, for three main levels of the Vaca Muerta. . . . .	63
Figure 3.37	Maps of extracted S-impedance for three main levels of the Vaca Muerta. . . . .	64
Figure 4.1	Blind well tests for post-stack P-impedance inversion (blue curves) and pre-stack P-impedance inversion (red curves) compared with the high-cut filtered P-impedance from the well logs (black curves). . . . .	67

Figure 4.2	RMS errors of blind well tests for post-stack and pre-stack P-impedance inversion. . . . .	68
Figure 4.3	Blind well tests for model-based Poisson's ratio (blue curves) and CSSI Poisson's ratio (red curves) compared with the high-cut filtered Poisson's ratio from the well logs (black curves). . . . .	70
Figure 4.4	RMS errors of blind well tests for model-based and CSSI derived Poisson's ratio. . . . .	70
Figure 4.5	Blind well tests for model-based $E\rho$ (blue curves) and CSSI $E\rho$ (red curves) compared with the high-cut filtered $E\rho$ from the well logs (black curves). . . . .	71
Figure 4.6	RMS errors of blind well tests for model-based and CSSI derived $E\rho$ . . . . .	71
Figure 4.7	Blind well tests for Poisson's ratio obtained from inversion with the standard LFM (red curves) and the complex LFM (blue curves) compared with the high-cut filtered Poisson's ratio from the well logs (black curves). . . . .	73
Figure 4.8	RMS errors of blind well tests for Poisson's ratio from the standard and complex low frequency models. . . . .	73
Figure 4.9	Blind well tests for $E\rho$ obtained from inversion with the standard LFM (red curves) and the complex LFM (blue curves) compared with the high-cut filtered $E\rho$ from the well logs (black curves). . . . .	74
Figure 4.10	RMS errors of blind well tests for $E\rho$ from the standard and complex low frequency models. . . . .	74
Figure 4.11	Logs of Thomsen parameters for wells C and D. Orange: delta. Blue: epsilon. . . . .	78
Figure 4.12	Comparison between reflection coefficient curves for the Lower Vaca Muerta-Tordillo interface model. Blue: isotropic. Orange: anisotropic. Black: isotropic with $0.9*Vs$ . . . . .	80
Figure 5.1	Logs of clay, carbonate and quartz mineral volumes, with calibration data from XRD (black dots). (a) Well B (from ECS logs). (b) Well A (from petrophysical relationships). . . . .	83
Figure 5.2	TOC logs with rock-eval calibration data (black dots). . . . .	84

Figure 5.3	Cross-plots of $V_p/V_s$ (y-axis) vs P-impedance (x-axis), color coded by (a) carbonate volume, (b) quartz volume, (c) clay volume, and (d) TOC. . . . .	85
Figure 5.4	Top left: P-impedance vs carbonate volume. Top right: P-impedance vs quartz volume. Bottom: P-impedance vs TOC. The colour code is red for the Upper Vaca Muerta and blue for the Lower Vaca Muerta. . . . .	86
Figure 5.5	Graphical representation of the advantage of using rock class classification for property predictions vs global correlations . . . . .	87
Figure 5.6	Cluster analysis results for the Vaca Muerta . . . . .	88
Figure 5.7	Distributions of $E\rho$ by rock class. . . . .	89
Figure 5.8	Distributions of Poisson's ratio by rock class. . . . .	90
Figure 5.9	Distributions of quartz volume by rock class. . . . .	91
Figure 5.10	Distributions of carbonate volume by rock class. . . . .	91
Figure 5.11	Distributions of clay volume by rock class. . . . .	92
Figure 5.12	Distributions of TOC by rock class. . . . .	92
Figure 5.13	Cross-plot of P-impedance vs $V_p/V_s$ at seismic resolution, color coded by rock class, and associated PDF's for each rock class. . . . .	94
Figure 5.14	Inline section showing most probable rock class volume and comparison with Well A lithology log. Areas in black are unclassified. . . . .	95
Figure 5.15	NCT (blue curve) with lithology and porosity corrected P-wave velocity (orange curve). The stars point to the interpreted onset of overpressure. The dashed black line represent the Quintuco-Vaca Muerta boundary. . . . .	98
Figure 5.16	Calculated Eaton pore pressure profiles for the Vaca Muerta interval. . . . .	99
Figure 5.17	Distributions of Eaton pore pressure by rock class. . . . .	100
Figure 5.18	PLT data with oil production percentages per stage (left track), and rock classes from cluster analysis (right track) for Well A. Note the high proportion of cluster 7 (red) in the upper stage, and the predominance of cluster 5 (orange) in the lower stage with high production, both highlighted by the black boxes. . . . .	101

Figure 5.19 Left: arbitrary line of most probable rock class intersecting Well E, aligned with the interpreted minimum horizontal stress direction. Right: probability of rock class 7, with proposed well trajectories in dark blue. 102

Figure 5.20 Left: arbitrary line of most probable rock class intersecting Well F, aligned with the interpreted minimum horizontal stress direction. Right: probability of rock class 5, with proposed well trajectories in dark blue. 103

## LIST OF TABLES

Table 1.1	Ranges in reservoir properties of the Vaca Muerta, compared with other important shale plays in the US . . . . .	9
Table 1.2	Seismic acquisition parameters. . . . .	11
Table 1.3	Well database for the study area. . . . .	13
Table 3.1	LFM blind well test results for standard interpolation methods. . . . .	41
Table 3.2	Post-stack inversion parameters. . . . .	47
Table 3.3	Pre-stack inversion parameters. . . . .	55
Table 4.1	Average properties of the Lower Vaca Muerta and Tordillo obtained from the well logs. . . . .	79
Table 5.1	Prior probabilities for each rock class. . . . .	93
Table 5.2	Comparison of measured and modelled elastic parameters for each rock class. Density is in g/cc and velocities are in m/s. . . . .	96
Table 5.3	Vp/Vs ratio of data compared with modelled and fluid substituted Vp/Vs for clusters 4 and 7. . . . .	99

## LIST OF ABBREVIATIONS

Amplitude Variation with Angle . . . . .	AVA
Amplitude Variation with Offset . . . . .	AVO
Computarized Tomography . . . . .	CT
Constrained Sparse Spike Inversion . . . . .	CSSI
Diagnostic Fracture Injection Test . . . . .	DFIT
Elemental Capture Spectroscopy . . . . .	ECS
Energy Information Administration . . . . .	EIA
Facies and Fluid Probability . . . . .	FFP
Lambda-Mu-Rho . . . . .	LMR
Low Frequency Model . . . . .	LFM
Mechanical Earth Model . . . . .	MEM
Normal Compaction Trend . . . . .	NCT
Normal Move-Out . . . . .	NMO
Oil-Based MicroImager . . . . .	OBMI
Pre-Stack Time Migration . . . . .	PSTM
Probability Density Function . . . . .	PDF
Production Logging Tool . . . . .	PLT
Quality Control . . . . .	QC
Reservoir Characterization Project . . . . .	RCP
Residual Move-Out . . . . .	RMO

Root-Mean Square . . . . .	RMS
Total Organic Carbon . . . . .	TOC
Ultrasonic Borehole Imager . . . . .	UBI
Vertical Seismic Profile . . . . .	VSP
Vertical Transverse Isotropy . . . . .	VTI
X-Ray Diffraction . . . . .	XRD

## ACKNOWLEDGMENTS

First of all, I want to thank Dr. Tom Davis for giving me the opportunity to have such a high-quality educational and research experience. I feel truly privileged to have worked under his tutelage for the last two years. He has left a lasting legacy of excellence with RCP. Now I wish him the best in his well-deserved retirement. I would also like to acknowledge my committee members: Dr. Bob Benson, Dr. Steve Sonnenberg, Dr. Ken Lerner and David Curia, for their time and valuable comments.

This thesis would not have been possible without the gracious and kind help from Wintershall, who provided RCP with this excellent dataset, and also gave me the invaluable opportunity to intern with them during the summer of 2014. Thank you to Heather Davey, Bertrand Cuesta and Pablo Pateti, for very valuable technical discussions as well as some fun times in Kassel. A special acknowledgement to Christian Hanitzsch, who really went above and beyond to support me in every step of the way.

Thank you to the awesome Grateful Dead Bovine team. Kyla Bishop was my restless partner. Her outstanding technical skills and fun personality, made her always a pleasure to work with. With Paula Barbosa and Carlos Convers continuing the work, the Vaca Muerta project is in excellent hands moving forward.

I want to express my deepest gratitude to the staff from RCP and the Department. Thank you to Sue Jackson, Michelle Szobody, Justine Gomez and Renie Herrin, for truly making life much easier for us. A special acknowledgement to Sue, who also was vital with her motivation to move forward. Her work in RCP is really extraordinary.

Thank you to all my wonderful RCP and Geophysics colleagues and friends. I have no doubts that you all will be great leaders one day. Special thanks to Ben Andrews for helping me code the references in Latex, and to Esteban Diaz (Toto) who helped me correct the static shifts for the pre-stack gathers. Also, thanks to my South American gang from Mines,

for very fun times and giving me a little piece of home.

Thank you to FC International, Bodka Juniors and Colorado Cutthroats Baseball, for giving me the chance to play sports, have fun and keep my mental sanity.

Of course, none of this would have been possible without the support from my family in Venezuela and many other parts of the world. To my parents, sisters, grandparents, cousins, aunts, uncles, and my friends (who are the family I chose): the list of names is too long, but you all know who you are. Thanks for everything.

And last, but certainly, not least, thank you to my beautiful wife Antonella. Your love, compassion, good humour and wise counselling has carried me through this experience. You give meaning to my life, and I really look forward to growing old with you.

To the memory of Morelia, Elizabeth, Remedios, Aldo, Tito, JJ, Teresa and Audi

## CHAPTER 1

### INTRODUCTION

The success of unconventional shale plays in the United States and Canada in recent years has led to an increasing effort by national and independent oil companies to evaluate the potential of these self-sourced reservoirs in other locations. Perhaps the most promising shale play in the world outside of North America is the Vaca Muerta Formation in Argentina's Neuquen Basin.

According to the Energy Information Administration (EIA), Argentina ranks 3rd in the world in technically recoverable shale gas resources with 802 trillion cubic feet (behind the US and China). Also, with 27 billion barrels, it is in 4th place among all countries in technically recoverable shale oil resources (trailing only Russia, US, and China). The Vaca Muerta holds 308 trillion cubic feet of gas and 16.2 billion barrels of oil, representing 38.4 and 60 % of the country's shale gas and shale oil potential, respectively (EIA/ARI, 2013). These numbers show the great importance of this vast play in Argentina's energy future.

The work presented in this thesis was performed in the framework of a project that began in 2013, between the Reservoir Characterization Project (RCP) and Wintershall Holding GmbH. This integrated study focuses in the exploration, appraisal, and development of the Vaca Muerta in Wintershall's first own-operated block in the region. Data within the study area include a large 3D seismic survey and a wealth of information from a few wells consisting of full wireline log suites, image logs, cuttings, pressure, and production data.

Traditional RCP projects are undertaken well into the development stage and focus on optimizing production by monitoring either hydraulic fracturing for shale reservoirs (e.g., Niobrara-Codell in Wattenberg Field, Colorado) or enhanced oil recovery processes for conventional reservoirs (e.g., Paluxy-Tuscaloosa in Delhi Field, Louisiana). The Vaca Muerta project is unique for RCP in the sense that it is starting at a much earlier stage. Currently,

the field is in the "Technology Phase", with only one vertical well inside the block, two more vertical wells being drilled in mid-2015, and the first horizontal wells planned for 2016. Optimization is evidently not a key component at this point in time. Currently, the focus is beginning to understand the reservoir, reducing geological uncertainty, and identifying sweet spots to guide the placement of future wells for the later stages of development.

In this context, the use of 3D seismic for reservoir characterization poses interesting challenges. The available data are not optimal for unconventional reservoirs. The offset, and especially the azimuthal coverage is not suited for the study of anisotropy, necessary to measure the lateral variations of the *in-situ* stress field and the presence of natural fractures. Moreover, there are limitations in the availability of ancillary data for integration with the seismic. The well control is sparse. At this stage there are no microseismic or VSP surveys, and the engineering and production data are limited. This gives a good opportunity to understand how to make the most out of this high-quality dataset to assess uncertainty and build predictive power from the beginning of the life of an unconventional reservoir. The value of the workflow presented here is that it can be applied in other frontier shale plays around the world, with similar situations on data availability.

The main focus of this thesis is to describe the vertical and lateral variability of geomechanical properties in the reservoir and their relationship with lithology, stress state, and total organic carbon (TOC) content, through the use of post-stack and pre-stack seismic attributes and petrophysics/rock physics analysis. As this is a nascent project, there are no previous studies for this area. RCP researcher Kyla Bishop has conducted geologically focused studies on the well log data, working on natural fracture characterization with image logs and mechanical stratigraphy by the use of cluster analysis. Some results from this work are integrated with the seismic data in this thesis.

In this chapter, the objectives, location and geology of the reservoir, the data available, and the methodology employed in this work are presented. Chapter 2 describes the data pre-conditioning as a necessary step for a successful seismic inversion. Chapter 3 explains

the post-stack and pre-stack seismic inversion process performed. Chapter 4 explains the sensitivity analysis and blind well testing of different inversion parameters for geomechanical and reservoir properties, as an initial assessment of uncertainty. Chapter 5 shows the integration of the inversion results with the petrophysical analysis and mechanical stratigraphy. Chapter 6 includes the conclusions and recommendations drawn from this study.

## 1.1 Objectives

The specific objectives of this work are the following:

- To quantify the uncertainty inherent from limited well control in the estimation of elastic properties from seismic inversion through sensitivity analysis and blind well tests.
- To evaluate the effect of layer anisotropy in the Amplitude Variation with Angle (AVA) character of the reservoir, and its implications in an isotropic inversion.
- To predict lithology, TOC, stress state, and mechanical stratigraphy from seismic attributes, using petrophysical analysis and statistical techniques.

## 1.2 The Neuquen Basin

The Neuquen Basin is located in west central Argentina, on the eastern flank of the Andes mountain range (Figure 1.1). It covers an area of more than 120,000 km<sup>2</sup>, extending for approximately 700 km from north to south (Hogg, 1993). The basin is up to 4,000-m thick, and comprises continental and marine siliciclastics, carbonates, and evaporites, deposited under various basin styles (Howell et al., 2005). Although it has hosted active hydrocarbon exploration and production since the 1960s (Hogg, 1993), the advent of horizontal drilling and multi-stage hydraulic fracturing has given this basin new life in the past few years, the Vaca Muerta being the main reason for this uprise.

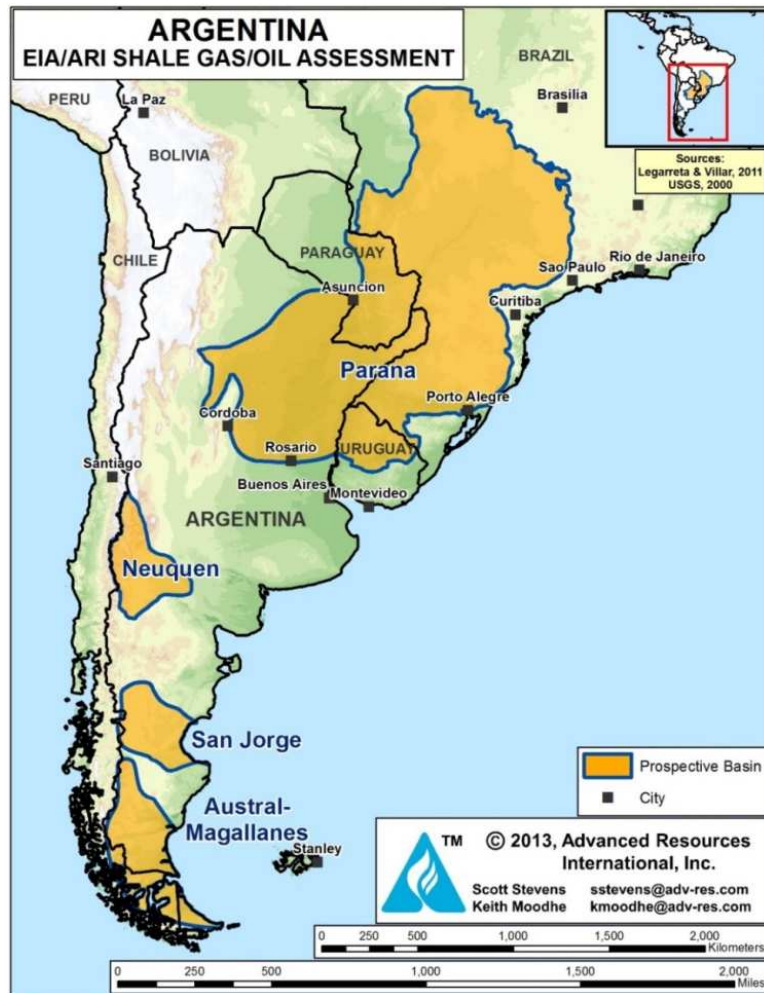


Figure 1.1: Location map of the Neuquen Basin, along with the most notable hydrocarbon basins in the southern part of South America (EIA/ARI, 2013).

### 1.2.1 Basin evolution

Howell et al. (2005) summarizes the complex history of the Neuquen Basin in three main stages:

1. Syn-rift stage: extensional tectonics and development of narrow, isolated depocenters (Late Triassic-Early Jurassic).
2. Post rift-stage: creation of an active subduction zone and associated back-arc subsidence within the basin. Responsible for most of the basin fill, including the deposition of the Vaca Muerta (Early Jurassic-Early Cretaceous)(Figure 1.2).

3. Compression and foreland basin stage: change to a shallow-dipping subduction zone, originating the transition to a compressional regime, inversion of previous extensional features and uplift of the foreland thrust belt (Late Cretaceous-Cenozoic).

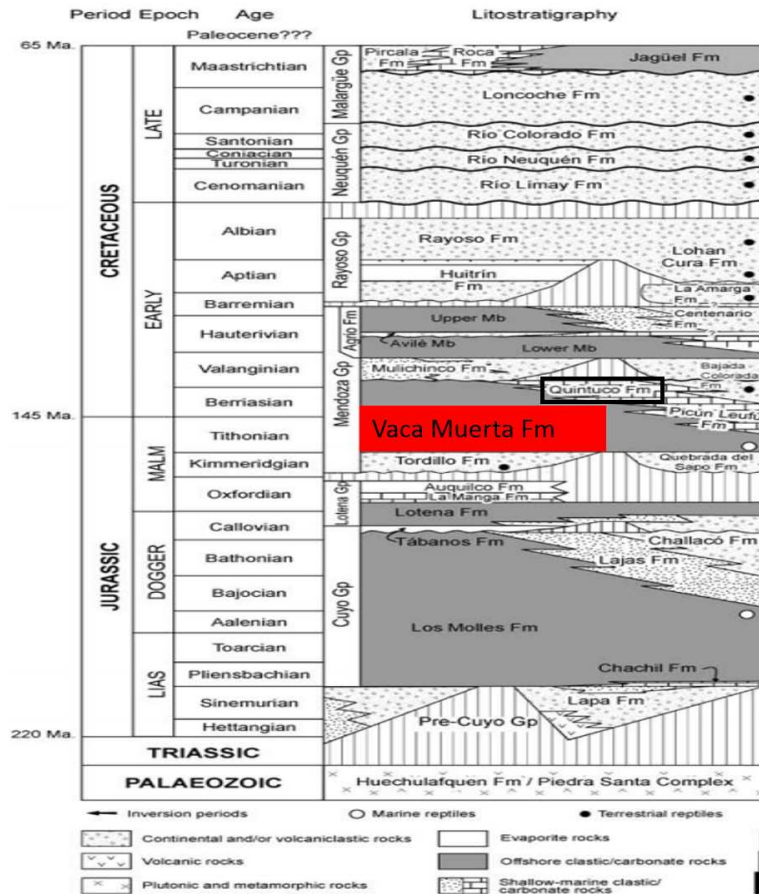


Figure 1.2: Stratigraphic column of the Neuquen Basin, highlighting the Quintuco and Vaca Muerta Formations. Modified from Howell et al. (2005).

### 1.2.2 Regional structure and tectonics

Resulting from the Andes orogeny that occurred in the Early Cenozoic, the western area of the basin shows more structural complexity, appearing as major thrust zones. The central and eastern parts of the basin are significantly less deformed structurally and have thicker sedimentary columns. This area, which holds most of the oil and gas fields in the basin, is known as the *embayment* (Garcia et al., 2013). This area shows structural

deformation mainly as the result of Mesozoic tectonics, mostly away from the influence of Andean tectonism, from the Oligocene onward. The main structures in the embayment are deep anticlinal structures parallel to the basin axis, and normal faults, mostly dipping to the north, which compose a series of antithetic basement blocks and rollovers in the upper sedimentary fill (Urien and Zambrano, 1994)

Understanding the regional *in-situ* stress field is of paramount importance in the study of unconventional shale plays. Towards the western part of the basin, the stress regime is strike-slip due to the compressional tectonic effect from the Andes. Moving to the east, the regime transitions from strike-slip to normal, and the horizontal stress anisotropy decreases. The direction of maximum horizontal stress is mainly east-west (Garcia et al., 2013).

Garcia et al. (2013) define four main zones in terms of stress state, which can be seen in Figure 1.3. Zone 4 is in a strike-slip regime and has the highest horizontal stress anisotropy. On the other hand, Zone 3 has the least stress anisotropy, belonging in a normal stress regime. Zones 1 and 2 are in the transition zone between strike-slip and normal stress conditions.

### 1.2.3 The Quintuco

The Quintuco Formation lies directly above the Vaca Muerta in the study area. Its composition includes different proportions of limestone, dolomite, anhydrite, and quartz/volcanic clastic sands (Hurley et al., 1995), deposited in a shallow marine environment (Figure 1.2). This formation has produced hydrocarbons for more than 40 years in the Neuquen Basin, as a conventional carbonate reservoir (Yrigoyen, 1993).

The Quintuco is very important in this study for various reasons. (a) Even though the Vaca Muerta is the main target interval, the Quintuco, as mentioned previously, is also known to be productive. Therefore, it may be an attractive secondary target. (b) In any geomechanical analysis, the overburden is important, and this thick formation will influence the stress state of the underlying Vaca Muerta. (c) The Quintuco is recognized to be the onset of overpressure, with pressure gradients up to 1 psi/ft (Garcia et al., 2013). These overpressures may represent serious drilling hazards.

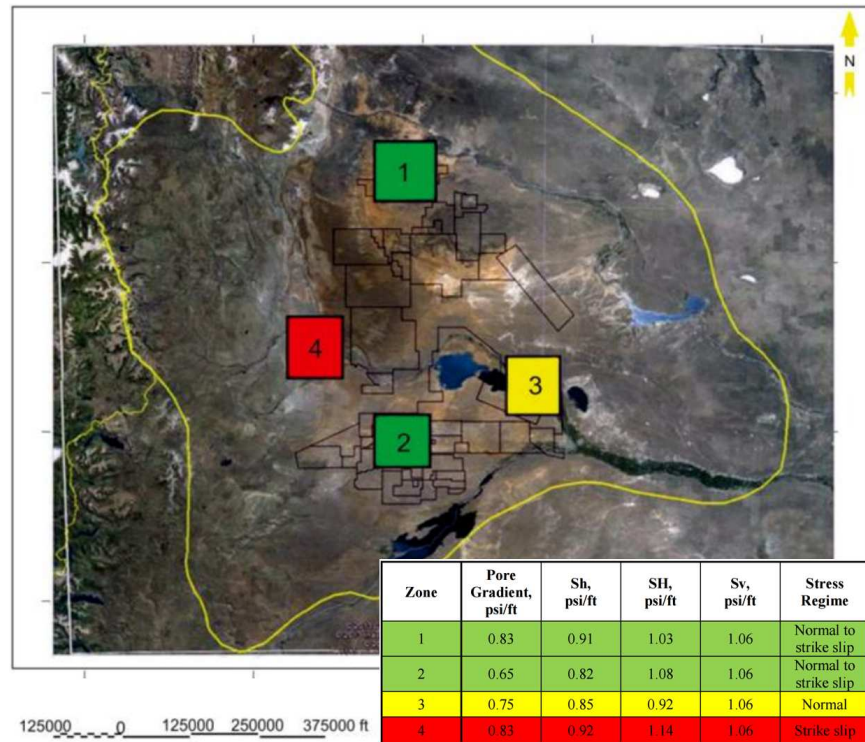


Figure 1.3: Top: Map of the Neuquen Basin showing the location of four main zones classified by stress regime. Bottom right: table with associated stress gradients for each zone. Modified from Garcia et al. (2013).

#### 1.2.4 The Vaca Muerta

The Vaca Muerta Formation has been recognized for years as the primary source rock for the producing conventional reservoir intervals in the Neuquen Basin, including the underlying Tordillo Formation (Figure 1.2). It is composed of organic-rich shales, limestones, and marls, deposited in a quick and widespread marine transgression started in the Early Tithonian (Legarreta and Uliana, 1991). According to Kietzmann et al. (2014), the deposition of the Vaca Muerta occurred in the context of a low-angle carbonate ramp. The central part of the basin shows a generalized sigmoid geometry, shown in Figure 1.4. The shallow marine carbonates of the Quintuco prograde into the deeper, more siliciclastic Vaca Muerta units. The base of the Vaca Muerta makes a sharp, conformable contact with the Tordillo. This is a clear and regionally widespread seismic marker.

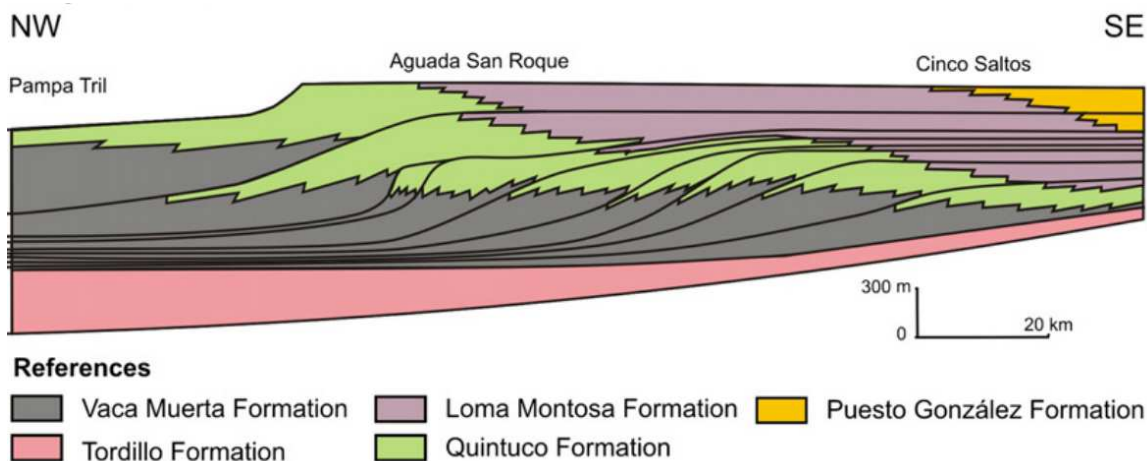


Figure 1.4: Schematic NW-SE section of the Central Neuquen Basin, showing the sequence geometries of the carbonate ramp, and prograding clinoforms of the Quintuco and Vaca Muerta (Kietzmann et al., 2014).

The Vaca Muerta was deposited under anoxic conditions, and contains high-quality amorphous organic matter, mostly Type I/II kerogen. The thermal maturity in the formation increases gradually from the east (oil-prone window) to the west (gas-prone window) of the basin (Legarreta and Villar, 2011). The study area is located in the oil window.

The thickness, depth, areal extent, thermal maturity, TOC, mineralogy, depositional environment, and pressure conditions of the Vaca Muerta Formation, make it a world-class unconventional resource play (Ejofodomi et al., 2013). Table 1.1 shows a comparison in important reservoir parameters between the Vaca Muerta and some of the major shale plays in the US. The data show that the Vaca Muerta ranks high in most items, especially in the net pay thickness and the overpressure represented by the pressure gradients. Therefore, it is clear that the reservoir quality of the Vaca Muerta is comparable or superior to that of its North American counterparts.

The matrix permeability ranges from hundreds of nanodarcies to tens of microdarcies. Natural fractures are present throughout the interval, and are believed to play a fundamental role in the production performance of the wells (Ejofodomi et al., 2013).

Table 1.1: Ranges in reservoir properties of the Vaca Muerta, compared with other important shale plays in the US (Askenazi et al., 2013).

	Barnett	Eagle Ford	Marcellus	Woodford	<b>Vaca Muerta</b>
Area (km <sup>2</sup> )	13,000	5,000	250,000	28,900	<b>30,000</b>
Depth (km)	2.0 - 2.6	1.2 - 4.2	1.2 - 2.6	1.8 - 3.4	<b>2 - 3.5</b>
Porosity (%)	4 - 5	4 -15	10 - 11	3 - 9	<b>4 - 12</b>
TOC (%)	3 - 6	4.5 - 5.5	3 - 12	0.6 - 1	<b>2 - 12</b>
Net pay (m)	15 - 60	25 - 100	15 - 60	35 - 67	<b>50 - 350</b>
Pressure gr. (psi/ft)	0.43 - 0.44	0.6	0.15 - 0.4	??	<b>0.6 - 1.1</b>

The Vaca Muerta Formation is commonly subdivided based on lithology and depositional environment (Garcia et al., 2013). The lower Vaca Muerta has the highest organic content and the lowest carbonate content. It is recognized as the hydrocarbon kitchen. The log signature shows a significant increase in gamma ray and a decrease in bulk density. The upper Vaca Muerta has less TOC and its carbonate content increases upward, while the siliciclastic content decreases. The clay content remains fairly constant throughout the whole interval. The transition between the Quintuco and the upper Vaca Muerta is identified in the logs as a noticeable reduction in bulk density (Figure 1.5).

### 1.3 Study area and data available

The RCP study area is located in the eastern part of the basin: the embayment. The Wintershall block covers an area of approximately 90 km<sup>2</sup>. The seismic dataset used in this work covers the entire block of interest, plus a significant portion of adjacent blocks to the south and west. It spans an area of approximately 600 km<sup>2</sup>. There is only one vertical well inside the Wintershall block (Well A), with two more currently being drilled, cored, logged, and completed. Three additional offset vertical wells (Wells B, C and D). are located within the seismic survey area, and therefore are also important to the analysis (Figure 1.6).

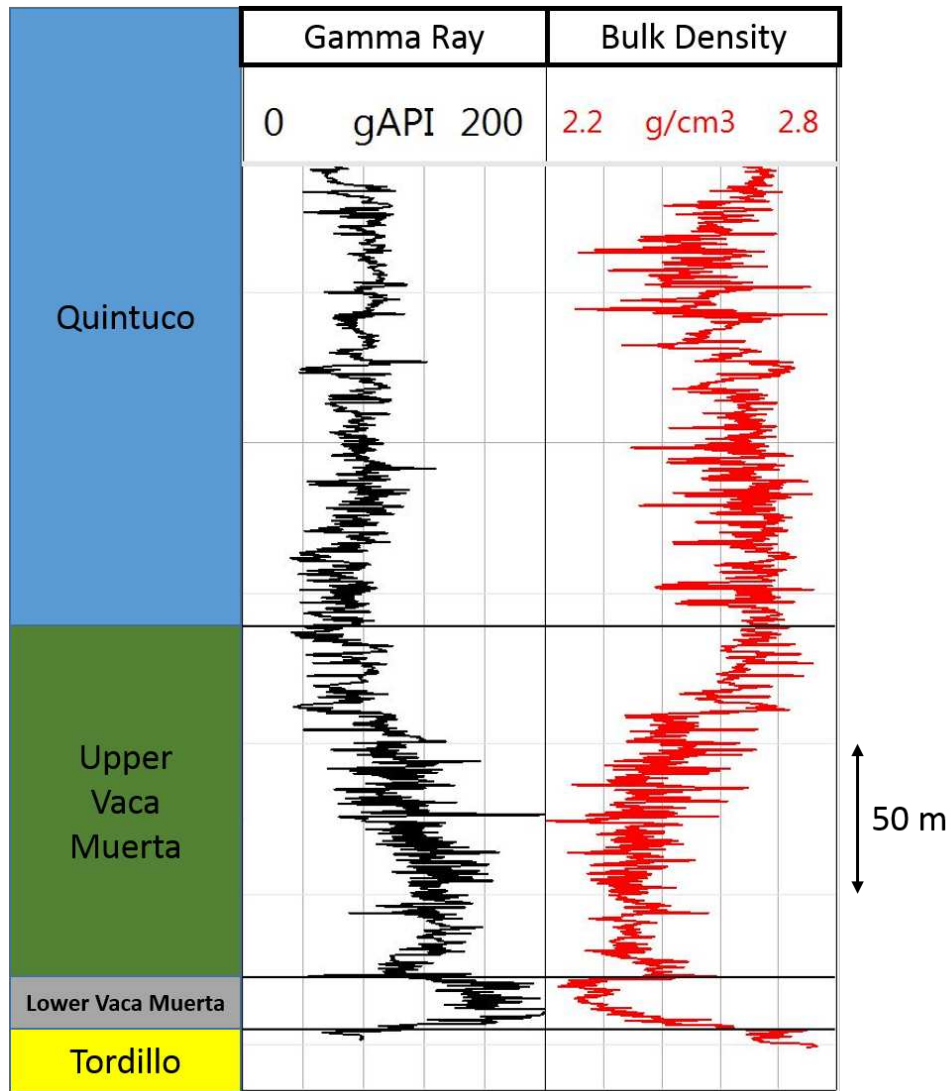


Figure 1.5: Type Log of the Quintuco and Vaca Muerta units in the study area.

### 1.3.1 Seismic data

The seismic dataset is part of a mega 3D survey of narrow-azimuth P-wave data, originally designed to characterize the conventional reservoirs in the area. Table 1.2 shows the acquisition parameters.

The data processing was done preserving the amplitudes, making it suitable for AVO analysis and pre-stack inversion. The following steps summarize the main steps of the processing sequence:

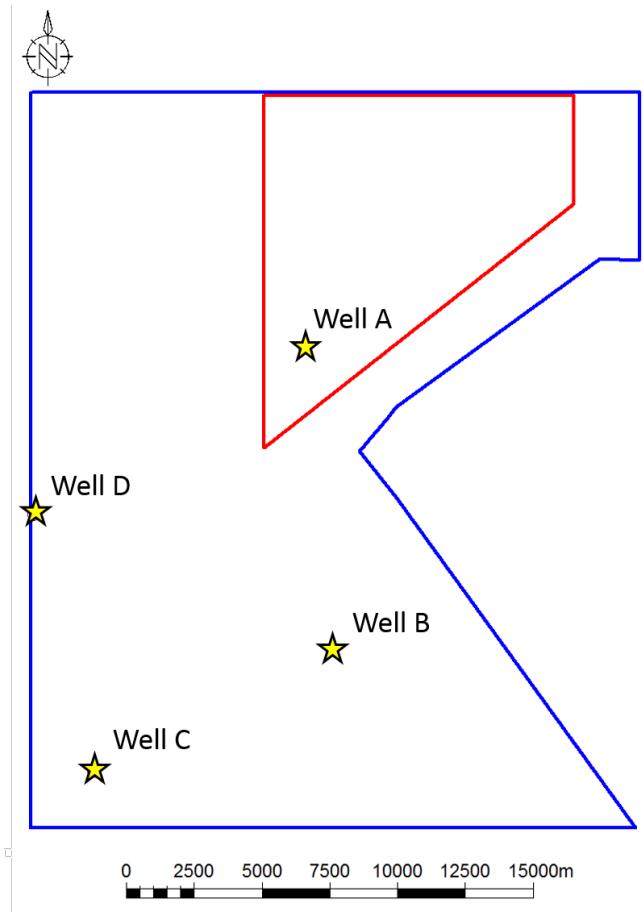


Figure 1.6: Map of RCP study area. The red polygon encloses the Wintershall block, and the blue polygon encompasses the area of the seismic survey.

Table 1.2: Seismic acquisition parameters.

Patch size	9,180 x 3,300 m
Aspect ratio	0.36 (narrow azimuth)
Source type	Vibroseis
Shot line spacing (m)	420
Shot point interval (m)	60
Receiver line spacing (m)	300
Receiver spacing (m)	60
Record length (s)	2.5
Sample rate (ms)	2
Number of inlines	908
Number of crosslines	751
Bin size	30 x 30 m
Maximum offset (inline direction)	4,500 m

- Geometry and geometrical spreading.
- Surface consistent spectral constraint deconvolution.
- Amplitude compensation.
- Refraction statics.
- Surface consistent residual statics.
- Velocity analysis and mute.
- Radon multiple attenuation.
- Surface consistent shot and receiver scalars.
- Pre-stack FXY filter.
- Pre-stack time migration (PSTM), isotropic.
- CDP stack.
- Post-stack noise suppression.

The data volumes available for this thesis are the PSTM gathers, the final stack, and the migration velocity volume.

### **1.3.2 Well data**

Table 1.3 shows the available data for all four wells used in this study. All of them have modern and high-quality wireline logs that cover the entire Vaca Muerta, and, in most cases, the Quintuco and a small interval in the Tordillo. Shear sonic data are available for all wells, allowing for the calculation of elastic properties. Ultrasonic Borehole Imager (UBI) and Oil-Based MicroImager (OBMI) data are the image logs available because of the drilling of these wells with oil-based muds.

Table 1.3: Well database for the study area.

		Well A	Well B	Well C	Well D
Logs	Gamma Ray	X	X	X	X
	Bulk Density	X	X	X	X
	P-Sonic	X	X	X	X
	Shear Sonic	X	X	X	X
	Stoneley Sonic		X	X	X
	Borehole Image	X	X	X	
	Spectral Gamma		X	X	
	Spinner	X	X	X	
Core/Cuttings	XRD	X	X	X	
	Rock-Eval		X	X	
	Porosity-Saturation		X	X	
	Core Photos		X	X	
	CT Scan		X	X	
Engineering	DFIT	X	X		
	Production Data	X	X	X	
	Well Reports	X	X	X	X

Data from sidewall core and cuttings are available, such as X-Ray Diffraction (XRD) and Pyrolysis Rock-Eval, which allow for the calibration of mineralogy and TOC calculations from logs. Some wells even have petrophysical measurements on core, such as porosity, grain density, water, oil, and gas saturations, as well as Computerized Tomography (CT) Scans and core photos.

Engineering data are not rich in this area. Although production history only accounts for a few months, and the Diagnostic Fracture Injection Tests (DFIT) are limited, there is a wealth of information from reports on mud log data, as well as drilling and completion reports. These can give valuable information on drilling events related to formation pressure and wellbore stability, important for geomechanical understanding of the reservoir.

#### 1.4 Previous studies

Since it is still an emerging play, published literature on the Vaca Muerta treating it as an unconventional reservoir is not abundant. Important aspects of shale characterization have

been analyzed, but mostly at the wellbore scale. These include optimization of completion strategies (Ejofodomi et al., 2014), dynamic flow analysis (Badessich and Berrios, 2012), hydraulic fracture modelling (Monti et al., 2013), geomechanical controls on production (Garcia et al., 2014), geological heterogeneity (Sagasti et al., 2014), and production analysis and forecasting (Herrero et al., 2014). Even fewer studies incorporate seismic data as a tool to predict rock properties in 3D (Figure 1.7). Truman Holcombe et al. (2014) show a case study in which seismic data were reprocessed to improve the input data going into seismic inversion and obtain anisotropy information for *in-situ* stress and fracture characterization. They use a multivariate technique to predict a 3D distribution of kerogen content in the Vaca Muerta by combining pre-stack seismic attributes and petrophysical analysis (Figure 1.7(a)). Zunino and Soldo (2014) show the use of a rock mechanics template on the Lambda-Mu-Rho (LMR) domain in order to identify TOC-rich or poor areas, as well as brittle zones. They then apply this template to pre-stack inversion volumes to assess the spatial extent of these zones and optimize the location of future wells (Figure 1.7(b)).

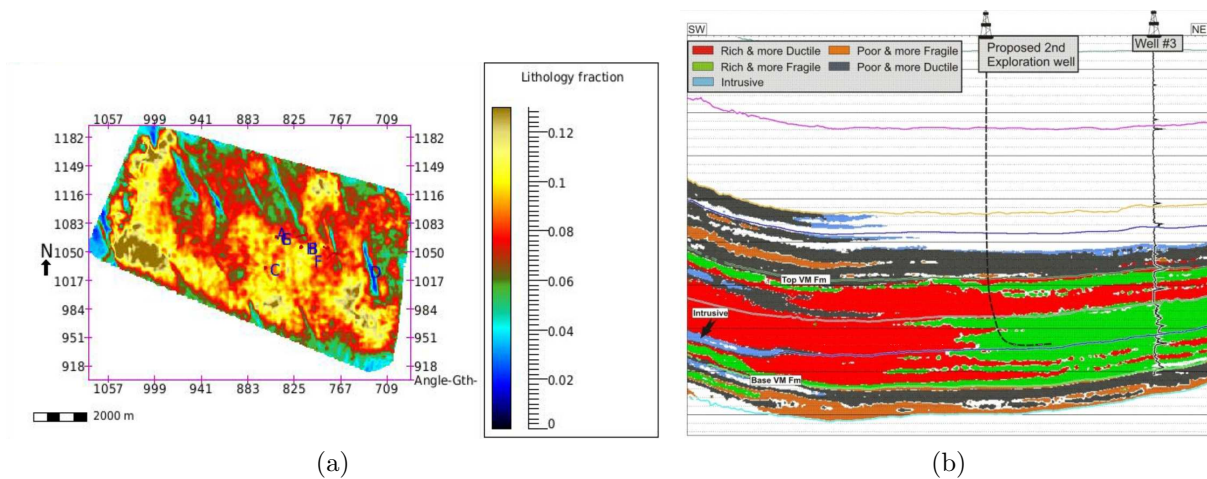


Figure 1.7: (a) Map of kerogen fraction distribution derived from pre-stack inversion and petrophysical logs (Truman Holcombe et al., 2014). (b) Seismic cross-section color coded by the zones derived from the LMR rock mechanics template, showing a proposed well location (Zunino and Soldo, 2014).

The Colorado School of Mines has developed high-quality research on the Vaca Muerta related to geomechanics. Once again, these studies were focused at the wellbore scale. Herzog (2014) applied a workflow for predicting pore pressure using a modified Bowers approach, by taking into account the effects of porosity and lithology on compressional wave velocities from wireline logs. Kosset (2014) performed a complete wellbore stability study, including a 1D geomechanical model, the analysis of temperature, chemical and flow-related effects on *in-situ* stress, and stochastic risk and sensitivity analysis.

Of all these studies, the work conducted by Willis (2013) is the most relevant for this thesis. Willis used core data and cross-dipole sonic tools to calibrate and obtain the anisotropic stiffness tensor for the whole Vaca Muerta. Cluster analysis was performed in several wells in the study area, using gamma ray, compressional slowness and bulk-density logging suites. Backus averaging allowed Willis to upscale the stiffness tensor for each cluster group. The cluster definition showed definite trends in terms of stiffness coefficients and Young's Moduli (vertical and horizontal). These clusters were used as geomechanical facies to populate a 3D Mechanical Earth Model (MEM) (Figure 1.8). The lateral distribution of the geomechanical facies is determined only by geostatistical means, using an exponential variogram, as well as facies weighting (Willis, 2013). No seismic data were used to constrain the prediction of these clusters away from the wells.

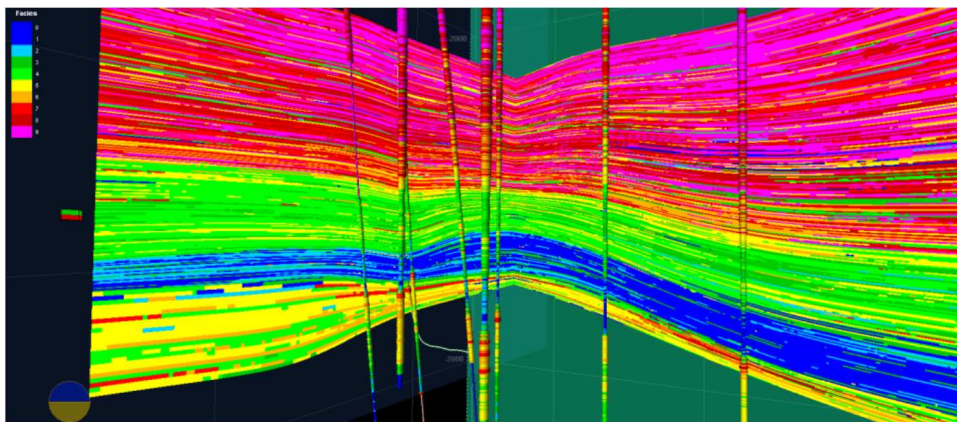


Figure 1.8: 3D view of modelled mechanical clusters for the Quintuco and Vaca Muerta (Willis, 2013).

Pre-stack attributes derived from seismic inversion can provide a powerful tool to assess the lateral variability of rock properties. A good example of the integration of seismic inversion and cluster analysis can be found in the work performed by Dueñas (2014), in the Montney Shale reservoir in Pouce Coupe Field, Alberta, Canada, as part of RCP. Cluster analysis was applied using wireline logs mostly governed by *composition*, rather than texture: neutron porosity, bulk density, Gamma Ray, and photoelectric effect. By cross plotting elastic properties such as LMR, in combination with the results of cluster analysis, her work was able to identify and map the areas of better rock quality on the 3D seismic volume (Figure 1.9).

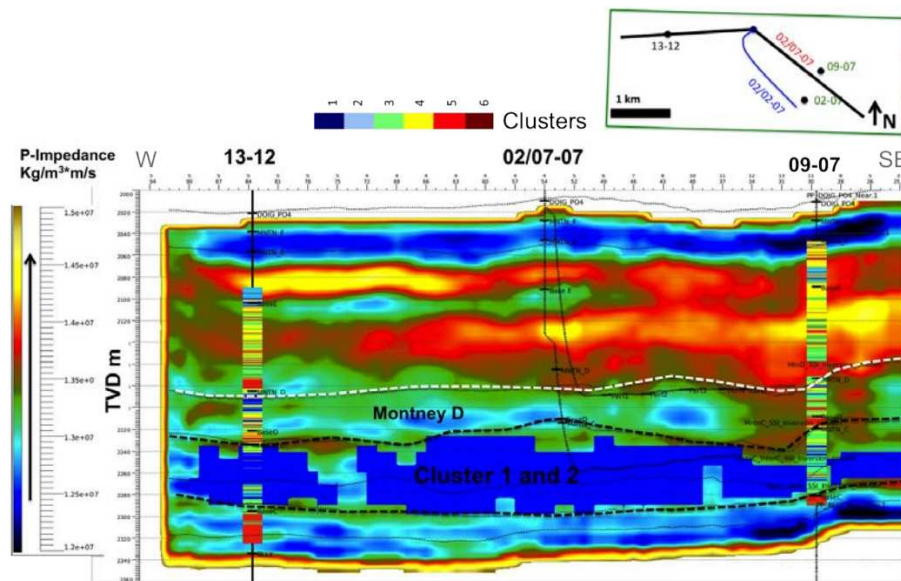


Figure 1.9: Cross section of P-impedance volume, showing geobodies of clusters 1 and 2, interpreted as high quality rock. Montney Shale, Pouce Coupe Field, Canada (Dueñas, 2014).

The work from Willis (2013) and the cluster analysis by Kyla Bishop can be combined with the research on seismic-derived rock properties from Dueñas (2014) to move towards an integrated understanding of the *mechanical* behavior of the Vaca Muerta.

## 1.5 Methodology of this work

Figure 1.10 shows an illustration of the generalized workflow undertaken in this study. Several data sources at different scales were used. Emphasis was made on quality control and validation in most of the steps.

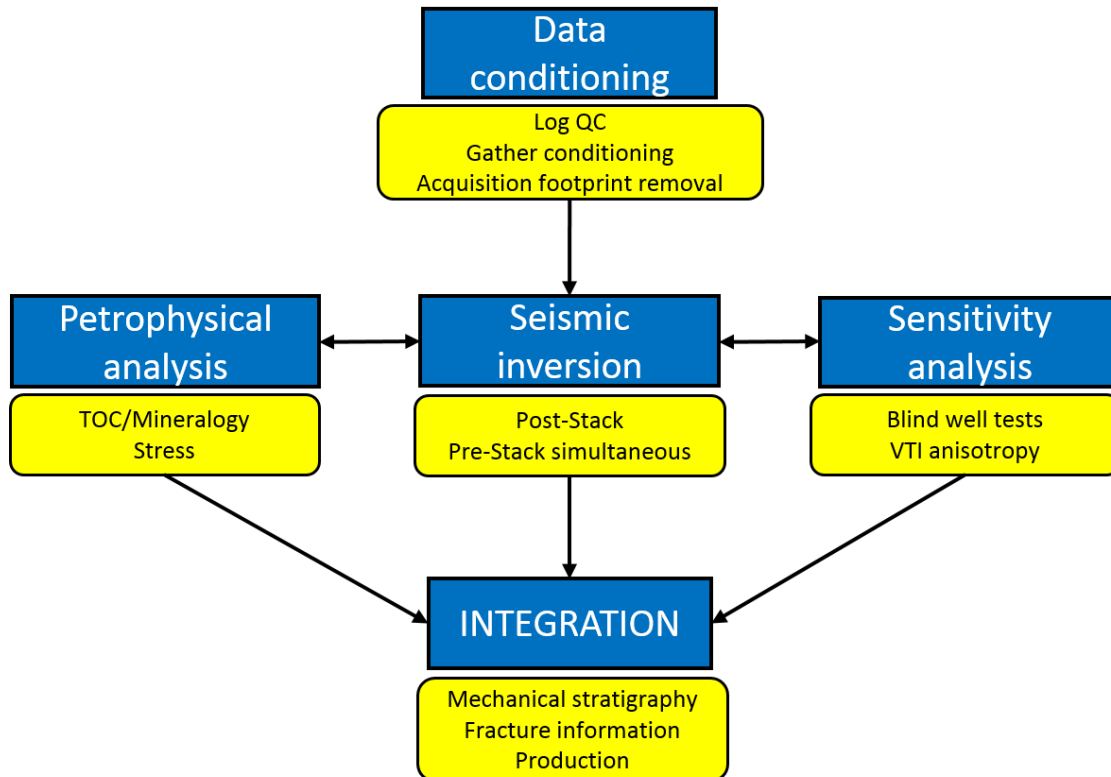


Figure 1.10: Workflow of the research presented in this thesis.

## CHAPTER 2

### DATA PRE-CONDITIONING

Before running a seismic inversion process, some steps are necessary to ensure that the data are complete, in the right domain, and have the highest quality possible, thus generating a better output for interpretation. These steps involve careful review and manipulation of the well log and seismic data, and are explained in this chapter.

#### **2.1 Well log quality control**

This is a key part of the workflow, since the elastic-property logs (bulk density, compressional and shear sonic) are needed for almost every step in the inversion process, including well ties, wavelet estimation, the low-frequency model, and the interpretation process. The well logs need to be carefully examined for: differences in logging tools or vendors, data spikes or unrealistic values, missing sections, borehole rugosity, and misaligned data in depth, among others.

A detailed correction was performed on the elastic-property logs for all available wells in the Quintuco and Vaca Muerta intervals, de-spiking the data and correcting the unphysical values, which were very few, mostly around the end of the log runs. The bulk-density log in particular can be very sensitive to borehole condition, yielding incorrect values in the case of washouts. The caliper log can be a useful tool in determining these zones. Few zones of possible borehole washout were detected based on the caliper, and in these zones the bulk-density log did not show an anomalous behavior. This suggests that the petrophysicist did a good job compensating for these effects.

The consistency of the elastic-property log data between the different wells is fundamental for inversion and interpretation. Figure 2.1 shows histograms that help evaluate this inter-well consistency. The wells in the area have a good match, confirming that the log data available are of good quality.

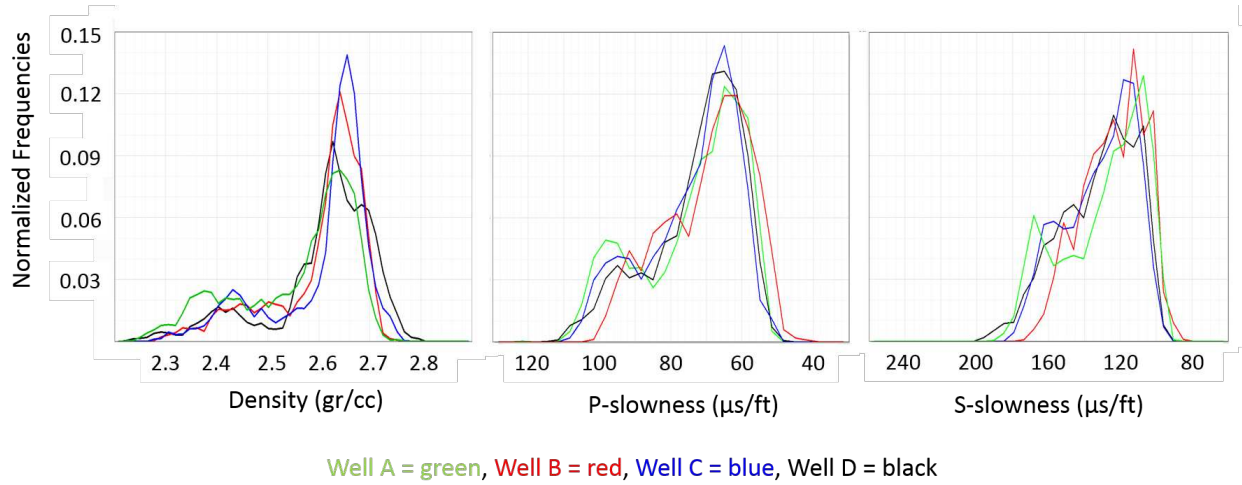


Figure 2.1: Histograms of elastic-property logs for the four wells in the Quintuco-Vaca Muerta interval. Left: bulk density. Center: compressional slowness. Right: shear slowness.

## 2.2 Synthetic log generation

All four wells in the study area have compressional and shear slowness logs that cover the entire Quintuco-Vaca Muerta zone. The bulk-density logs are complete for this zone for wells A and C. Wells B and D have density data only in the Vaca Muerta. Since the inversion and interpretation includes the Quintuco, synthetic bulk-density logs are needed for this formation in wells B and D.

Wells A and C were used to crossplot bulk density versus P-wave velocity from compressional slowness for the Quintuco (Figure 2.2). The crossplot shows that a Gardner-type power function fits the data adequately. The empirical equation obtained is the following:

$$\rho_{syn} = 1075.7 * Vp^{-0.1063} \quad (2.1)$$

where  $\rho_{syn}$  is the synthetic bulk density in  $\text{kg/m}^3$ , and  $Vp$  is the P-wave velocity in  $\text{m/s}$ .

Equation 2.1 was used with the sonic logs for wells B and D to obtain the synthetic curves for the Quintuco, and then these were spliced with the measured bulk density logs in the Vaca Muerta.

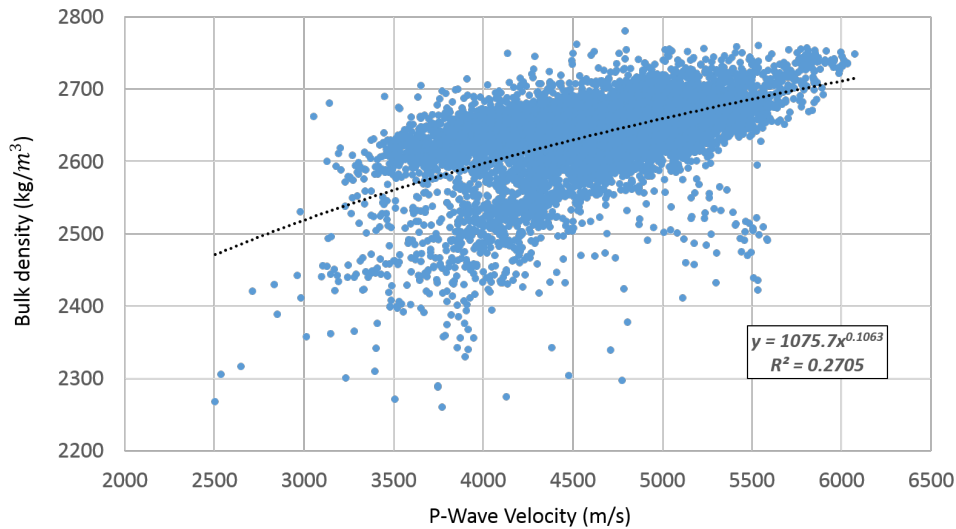


Figure 2.2: Crossplot of bulk density vs P-wave velocity for the Quintuco interval in wells A and C. The dotted black line represents the best-fit power-law trendline, and the corresponding equation and correlation value are shown in the box on the bottom right.

### 2.3 Pre-stack seismic gather conditioning

Figure 2.3(a) shows the original pre-stack gathers in the area of interest around Well A, and Figure 2.3(b) shows the same gathers after standard conditioning steps, such as muting and Radon de-noising. As is clear from this figure, although there is good event coherency and high signal-to-noise ratio, the reflectors are not optimally flat for a reliable AVO inversion. Therefore, it was decided that in order to improve the inversion outputs, it was necessary to perform further pre-conditioning of the gathers, with the goal of obtaining flatter events while preserving AVO class 2 events with polarity reversals at far offsets, such as the top Quintuco reflector.

The Geophysics team at the Wintershall office in Kassel, Germany, applied Residual Move-Out (RMO) to the full survey gathers. Because of the size of the survey, this was a computer-intensive process. Figure 2.3(c) shows the output gathers around Well A. The RMO process was performed over a long time window in order to preserve the AVO class 2 event at the top Quintuco. Therefore, this process was a compromise, as some events are still not ideally flat, especially in the middle of the Quintuco. These results, however, show

a clear improvement with respect to the input data from Figure 2.3(b).

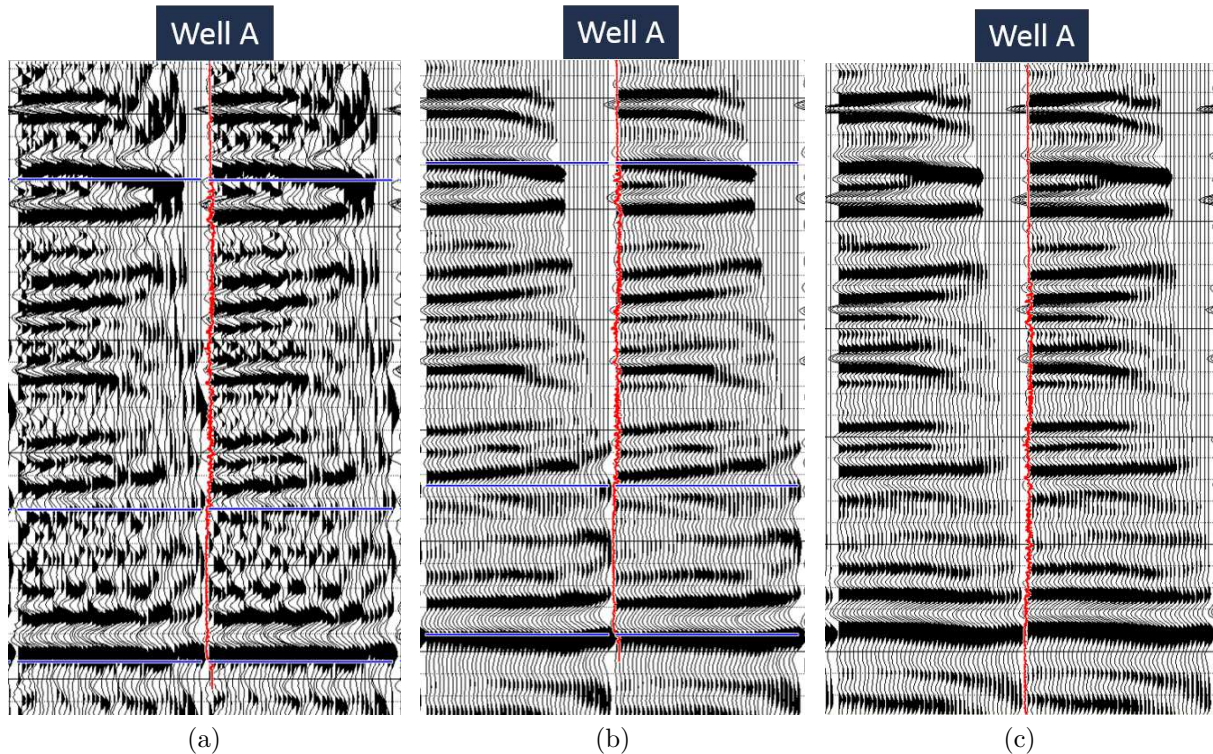


Figure 2.3: Pre-stack migrated offset gathers around Well A. (a) Original data. (b) Data after muting and Radon de-noising. (c) Improved data after RMO, showing flatter events for AVO inversion.

## 2.4 Angle stacks and data alignment

Once the gathers are properly pre-conditioned, they need to be converted from the offset domain to the incident-angle domain, since the AVO equations applied to seismic inversion are a function of angle (MacFarlane, 2014). Hampson-Russell<sup>TM</sup> software was used to transform the data from offset to angle. It employs the Ray Parameter Method, based on the following equation (Russell, 2014):

$$\sin \theta = \frac{XV_{int}}{tV_{rms}^2} \quad (2.2)$$

where  $\theta$  is the incident angle,  $X$  is the offset,  $V_{int}$  is the interval P-wave velocity,  $V_{rms}$ , is the root-mean-square (RMS) P-wave velocity, and  $t$  is the two-way vertical travelttime.

It is clear from Equation 2.2 that P-wave velocity information is needed to apply this offset-incident angle conversion. The migration velocity field available for the full survey was used (Figure 2.4(a)). This is a smooth and not horizon-consistent velocity field, but the interval velocity trends, obtained by the Dix equation, are consistent with the interval velocities from the well logs, which gives confidence to its use for the conversion. Figure 2.4(b) shows the pre-stack gathers converted to the incident-angle domain. After careful review of the angle gathers in different areas of the survey, quality data is good up to 36 degrees.

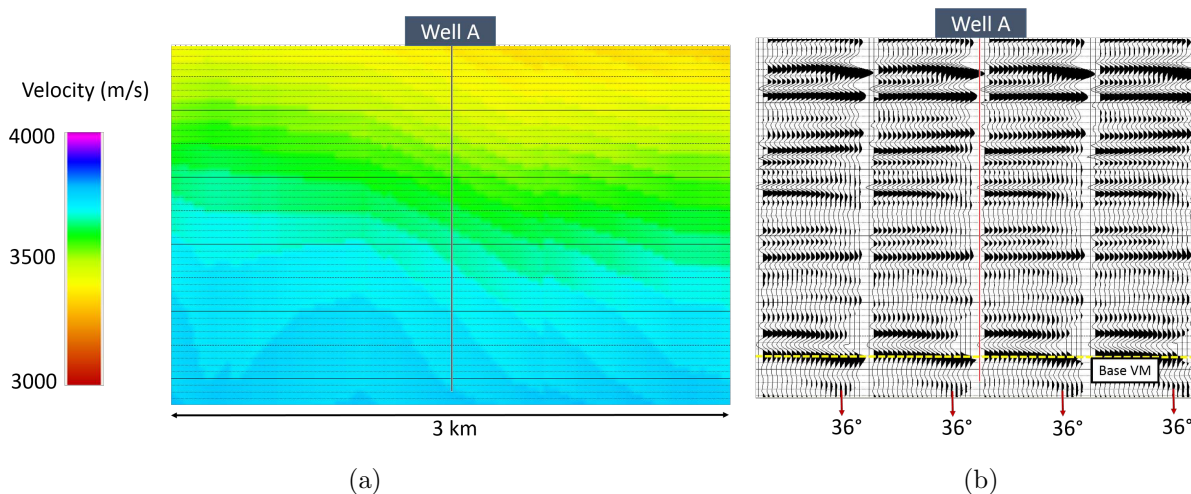


Figure 2.4: (a) Inline plot of the migration velocity field used for the offset-incidence angle conversion of the pre-stack gathers. (b) Angle gathers around Well A. Traces go from 2 to 44 degrees, in 2 degree increments. Note the lack of data from 38 to 44 degrees close to the base of the Vaca Muerta.

The input into the seismic inversion requires at least three partial stacks with limited incidence angles to stabilize the inversion (MacFarlane, 2014). Four sub-stacks were generated, with the following ranges: 0-9°(Nears), 9-18°(Near-Mids), 18-27°(Mid-Fars) and 27-36°(Fars). This selection was done based on the successful case study by Dueñas (2014), which used these same four angle ranges for partial stacks on a P-P dataset, having incidence angles from 0 to 36 degrees just as those for the Vaca Muerta seismic. The excellent quality and stability of the data allowed for the stacking of small subsets of angles without the need for angle overlap, and still yielding consistent partial stacks (Figure 2.5).

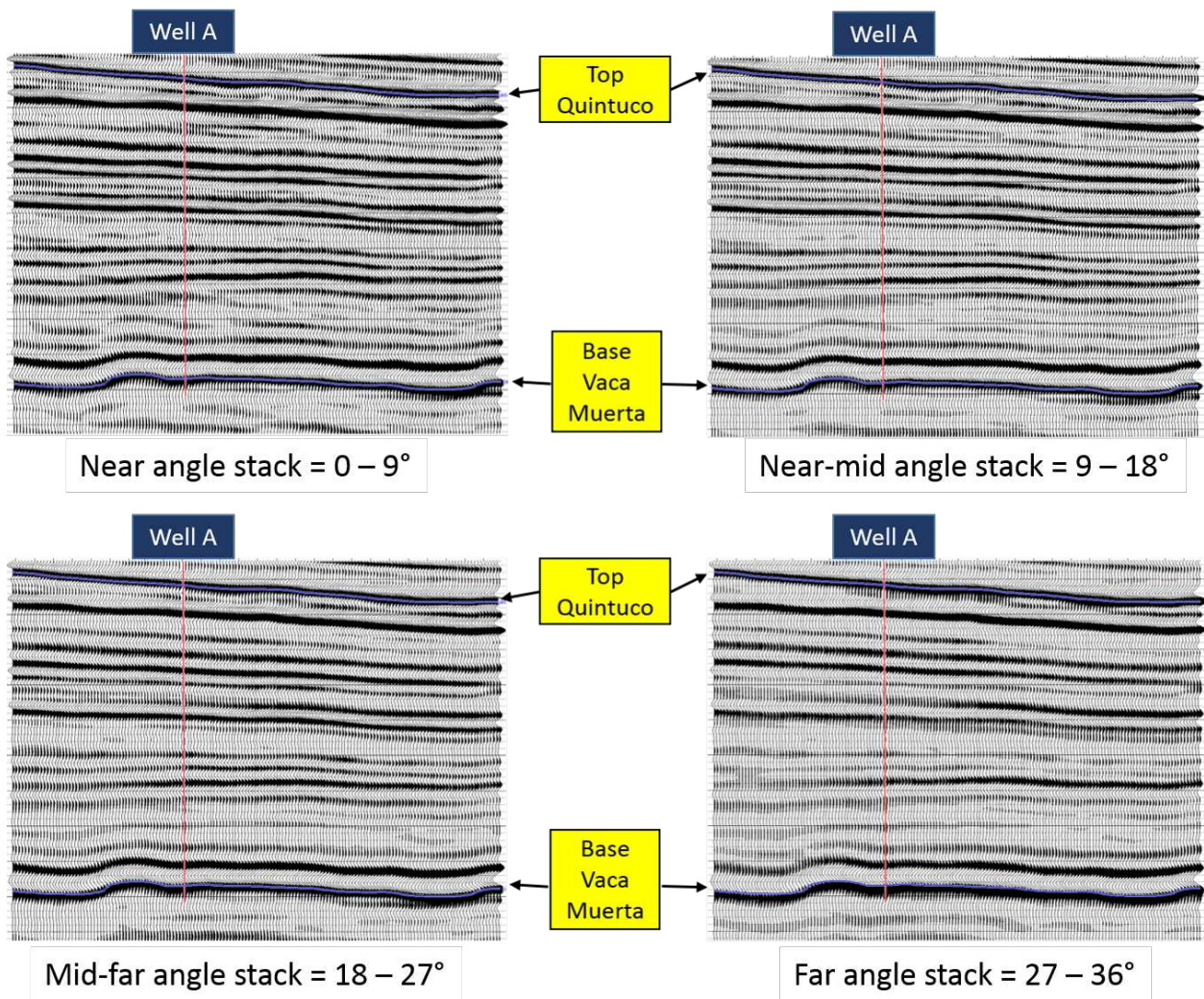


Figure 2.5: Inlines of the four sub-stacks generated for pre-stack simultaneous inversion.

A successful inversion is dependent on the time alignment of the partial angle stacks. The main causes for misalignment are inaccurate migration velocities or incorrect statics in processing. To ensure that the data are aligned as best as possible, small static adjustments are calculated and applied to each sub-stack volume to optimise the trace-to-trace cross-correlation (MacFarlane, 2014).

The alignment of the Near-Mid, Mid-Far and Far angle stacks was performed in Jason<sup>TM</sup> software, using the Near angle stack as a reference volume. The Near angle stack is the most similar to the zero offset as it is less compromised by normal move-out. Volume alignment

was used instead of horizon alignment because the phase differences, as well as the amplitude differences, are taken into account. The vertical time window used for obtaining the optimal time shift was selected from 100 ms above the Top Quintuco, to 100 ms below the Base Vaca Muerta. The time-shift volumes show small time shifts, not exceeding 3 ms in absolute value (Figure 2.6). After applying these minimal time shifts to each angle stack, the data shows good alignment for inversion.

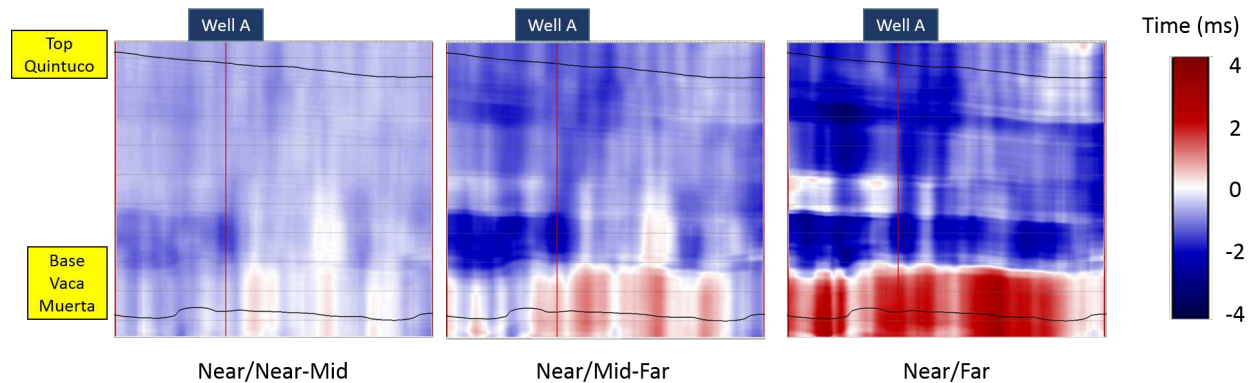


Figure 2.6: Inlines of time-shift volumes applied to the Near-Mid, Mid-Far and Far stack, with the Near stack as the benchmark volume. Negative values indicate an shift upward; positive values represent a downward shift.

## 2.5 Acquisition footprint removal

An acquisition footprint can be defined as any anomaly observed in seismic data related to surface data-acquisition geometry rather than to subsurface geology. Irregularities in stacking fold, and biases in source-receiver offsets and azimuths cause artificial spatial periodicity in enhanced seismic signal. Seismic attributes react to these changes in data quality and create artifacts that resemble the acquisition geometry (Chopra et al., 2011).

The seismic dataset used for this research exhibits a clear acquisition footprint, which can be seen in time slices as stripes in the east-west (inline) direction and, to a lesser degree, in the north-south (crossline) direction (Figure 2.7(a)). The narrow-azimuth geometry discussed in Chapter 1 is most likely responsible for this undesirable effect, which contaminates not only

geometric seismic attributes such as curvature and coherency, but also impedance volumes derived from inversion.

Ideally, acquisition footprint should be treated at the time of the survey design and in the processing shop (Chopra and Marfurt, 2007). Thankfully, some tools are available to deal with this issue on the interpretation side. TerraSpark Geoscience’s Insight Earth® software, among its many data conditioning tools, has a proprietary Footprint Removal process, which is a robust and user-friendly coherent noise filter that works in the wavenumber domain. The only inputs needed are the seismic volume itself, the time and trace gates, the direction in which the filter is applied (inline or crossline), and the distance between stripes in the time slice or the spatial periodicity of the noise. Several time slices in the interval of interest were evaluated to determine the optimal distances, both in the inline and crossline directions.

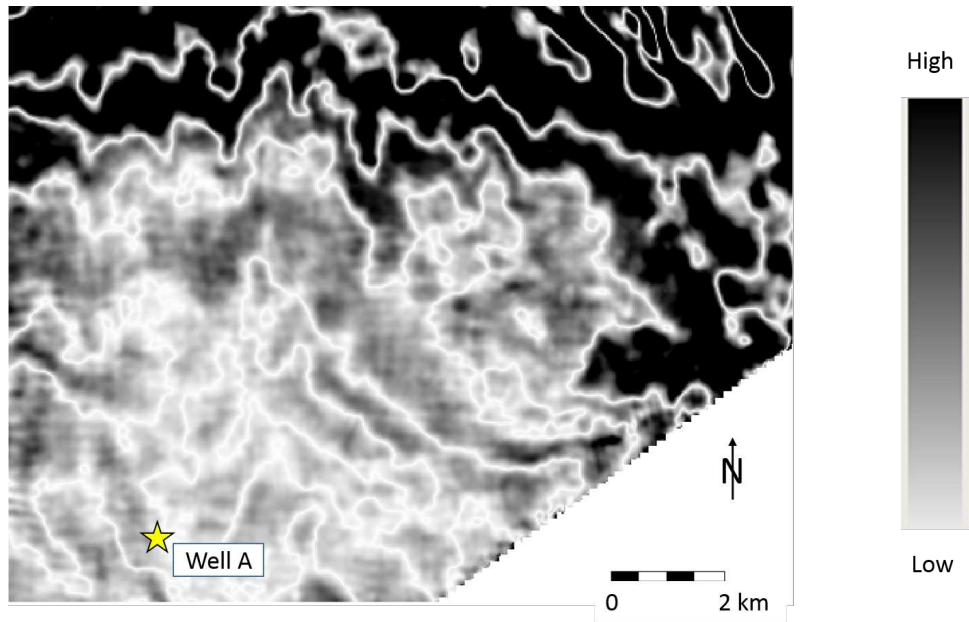
Figure 2.7(b) shows a time slice of the full stack volume after the Footprint Removal process was applied. The improvement with respect to the original volume is notable. Most of the striping noise has been suppressed in both directions. The same process was applied individually to each of the four partial angle stacks.

## 2.6 Summary

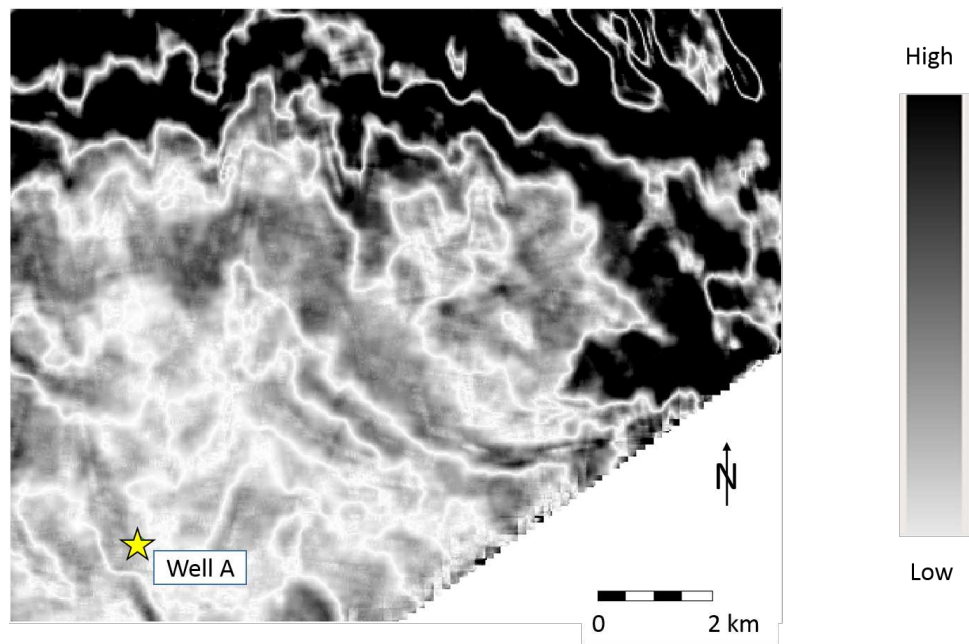
Data pre-conditioning is a key step in any reservoir characterization effort. Even though the data available are of high quality, several steps can be taken to improve them even further. That way the subsequent interpretation and integration is more accurate and robust. Data conditioning was applied to both the well logs and the seismic data.

With the density and sonic logs, general QC, editing and de-spiking, and histogram matching were performed, as well as synthetic bulk density log generation for the Quintuco interval in some wells, using non-linear regression on data from other wells.

With the seismic, Wintershall performed detailed pre-stack gather conditioning: muting, de-noising, and RMO. The gathers were transformed from offset to incidence angle using the migration velocity volume, generating four partial angle stacks and applying residual time alignments using time shift volumes. Finally, the acquisition footprint was reduced in all



(a)



(b)

Figure 2.7: Time slices of raw seismic amplitudes in the northeastern part of the survey, extracted inside the Vaca Muerta interval. (a) Original data. Note the striping pattern in the east-west and north-south directions. (b) Data after application of the Footprint Removal process.

volumes using Insight Earth® Footprint Removal module.

The outputs from the work described above are much improved for input into the seismic inversion and petrophysical analysis processes described in later chapters.

## CHAPTER 3

### SEISMIC INVERSION

Inversion can be defined as deriving from field data a model that describes the subsurface and is consistent with the data, determining the cause from the observation of effects (Sheriff, 2002). In the specific case of seismic data, inversion methods are techniques that extract information about properties of the subsurface, including the prediction of acoustic impedance from stacked seismic data, the estimation of changes in elastic properties from pre-stack seismic data, and methods that use the variation of reflection amplitude with offset to detect the presence of hydrocarbons in the subsurface (Keys and Foster, 1998). The acoustic impedance and AVO attributes derived from seismic inversion can be transcribed into petrophysical parameters, and combined with the structural framework to create a model of the reservoir. Therefore, seismic inversion can act as the bridge of integration between petroleum geology, petroleum engineering, and geophysics (Yilmaz, 2001) .

The use of pre-stack data in reservoir characterization has been in use for years in conventional reservoirs, but has been mostly focused on facies and fluid discrimination (Ouenes, 2012). With the advent of shale plays, the application of seismic inversion has changed. As tight shales have low porosity (often less than 10%) and generally contain some hydrocarbons, the use of AVO methods is oriented to primarily extract lithology and mechanical properties (Goodway et al., 2010). Reservoir quality indicators such as TOC, and properties related to the potential effectiveness of hydraulically fracturing the rock, such as brittleness, natural fracture presence, and closure stress, are key parameters that need to be known and understood to optimize the production in these plays. These parameters can be estimated with seismic data.

This chapter focuses on the basic theory of post-stack and pre-stack seismic inversion, the underlying assumptions in these methods, and differences between the two algorithms

used in this research: Constrained Sparse Spike inversion (CSSI) and Model-Based inversion. The detailed workflow, QCs and results of the seismic inversions performed on the P-wave dataset for the Quintuco and Vaca Muerta intervals are also presented.

### 3.1 Theory

The basic model from which many seismic inversion methods are based is the convolutional model (Figure 3.1). It states that the seismic trace is simply the convolution of the wavelet or source function with the earth’s reflectivity series, with the addition of a noise component (Russell, 1988). The fundamental objective of inversion is to find a geologically realistic impedance profile that correlates to the reflectivity series, and therefore, satisfies the convolutional model. Noise is usually neglected or assumed to have been sufficiently attenuated during data processing. Therefore, the inversion requires *a priori* information about the wavelet and understanding of the relationship between elastic properties and reflectivity (MacFarlane, 2014).

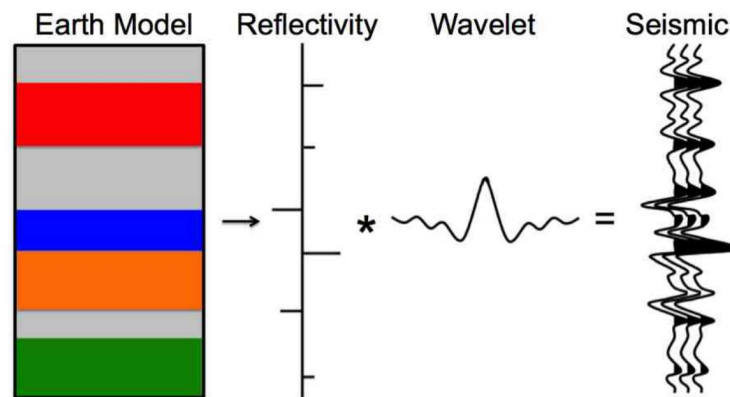


Figure 3.1: Schematic representation of the convolutional model (MacFarlane, 2014).

There are additional assumptions to be considered regarding the wavelet and the reflectivity series. In the convolutional model and inversion, the wavelet is assumed to be constant and well-defined. More realistically, the wavelet is time-variant and complex in shape (Russell, 1988). Its frequency content and phase changes with depth as a result of the high-cut filter characteristics of the earth. To overcome this limitation, it is convenient to constrain

the vertical extent of data input (MacFarlane, 2014). On the other hand, the reflectivity series is assumed to be a perfectly random sequence. This means that its autocorrelation is a spike at zero-lag. The true earth reflectivity cannot be considered truly random, but if the input data time window is sufficiently large, it is a good approximation (Russell, 1988).

### 3.1.1 Post-stack and pre-stack inversion

In post-stack inversion, a band-limited estimate of acoustic impedance, or P-impedance, is obtained from seismic amplitudes. Latimer et al. (2000) explain some of the benefits of acoustic impedance data. P-impedance is a rock property rather than an interface property, and is closely related to lithology, porosity and fluids. It can leverage the reservoir description beyond simple seismic interpretation.

Post-stack inversion assumes the special case of normal incidence; that is, each reflection coefficient is the result of a seismic ray striking the interface between two layers at zero degrees from normal. In this case, there is no mode conversion, and the reflection coefficients are a simple function of the P-wave velocity and density of the layers (Russell, 1988):

$$R_P = \frac{\rho_2 V_2 - \rho_1 V_1}{\rho_2 V_2 + \rho_1 V_1} \quad (3.1)$$

where  $\rho$  is density and  $V$  is P-wave velocity. Subscripts 1 and 2 represent the media values for the incident upper and lower transmitted layers, respectively.

The stacked data are often considered to be a reasonable approximation to a sequence of filtered normal-incidence reflection coefficients. The stack, however, is an average over all angles, and therefore does not represent the true normal incidence reflectivity. Thus, a more accurate input to acoustic impedance inversion would be the acoustic impedance reflectivity from pre-stack gathers (Russell, 2014). Moreover, constructive/destructive interference from thin beds at finite offset ranges generate amplitude distortions in the NMO corrected stacked trace. These distortions are not accounted for in post-stack inversion, but they are dealt with in the pre-stack domain, giving more detail and resolution (Mallick and Ng, 1995).

When the seismic ray strikes the boundary at nonzero incidence angles, there is P-to S-wave conversion and the reflection coefficient becomes a function of the P-wave velocity, S-wave velocity and density of the layers. The equations from which the amplitude variations with offset can be derived are the Zoeppritz equations (Russell, 1988). The use of the full Zoeppritz equations can lead to a complex solution for a given incidence angle. That is why several approximations have been derived for the reflection coefficients that are good for a certain range of angles of incidence. For this work, the Aki-Richards equation (Aki and Richards, 2002) is used, which is a linearized approximation of the P-wave reflection coefficient:

$$R_P(\theta) = \frac{1}{2} \left[ 1 - 4 \left[ \frac{V_S}{V_P} \right]^2 \sin^2 \theta \right] \frac{\Delta \rho}{\rho} + \frac{1}{2} \left[ 1 + \tan^2 \theta \right] \frac{\Delta V_P}{V_P} - 4 \left[ \frac{V_S}{V_P} \right]^2 \sin^2 \theta \left[ \frac{\Delta V_S}{V_S} \right] \quad (3.2)$$

where  $V_P$ ,  $V_S$  and  $\rho$  are, respectively, the average P-wave velocities, S-wave velocities, and densities across the interface,  $\Delta V_P$ ,  $\Delta V_S$  and  $\Delta \rho$  are the differences in parameters across the interface, and  $\theta$  is the average of the P-wave incidence and transmission angle.

In pre-stack inversion, both the low-and high-frequency components of the acoustic impedance are extracted from seismic data. Plus, there is the obvious advantage to using a full elastic model, in which  $V_p/V_s$  (and Poisson's ratio) can be estimated (Mallick and Ng, 1995). Figure 3.2 shows the workflows for both post-stack and pre-stack seismic inversion. Although the steps for both methods are essentially the same (wavelet estimation, low-frequency model building), the quantity of input data, the complexity of the process, and the variety of the products are clearly different.

### 3.1.2 Sparse-spike and model-based inversion

The two main categories of seismic inversion algorithms, trace-based and model-based, are compared in Figure 3.3. The differences between them are mainly in how the methods use modelled data from extrapolated well logs (MacFarlane, 2014). For this research, the CSSI method is mainly used, which is a trace-based inversion. The model-based approach

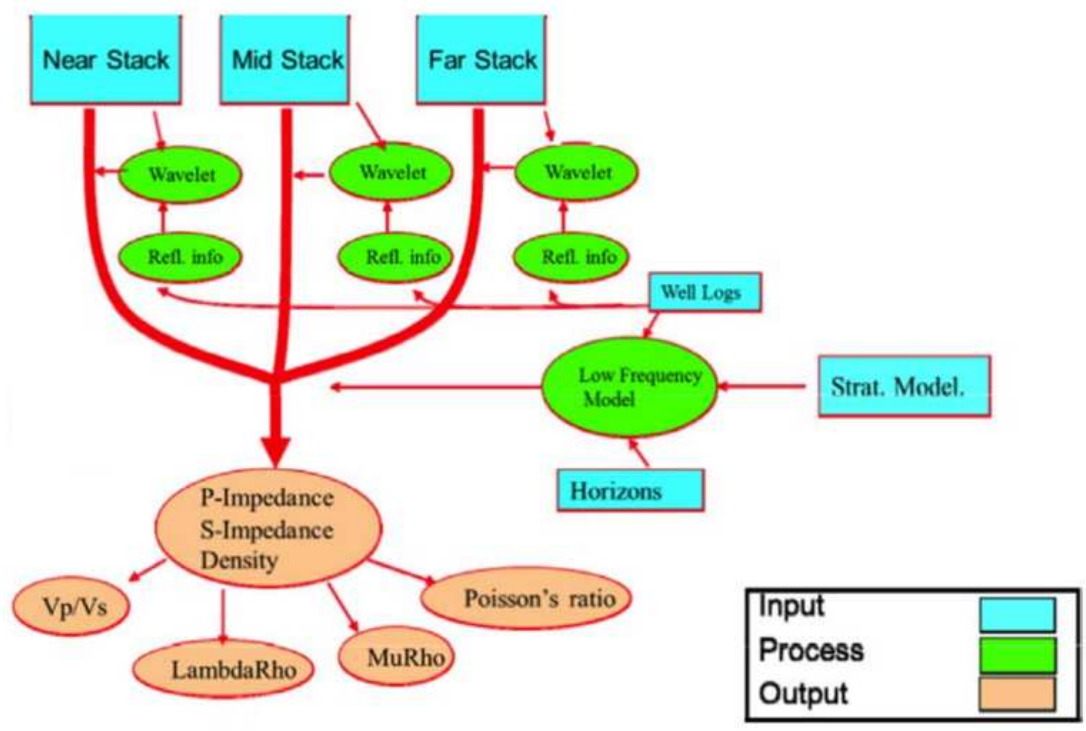
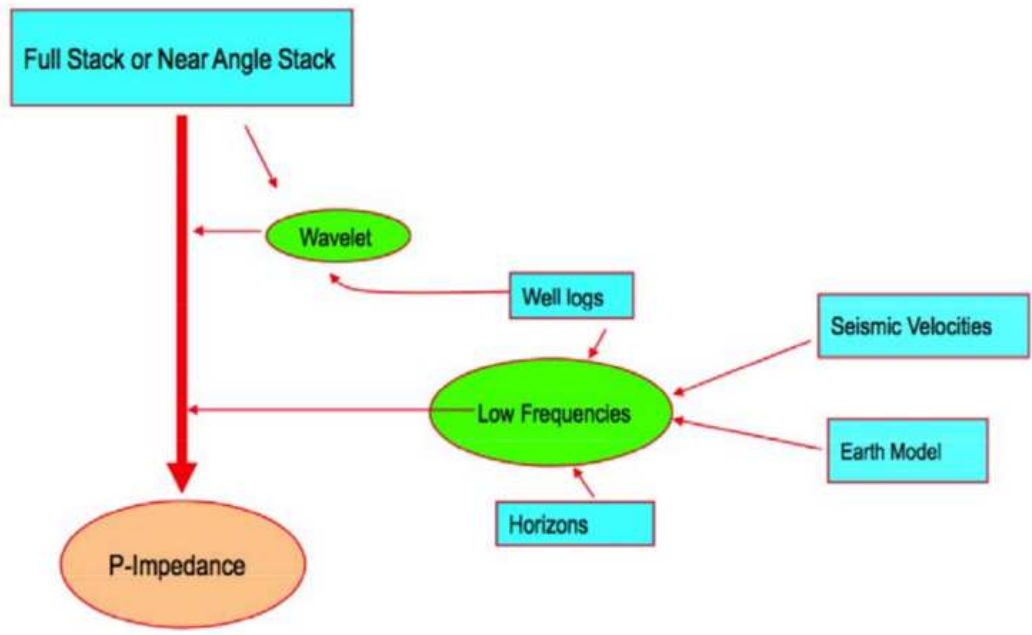


Figure 3.2: Generalized workflows for seismic inversion. Top: post-stack. Bottom: pre-stack. Modified from Dueñas (2014).

is employed mostly for sensitivity and comparison purposes, which are explained in more detail on the next chapter.

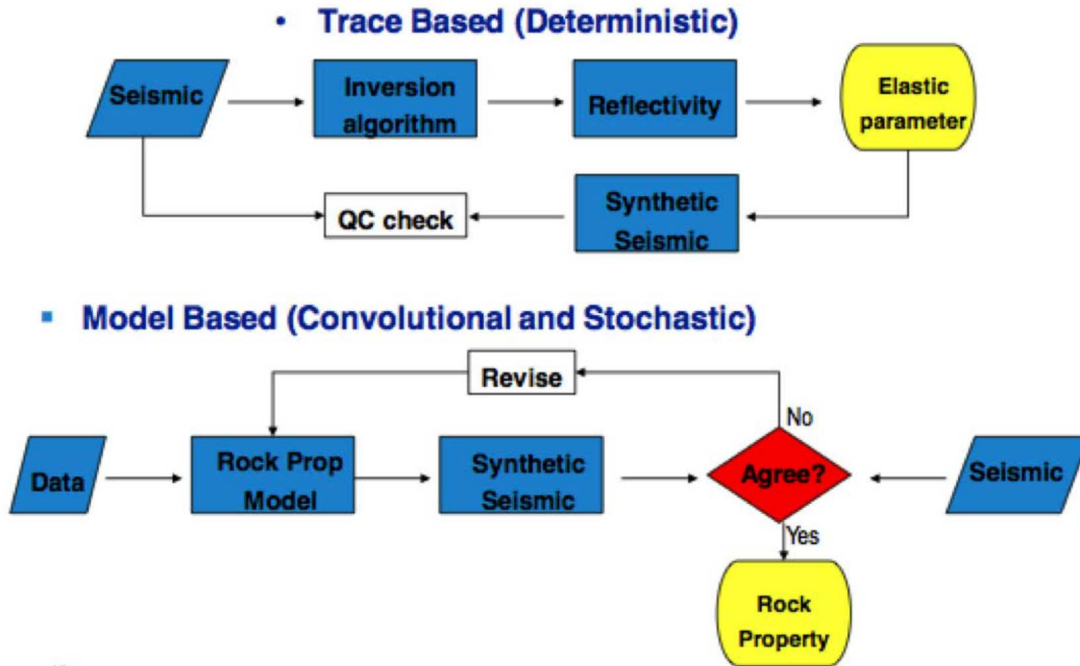


Figure 3.3: Comparison of trace-based vs model-based seismic inversion workflows (Dueñas, 2014).

The CSSI method is the basis for the seismic inversion performed in Jason<sup>TM</sup> software. The reflection coefficient is assumed sparse. In sparse-spike inversion, the method itself is not directly dependent on the impedance log information; the logs are used just to set the correct absolute impedance range. It is called *constrained inversion* because it has certain constraints that are usually provided in order to improve the accuracy of the solution to the inversion (Dueñas, 2014). The core of these constraints lies in the objective function (Equation 3.3), that the CSSI algorithm attempts to minimize. The inversion should be kept simple because of the non-uniqueness of the problem and the assumption that the fewer reflection coefficients needed to match the data the better the representation of the earth model (MacFarlane, 2014).

$$F(V_P, V_S, \rho) = \sum (F_{seismic} + F_{contrast} + F_{trend} + F_{spatial} + F_{SVD} + F_{Gardner} + F_{mudrock}) \quad (3.3)$$

where the individual terms are misfit functions calculated per trace.  $F_{seismic}$  controls the seismic residuals,  $F_{contrast}$  keeps the solution sparse (controls the elastic parameter variance),  $F_{trend}$  stabilizes low frequencies relative to the trend,  $F_{spatial}$  controls the smoothness of the output,  $F_{SVD}$  stabilizes the inversion,  $F_{Gardner}$  constrains the density, and  $F_{Mudrock}$  constrains the S-impedance or  $V_p/V_s$  ratio.

The model-based approach is the basis for the seismic inversion performed in Hampson-Russell™ software. The algorithm is based on the following main assumptions: the linearized approximation to reflectivity holds, and a linear relationship exists between the logarithm of P-impedance and both S-impedance and density, and this relationship holds for the background lithologies. Using these assumptions, one can derive a final estimate of P-impedance, S-impedance and density by perturbing an initial P-impedance model. Using the objective function and this initial guess, the next step is to iterate towards a final solution using the conjugate gradient method (Martins, 2013).

Russell (1988) summarizes the pros and cons of sparse-spike and model-based inversion methods.

Advantages of sparse-spike inversion:

- The data themselves are used in the calculation.
- A geological-looking inversion is produced.
- The low-frequency information is included mathematically in the solution.

Disadvantages:

- Statistical nature of the method is subject to problems in noisy data.
- Final output lacks much of the fine detail; only the *blocky* component is inverted.

Advantages of model-based inversion:

- A complete solution is possible, including the low-frequency information.

- Errors are distributed throughout the solution.
- Multiples and attenuation effects can be modelled.

Disadvantages:

- The solution is arrived at iteratively and may never be reached (may not converge).
- More than one forward model correctly fits the data (non-uniqueness).

### 3.2 Stacked data interpretation

Wintershall performed a comprehensive interpretation of the main horizons from the full stacked seismic data. This interpretation is very important as it will provide the framework for building the low-frequency trend model, which will be discussed in the next chapter. Detailed QC of these horizons was done focusing on consistency of seismic character and continuity across the whole survey. Localized editing of the horizons was needed in a few problem areas such as where gaps exist in the data, especially close to the location of the faults. Also, horizon smoothing was performed with care to preserve the structural detail needed for the low-frequency model.

The main interpreted horizons are seen in section view in Figure 3.4. This E-W inline is important as it crosses Well A and it will be used as a reference line for subsequent seismic section displays. The horizons, in order from shallowest to deepest, are:

- The Top Quintuco, represented by a strong peak reflector, continuous across the area, resulting from the high impedance of the Quintuco with respect to the overlying Mulichincho Formation.
- The "Lower Quintuco", given by a zero-crossing that represents the base of onlapping reflectors. This is the most difficult horizon to interpret but provides additional needed detail for a very thick interval such as the Quintuco.

- The Top Vaca Muerta, characterized by a trough reflector that is continuous across the survey. This comes from the decrease in impedance of the upper Vaca Muerta relative to the lower Quintuco.
- The "Middle Vaca Muerta" horizon, which is a weak trough reflector, with some loss of continuity towards the south. This proves nevertheless to be a good control horizon within the Vaca Muerta.
- The Base Vaca Muerta, a strong and continuous peak reflector, representing the contrast between the lower Vaca Muerta and the stiffer underlying Tordillo sandstone.

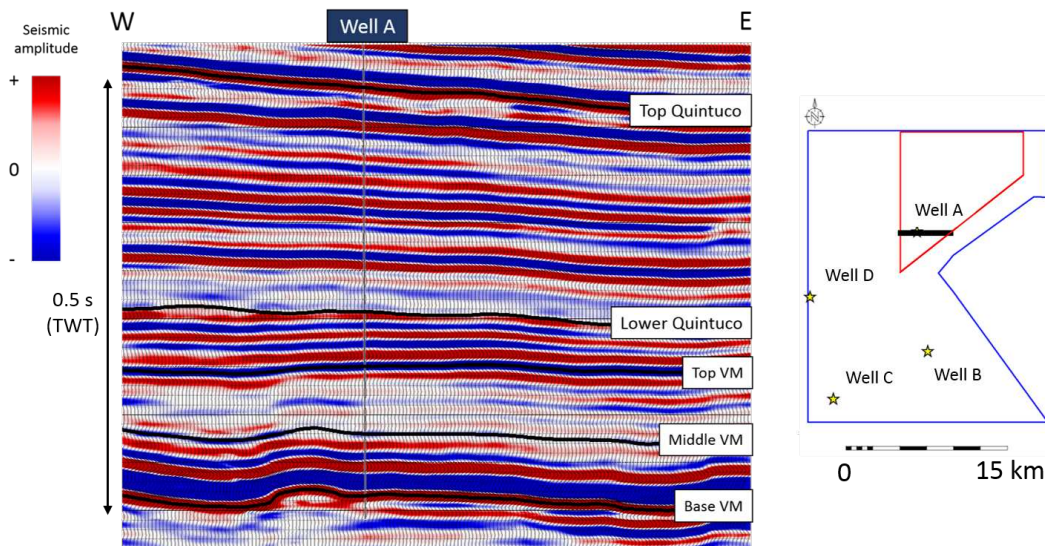


Figure 3.4: Reference inline of full stack seismic data with main horizons interpreted. The relative location of this section is depicted by the thick black line on the base map to the right.

Figure 3.5, Figure 3.6, Figure 3.7, Figure 3.8 and Figure 3.9 show maps of the five horizons interpreted in time domain. With the exception of the Top Quintuco which shows a more defined dip from west to east, the structural trends for all horizons are similar. They are deeper in the center of the survey and shallower toward the south and north. The Base Vaca Muerta horizon is clearly affected by the faults from the intervals below; some of them continue up into the Vaca Muerta (west and northeast).

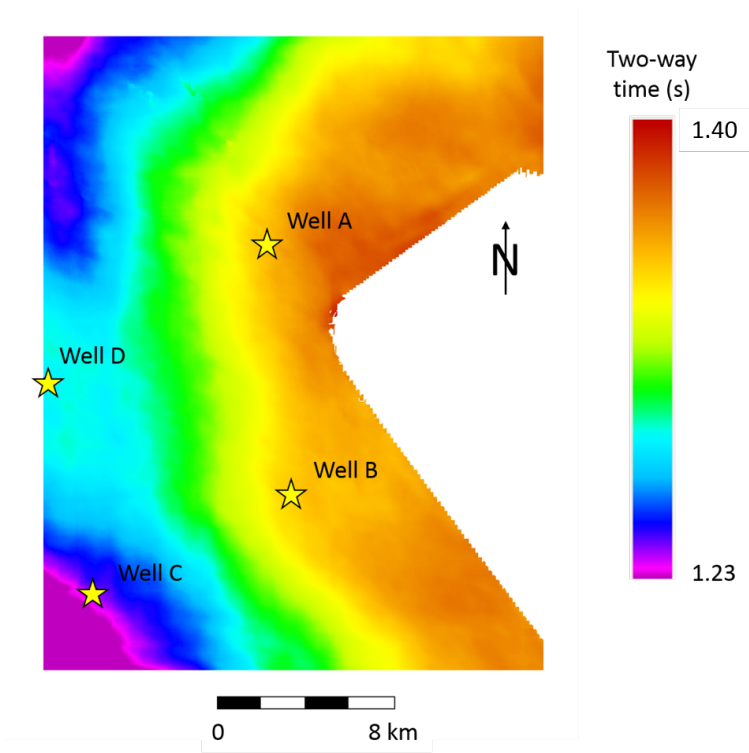


Figure 3.5: Time structure map of the Top Quintuco.

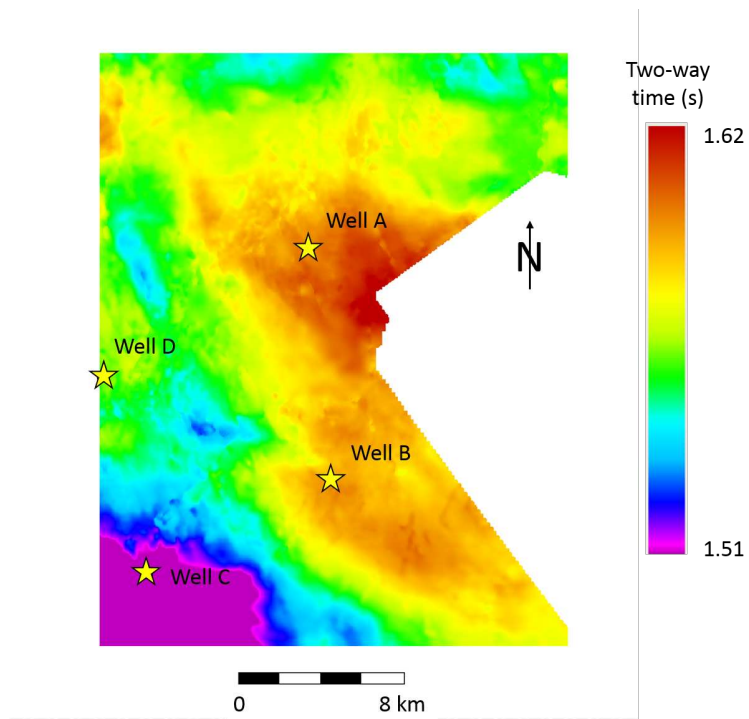


Figure 3.6: Time structure map of the Lower Quintuco.

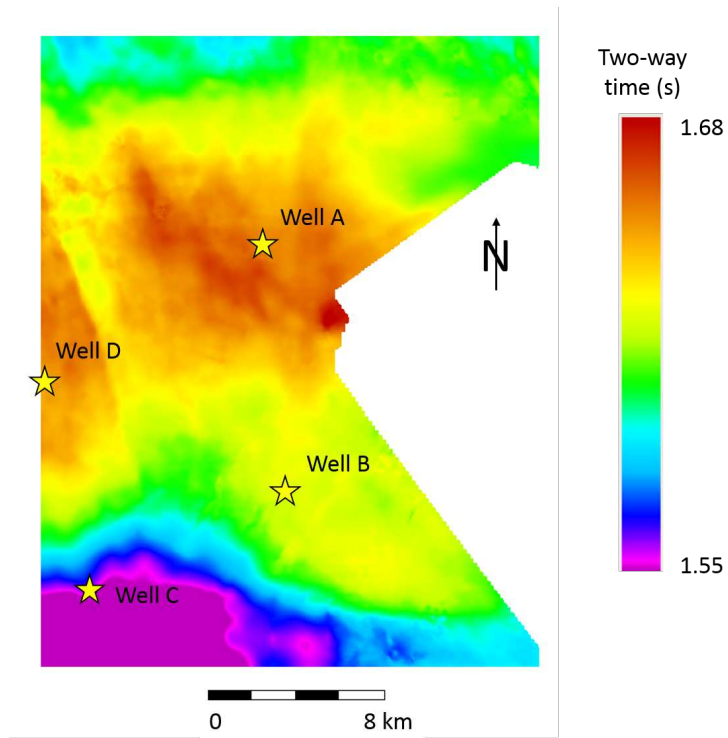


Figure 3.7: Time structure map of the Top Vaca Muerta.

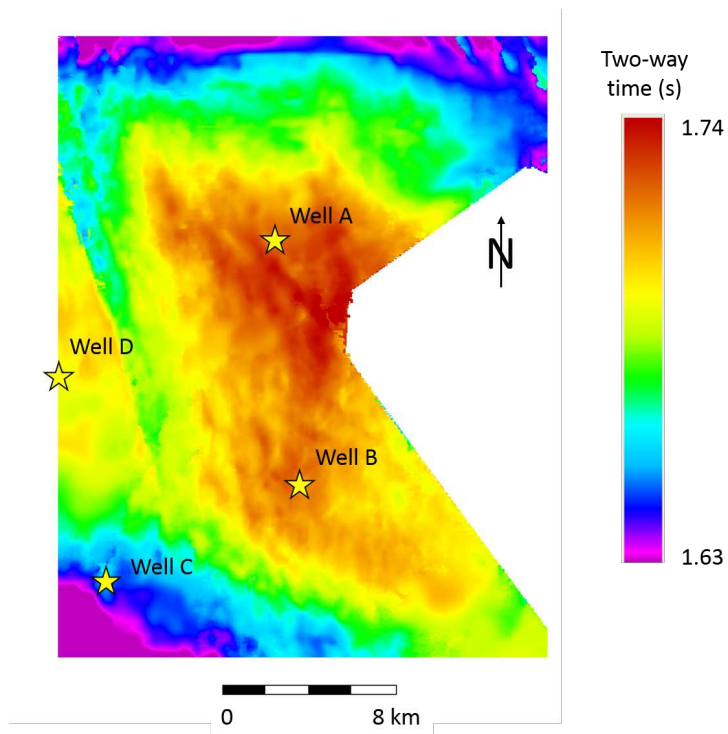


Figure 3.8: Time structure map of the Middle Vaca Muerta.

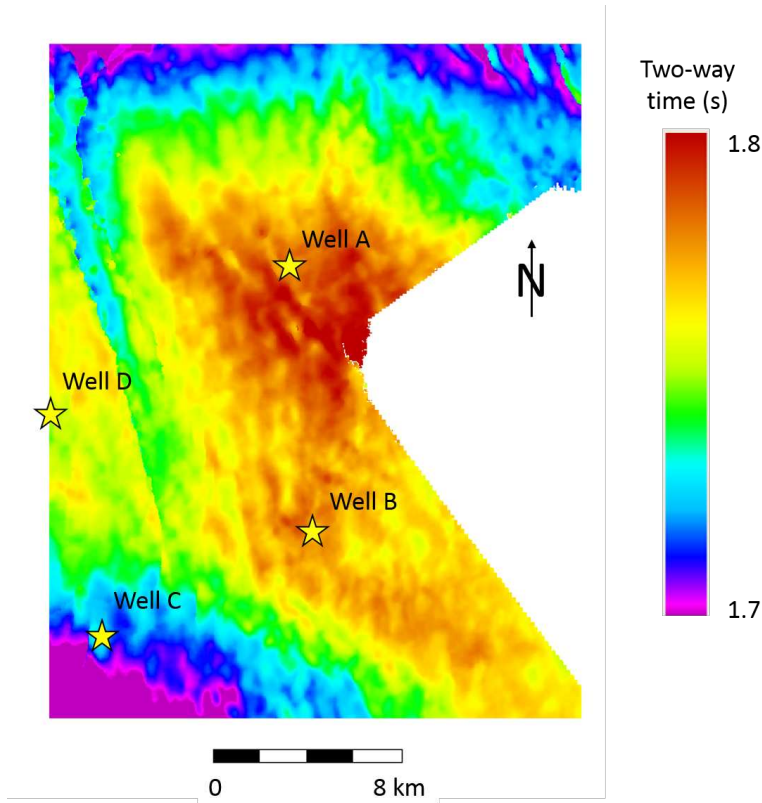


Figure 3.9: Time structure map of the Base Vaca Muerta.

### 3.3 Low frequency model

Accounting for missing information below the seismic bandwidth is a critical issue in seismic inversion. This information is needed for qualitative interpretation; determination of absolute reservoir properties (Pendrel, 2015). This is why we need to build a Low-Frequency Model (LFM). The inputs into the LFM are the well logs with P-impedance (for post-stack inversion), and additionally S-impedance and density (for pre-stack inversion). These logs are filtered to fill the gap of the frequencies below those in the seismic data, and then are interpolated and extrapolated throughout the whole 3D volume, guided by the interpreted horizons.

The interpolation of the well log data has always been a fundamental issue in the LFM. Many analytical method can be used, such as inverse distance weighting or kriging. But without additional information, the truth is that we really do not know the lateral variability

of the reservoir below the seismic bandwidth (Pendrel, 2015). In situations of limited well control and with a large survey, such as this case study, this issue becomes all the more critical.

Driven by these considerations, in this study two sets of LFM's were generated: (a) *standard* models using conventional analytical interpolation techniques, and (b) *complex* models using advance methods that take into account lateral trends provided by the velocity field and the seismic data themselves.

### 3.3.1 Standard model

Jason<sup>TM</sup> software offers two main interpolation techniques that are applicable to the situation of sparse data that we are dealing with in this work: inverse distance-weighted and kriging. In inverse distance-weighted, the interpolation weights decrease with distance from the well, and are exactly zero at the other well positions. Global kriging is a geostatistical method of interpolating data using a linear combination of weights applied to the known data based on a model of spatial correlation (Sheriff, 2002). The type used here is simple kriging, in which the global mean is constant over the entire area and is generally based on all the control points (Sheriff, 2002). The software allows only for a spherical variogram model, but the user is allowed to specify the variogram range.

In order to determine which model to use, the predictive power of the interpolations was examined through blind well testing. Although in this case it was done on the LFM, the following explanation on how the blind well tests were performed applies for subsequent analysis done on the inversion results, and so it is important to show in some detail.

Blind well testing consists of the following steps:

1. Build the model with all wells in it.
2. Extract pseudo logs of the property (P-impedance or S-impedance) from this model at each well location.
3. Build the model again, this time removing one well.

4. Extract pseudo log of the property at the location of the removed well.
5. Compute the RMS difference between the *validated* and the *blind* pseudo logs, given by:

$$RMSD = \sqrt{\frac{\sum_{t=1}^N (Z_{val,t} - Z_{blind,t})^2}{N}} \quad (3.4)$$

where  $Z_{val}$  and  $Z_{blind}$  are, respectively, the impedance value of the validated and the blind pseudo logs at sample  $t$ , and  $N$  is the total number of samples of the pseudo-log in the interval of interest (Quintuco and Vaca Muerta).

6. Repeat steps 3 to 5 for the other three wells.
7. Compute the average value of the RMS difference for all four wells, thus obtaining the average RMS P-impedance error for the particular interpolation parameters.

Several variogram ranges were tried for the global kriging interpolation, but the shorter ranges (between 1,000 and 10,000 m) yielded changes that are too rapid given the little relative variability of impedance between wells. The two best ranges found were 12,000 and 30,000 m. These are compared with the default inverse-distance weighted algorithm, and the results are shown in Table 3.1.

Table 3.1: LFM blind well test results for standard interpolation methods.

Method	Average RMS error (kg/m <sup>3</sup> *m/s)	
	P-impedance	S-impedance
Inverse distance weighted	8.96 x 10 <sup>5</sup>	5 x 10 <sup>5</sup>
Global kriging (Range=12,000 m)	8.99 x 10 <sup>5</sup>	5.02 x 10 <sup>5</sup>
Global kriging (Range=30,000 m)	8.86 x 10 <sup>5</sup>	4.88 x 10 <sup>5</sup>

According to these numbers, the global kriging with a 30,000 m range shows a slightly lower error value for both P and S-impedance, signifying better predictive power. Figure 3.10 shows the well weights for this interpolation. Note the slow and smooth decay in the weights because of the large variogram range, indicating little spatial variability.

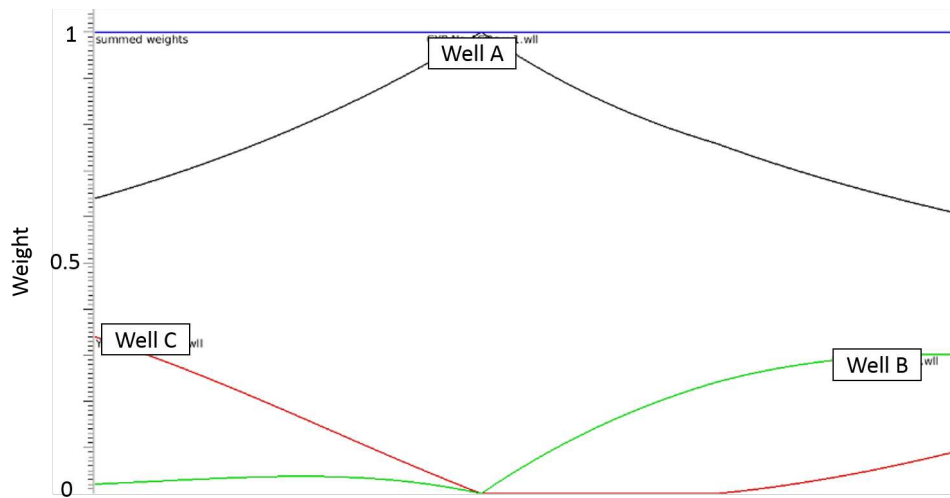


Figure 3.10: 2D section plot of well weights for global kriging (range=30,000 m).

### 3.3.2 Complex model

The software provides an option for applying user-defined weights that allow one to go beyond the standard interpolation techniques. These weights are built from *attribute horizons*, which can be derived from any lateral trend that the interpreter considers geologically meaningful. Each layer of the model will have an attribute horizon associated with it, from which the well weights are defined. For practical purposes, only three layers were chosen to generate these weights: Quintuco, Upper Vaca Muerta and Lower Vaca Muerta, the two latter bounded by the Middle Vaca Muerta horizon.

The attribute horizons are derived using all information available that might relate to lateral compaction trends or facies changes. The following attributes were used:

1. Structural trends from the time structure maps of the top of the layers.
2. Thicknesses of the layers.
3. Mean layer RMS amplitudes from the seismic data.
4. Mean layer migrations velocities.

5. Mean layer interval velocities obtained by applying the Dix equation to the migration velocity volume.

Each of these attributes generates an impedance model. Since every one of these models carries information about a certain lateral trend in the subsurface, they can be combined to generate a more geologically meaningful model. A good way to treat this is by the use of multi-attribute analysis. This is a process that builds a linear combination of attributes in order to calculate a property measured in the log, or target log. The attributes are selected according to the error in the prediction. The first attribute is the one with the highest correlation with the target log. The next attributes are those that add the least error. This process is known as *stepwise regression* (Vega, 2012). The Emerge module from Hampson-Russell™ software provides the tools for this analysis, and it offers the possibility to try non-linear transforms of the attributes as well.

Adding extra attributes always increases the correlation coefficient and decreases the error at the known well locations. However, if we apply a validation criteria, in which one well is extracted from the prediction and the errors computed at the blind well locations, the addition of more attributes will beyond some point increase the error. This is the criterion used for assessing the number of attributes to use.

Figure 3.11 and Figure 3.12 show the error plot for the calculation of the P-impedance and S-impedance models, respectively. Note that in both cases, the validation error decreases with the addition of attributes, meaning that the multi-attribute stepwise regression is increasing the predictive power of the models.

### 3.3.3 Qualitative comparison

Figure 3.13 shows the comparison in section view of the P-impedance low-frequency models generated with the standard interpolation and the stepwise regression approach. A 10 Hz high-cut filter was applied to both these models, as this value represents the low-frequency limit for the seismic survey. Figure 3.14 shows the same comparison for the S-

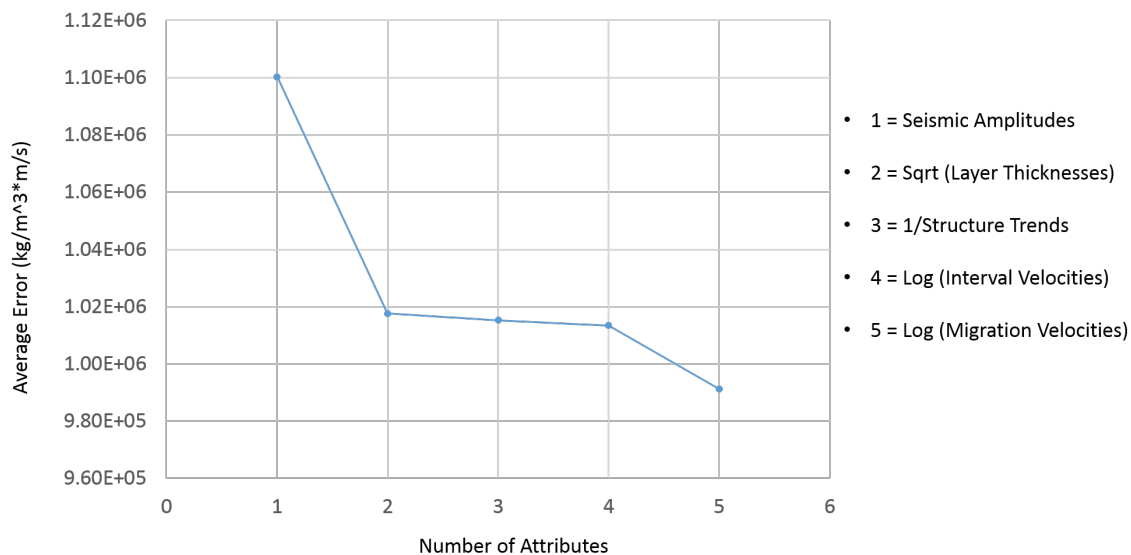


Figure 3.11: Stepwise regression error plot for the P-impedance model. The 2 in the x-axis means the use of attributes 1 and 2 listed on the right, the 3 means the use of attributes 1, 2 and 3, and so on.

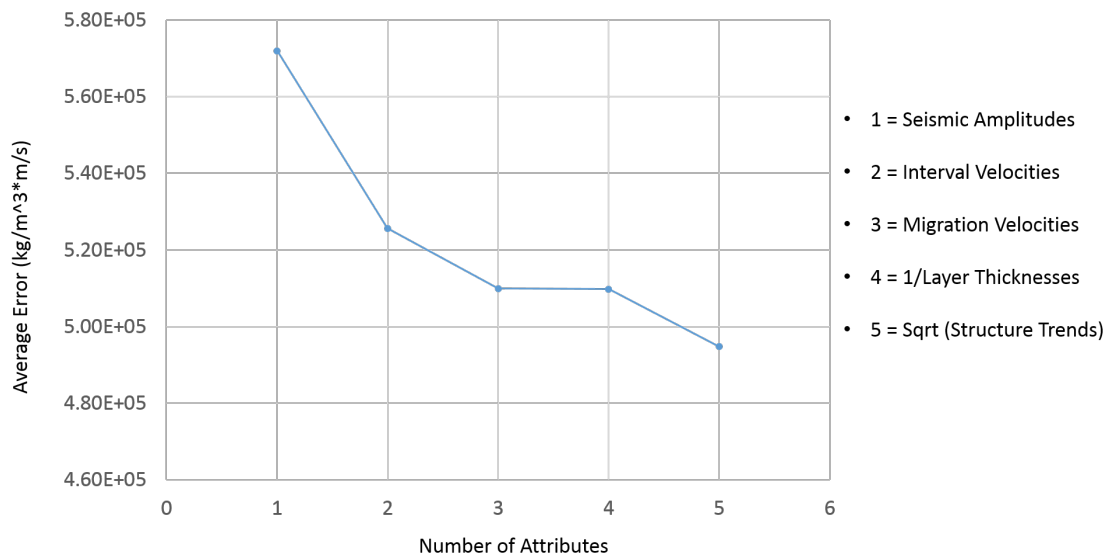


Figure 3.12: Stepwise regression error plot for the S-impedance model.

impedance models, also high-cut filtered to 10 Hz. There is a significant difference between the two models in terms of lateral variability. The complex models has sharper changes due to the local variation of the attributes. In contrast, the simple models are much smoother laterally.

The quantitative effect of these models on the inversion results will be analyzed in detail in the sensitivity analysis section on Chapter 4.

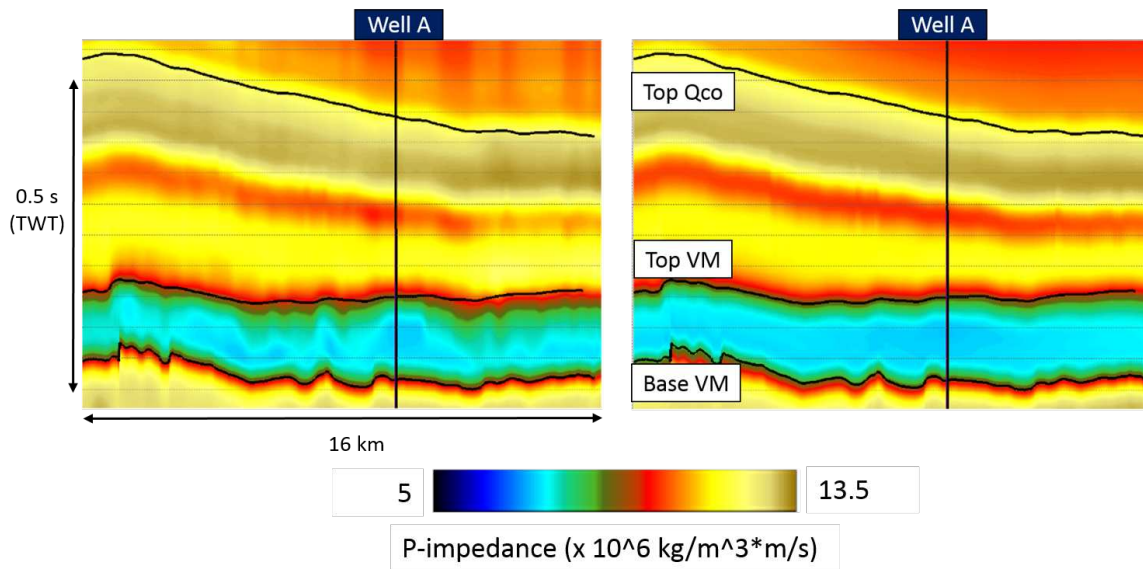


Figure 3.13: Inline of the P-impedance low-frequency models. Left: complex model. Right: standard model.

### 3.4 Post-stack inversion

This section presents the methodology for the inversion of the full stacked seismic dataset, with the objective of producing a P-impedance volume.

#### 3.4.1 Well tie and wavelet estimation

Seismic-well correlation and wavelet estimation is an iterative process that has the largest impact on the inversion results. It involves several updates to the well logs through shifts and stretch/squeeze operations, and updating the wavelet estimation parameters (MacFarlane, 2014).

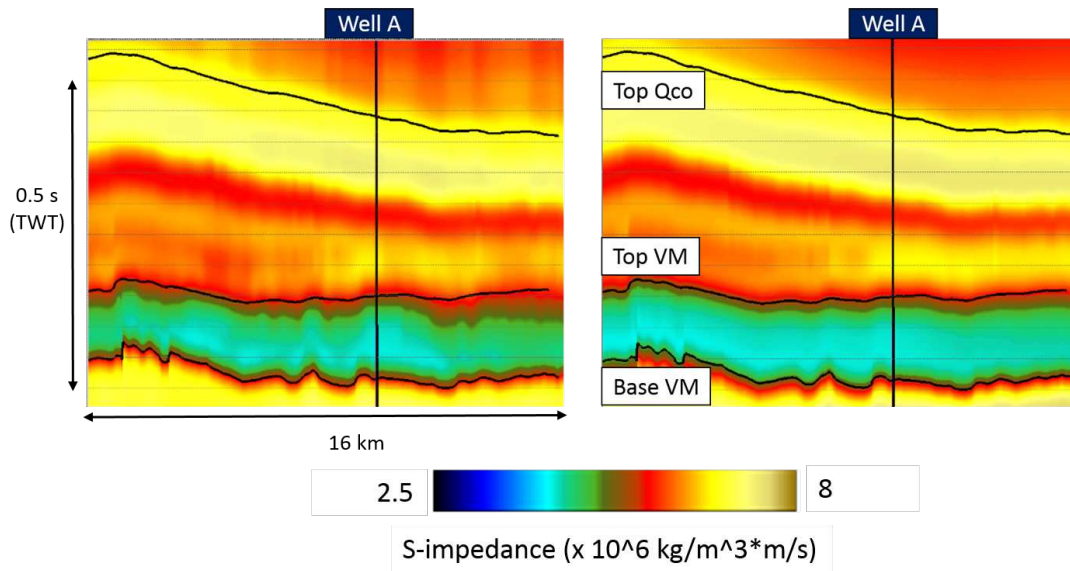


Figure 3.14: Inline of the S-impedance low-frequency models. Left: complex model. Right: standard model.

Well A is the only one with reliable check-shot data for building the time-depth curve. For the other wells, the filtered P-wave sonic logs were used. A first pass tie with a zero-phase wavelet was performed, and then refined by using techniques based on well reflectivity to estimate amplitude and phase of the wavelet simultaneously. This process was done for each well individually. After an optimal tie was achieved for each one, a *multi-well* wavelet was estimated using wells A and B, which yielded the best individual wavelets. Figure 3.15 shows the estimated wavelets displayed together. The final wavelet used for the well ties and the inversion is the multi-well wavelet.

The final well ties for the four wells are shown in Figure 3.16, Figure 3.17, Figure 3.18 and Figure 3.19. With the exception of Well C, all show an excellent seismic-synthetic match, with cross-correlation values of 0.7 or better. The match at Well C is much poorer because the dominant frequency of the seismic data in this area drops to around 30-35 Hz, in contrast with the rest of the survey, which is around 40-45 Hz.

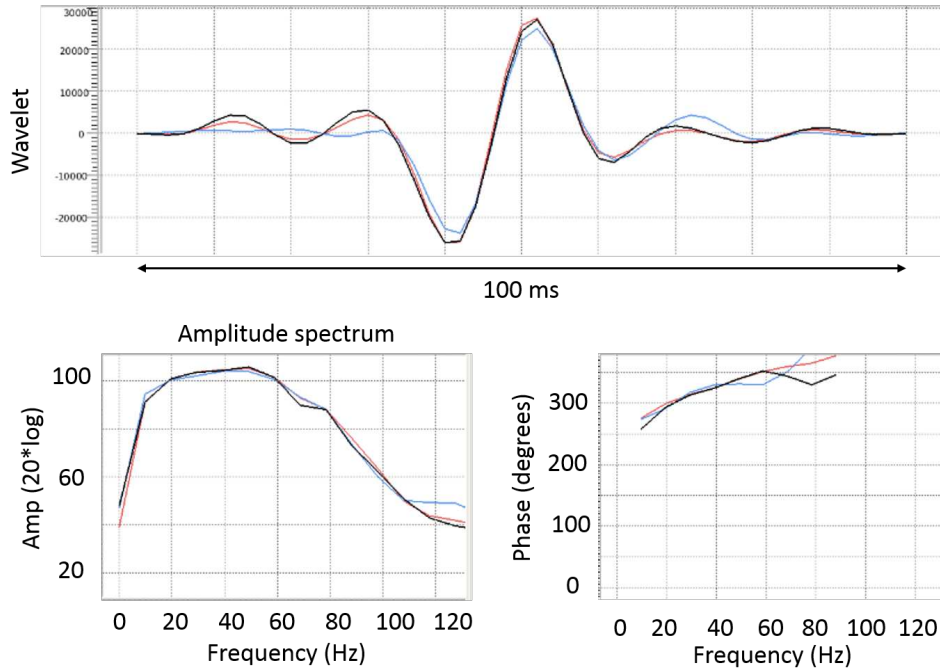


Figure 3.15: Wavelets estimated for the zero-offset well tie for post-stack inversion. Red: Well A wavelet. Blue: Well B wavelet. Black: multi-well wavelet.

### 3.4.2 Inversion parameters

To find the optimal settings for the misfit weights to use in the inversion, and therefore minimize the objective function, testing of the parameters and their impact on the results was done through different QCs. The weights are evaluated based on their capability to improve: signal-to-noise ratio, well log correlation, well log normalized standard deviation, and sparseness of the reflection coefficient (MacFarlane, 2014). Table 3.2 shows the main parameters used for the post-stack inversion.

Table 3.2: Post-stack inversion parameters.

Parameter	Value
Time window	Top Quintuco-Base Vaca Muerta
Seismic misfit signal-to-noise ratio	11.5 dB
Contrast misfit P-impedance uncertainty	1%
Wavelet scale factor	1
Merge cut-off frequency	10 Hz

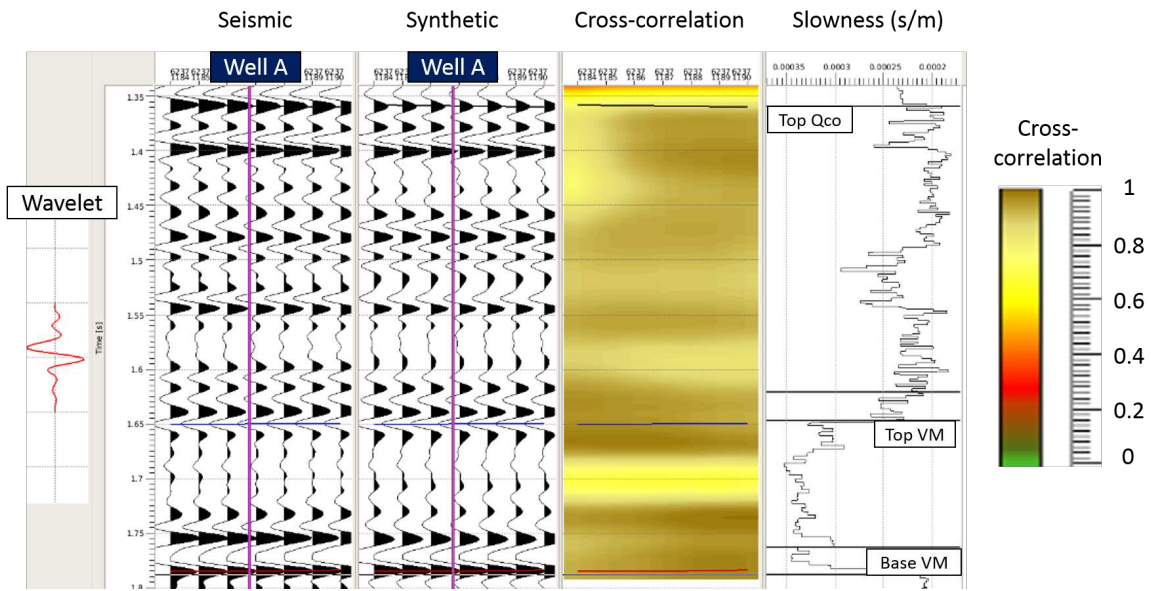


Figure 3.16: Full stack seismic-well tie for Well A.

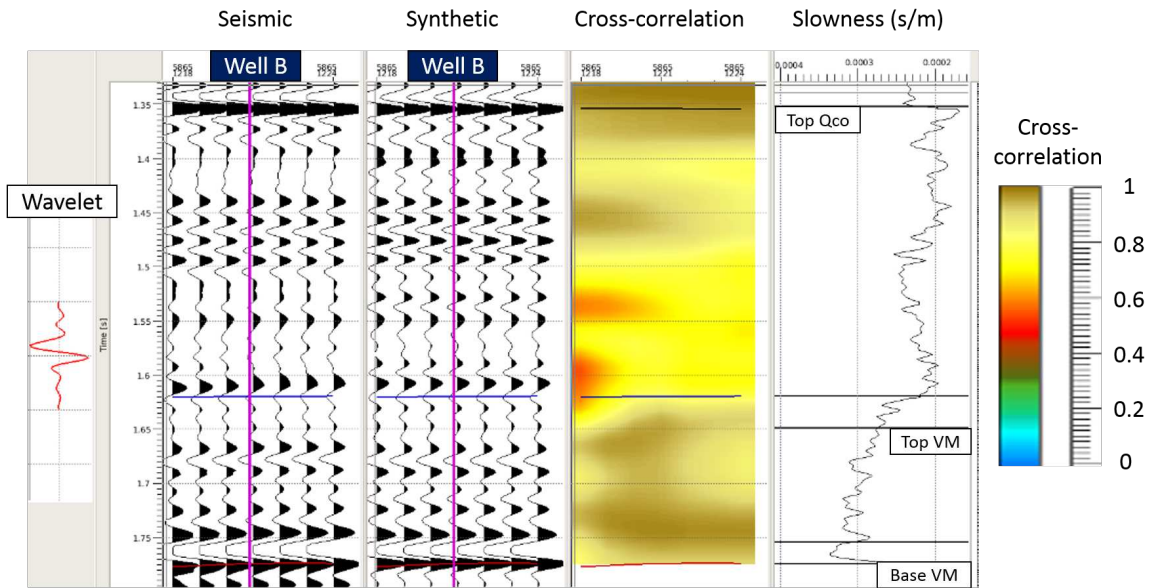


Figure 3.17: Full stack seismic-well tie for Well B.

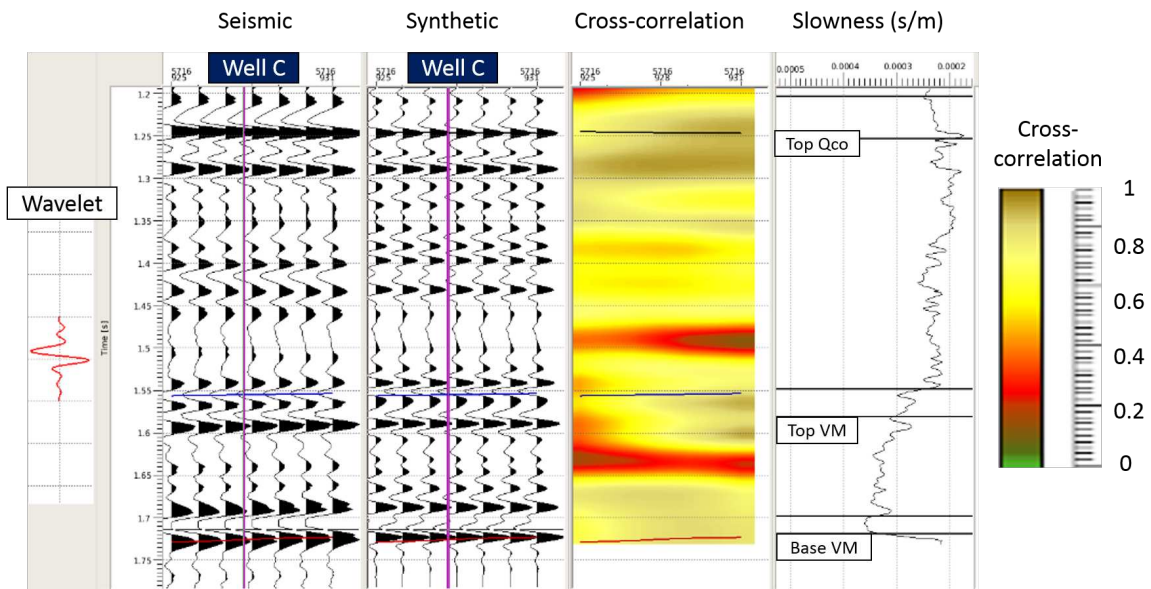


Figure 3.18: Full stack seismic-well tie for Well C.

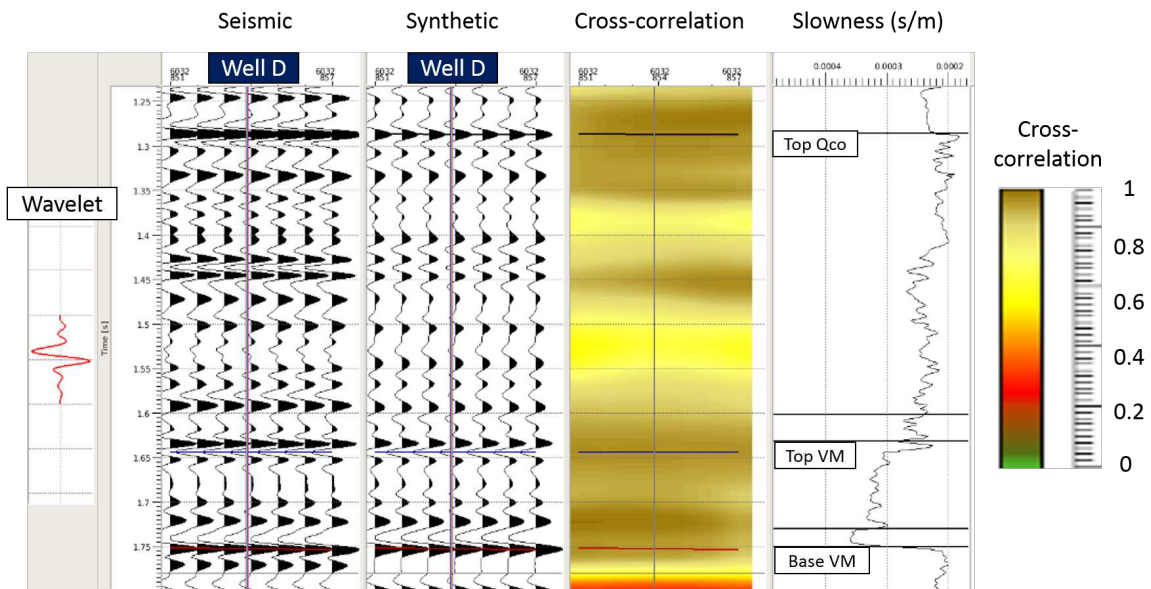


Figure 3.19: Full stack seismic-well tie for Well D.

One of the most important parameters is the merge cut-off frequency, which determines the overlap in the spectrum between the seismic and the low-frequency model. A value too high will cause an excessive imprint of the model, whereas a value that is too low will originate a gap in the bandwidth of the inversion results and thus degrade them. Figure 3.20 shows the bandwidth of the full stack with selected the merge frequency. Also shown is the bandpass filter applied to the inversion result. The high end of this filter should not be too high, as the inclusion of the higher frequencies will most likely bring noise to the results.

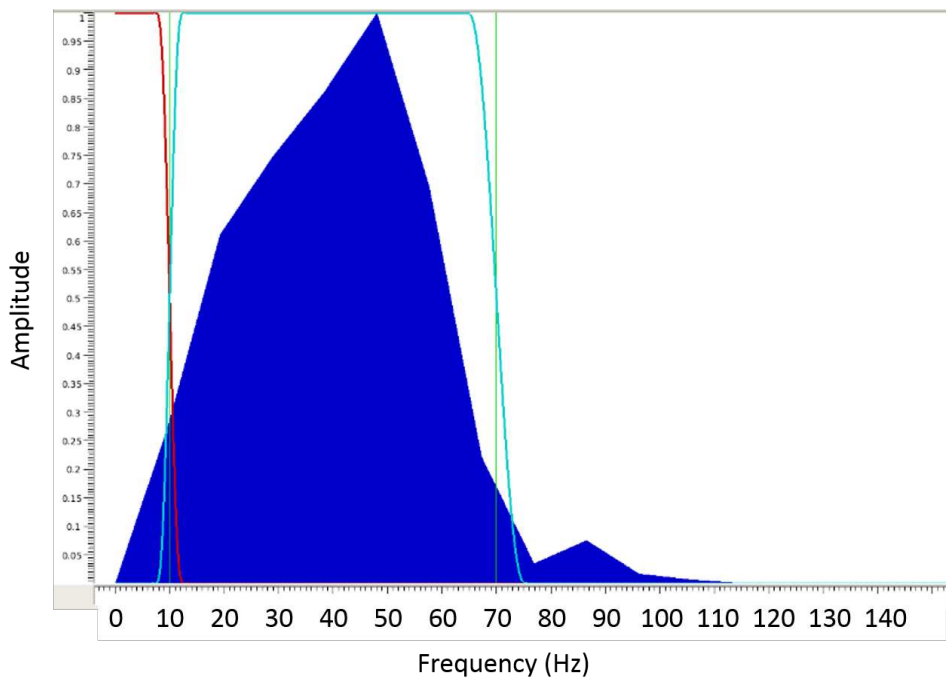


Figure 3.20: Bandwidth of the full stack. The high-cut filter applied to the low-frequency model is shown in red, and the bandpass filter applied to the post-stack inversion result is shown in cyan. The merge cut-off frequency is 10 Hz.

### 3.5 Pre-stack inversion

This section presents the workflow for the inversion of the angle stacks generated as explained in Chapter 2, with the goal to obtain P-impedance, S-impedance and, if possible, density volumes.

### 3.5.1 Well ties and angle-dependent wavelet estimation

The well ties and estimated wavelets in the post-stack inversion serve as a good starting point for this process on the partial angle stacks. Minor changes were made to optimize the well ties beginning with the Near stack in each well, and estimated the wavelets. A multi-well wavelet was defined for the Near stack. After this, the wavelets for the other three partial stacks were estimated, without the need to make further changes to the well tie time-depth curve because the time alignment of the stacks is good.

Figure 3.21 shows the final wavelets for the four partial angle stacks. The wavelets are consistent in the phase spectra. The far stack wavelet has slightly different amplitude spectrum than the others, with a lower frequency content. Aside from minor differences in side lobe energy, all the wavelets show a stable character throughout the angle ranges. The seismic-well ties for each stack for all wells are shown in Figure 3.22, Figure 3.23, Figure 3.24 and Figure 3.25, using the wavelets shown in Figure 3.21. Again, Well C shows problems. The match is poor, especially in the near angle stack. Aside from the change in frequency content previously discussed, the quality of the pre-stack gathers in this area is not good. With the exception of a few small areas, the seismic-synthetic match for Wells A, B and D is excellent for all stacks, with cross-correlation values mostly above 0.7.

### 3.5.2 Inversion parameters

The process of optimizing the parameters for pre-stack inversion is iterative. Because most parameters interact, comprehensive testing is needed to assess their impact on the inversion results. Moreover, the complexity of the process is much higher than for post-stack inversion because now we are inverting for three properties, which in turn interact with each other. Table 3.3 shows the main parameters used for the post-stack inversion. The rock physics constraints didn't show significant impact in the inversion and therefore were not used.

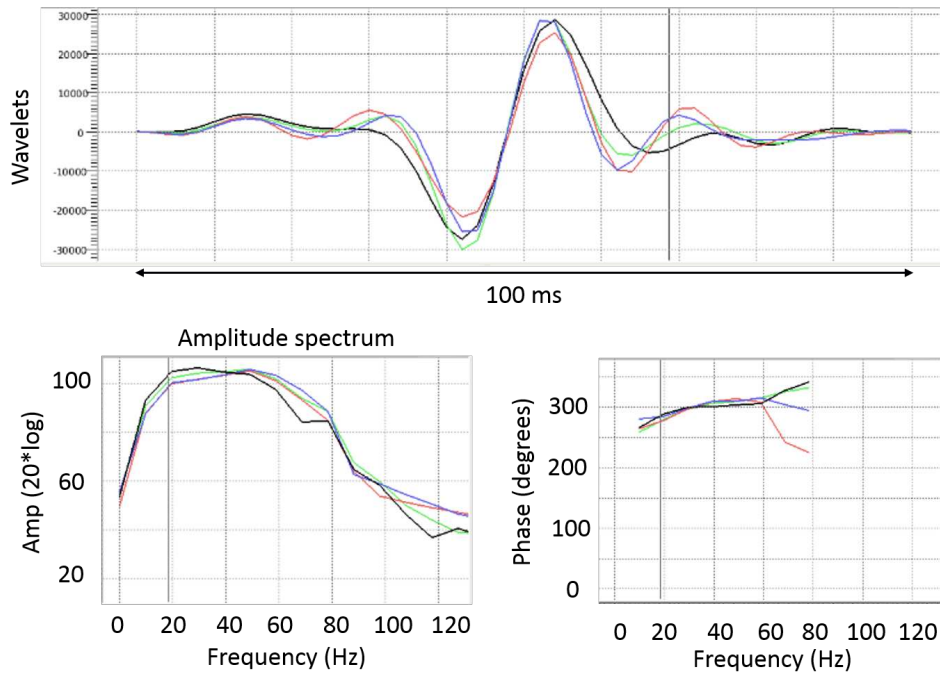


Figure 3.21: Wavelets estimated for each of the four partial stacks. Near stack: blue. Near-Mid stack: red. Mid-Far stack: green. Far stack: black.

Figure 3.26 shows the bandwidth of the Near stack with the merge frequency selected. Also shown is the bandpass filter applied to the inversion result. The merge cut-off frequency was selected based on the Near stack because it has the highest frequencies and we need to avoid the bandwidth gap.

### 3.6 Inversion results and quality control

In order to validate the inversion results and identify potential problem areas, several QC steps can be applied to the data, such as:

- Seismic-synthetic correlations.
- Section views of inverted results, both band-limited and full-bandwidth.
- Extracted pseudo-logs from the inverted volumes compared with the filtered well logs.
- Map extraction of inverted volumes for different levels of the Vaca Muerta.

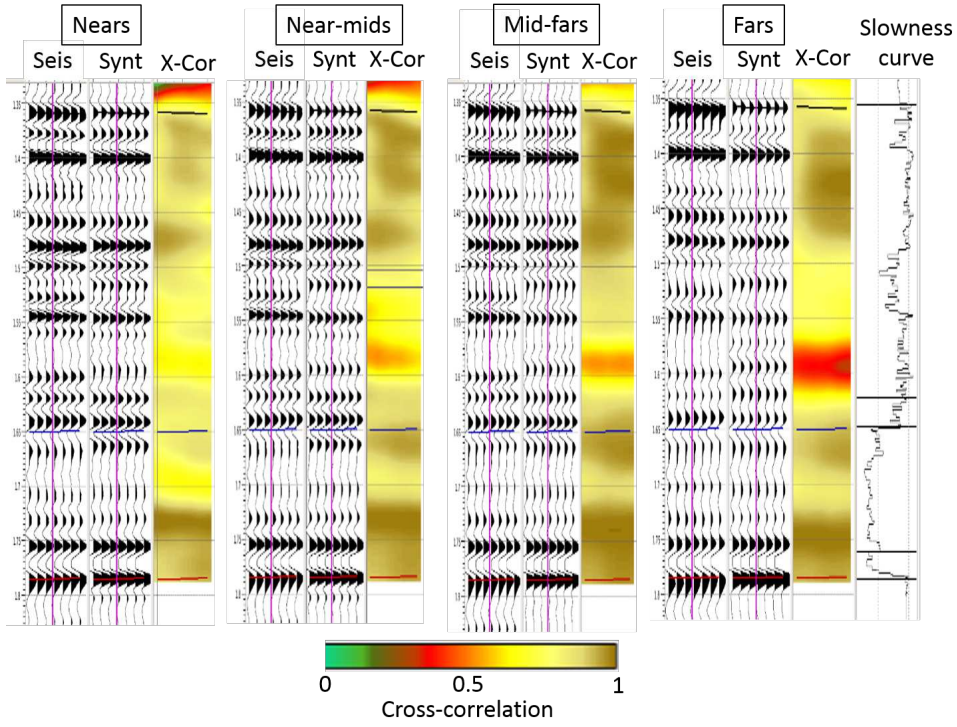


Figure 3.22: Well ties for partial angle stacks in Well A.

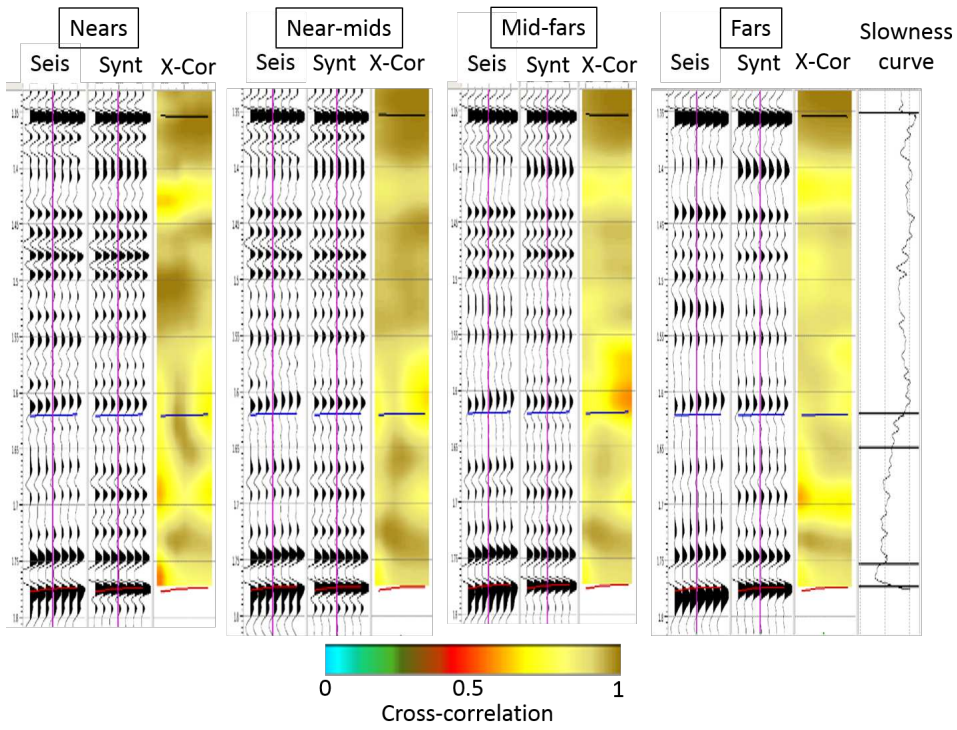


Figure 3.23: Well ties for partial angle stacks in Well B.

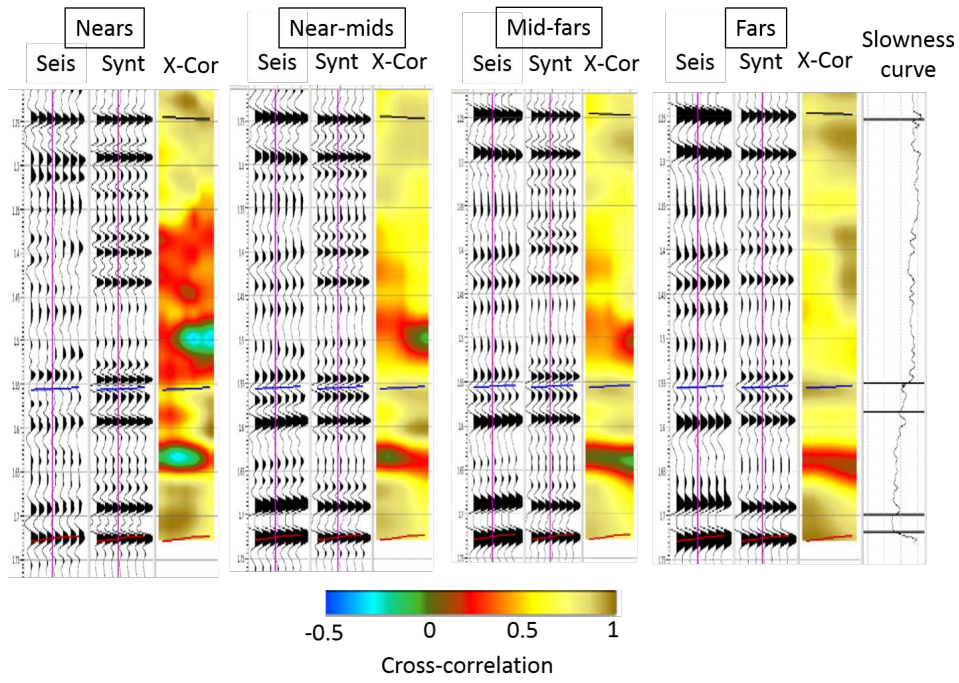


Figure 3.24: Well ties for partial angle stacks in Well C.

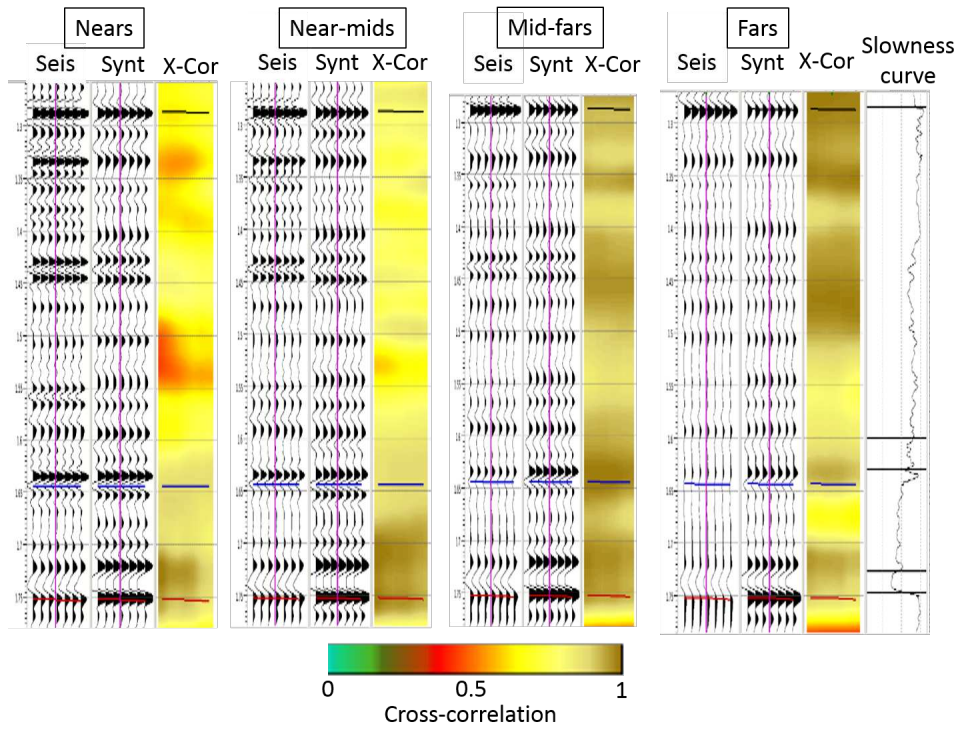


Figure 3.25: Well ties for partial angle stacks in Well D.

Table 3.3: Pre-stack inversion parameters.

Parameter	Value
Time window	Top Quintuco-Base Vaca Muerta
Merge cut-off frequency	10 Hz
Contrast misfit P-impedance uncertainty	1.6%
Contrast misfit S-impedance uncertainty	0.8%
Contrast misfit density uncertainty	0.4%
Seismic misfit signal-to-noise ratio (Nears)	17.9 dB
Seismic misfit signal-to-noise ratio (Near-Mids)	15 dB
Seismic misfit signal-to-noise ratio (Mid-Fars)	28.9 dB
Seismic misfit signal-to-noise ratio (Fars)	24 dB
Wavelet scale factor (Nears)	1.1
Wavelet scale factor (Near-Mids)	1.1
Wavelet scale factor (Mid-Fars)	1.1
Wavelet scale factor (Fars)	1.1

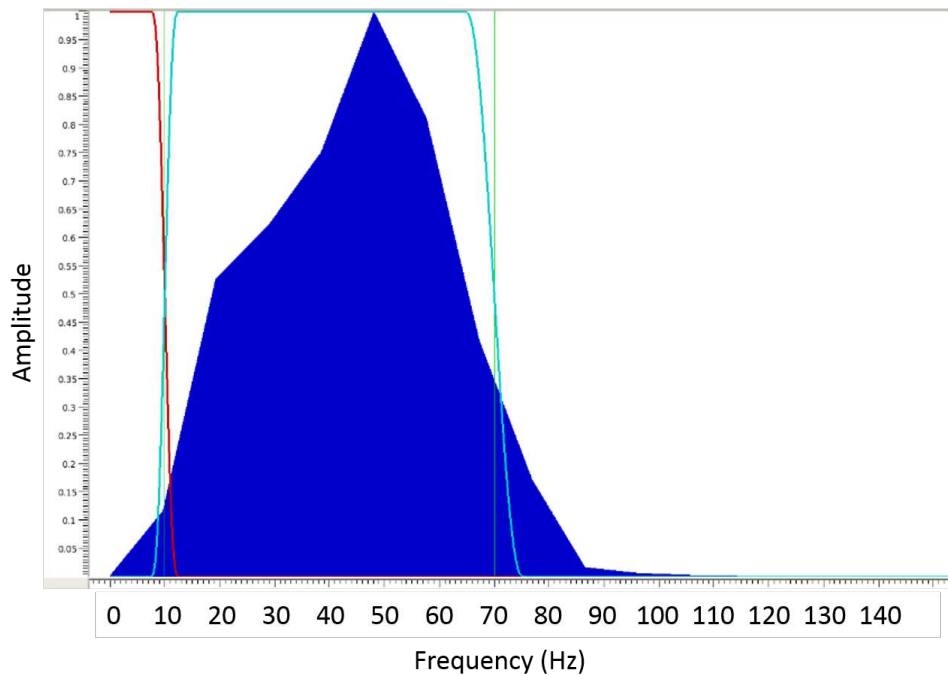


Figure 3.26: Bandwidth of the Near stack. The high-cut filter applied to the low frequency model is shown in red, and the bandpass filter applied to the pre-stack inversion result is shown in cyan. The merge cut-off frequency is 10 Hz.

Figure 3.27 shows the correlation between seismic and synthetic volumes for each of the four partial angle stacks. High correlation values mean low residuals and therefore a successful inversion. The correlation is high in the Mid-Far and Far stacks (above 0.95). In the Near-Mid stack, the correlation is still mostly above 0.9 although some areas around wells A and D drop to around 0.8. The only real problem area can be detected in the Near stack. The southwestern area of the survey, where Well C is located, shows a dramatic decrease in correlation values, some of them dropping below 0.6. This is because of the low quality of the gathers in this area, resulting in poor well ties. Therefore, in this area the inversion results cannot be considered reliable. The rest of the survey shows excellent results.

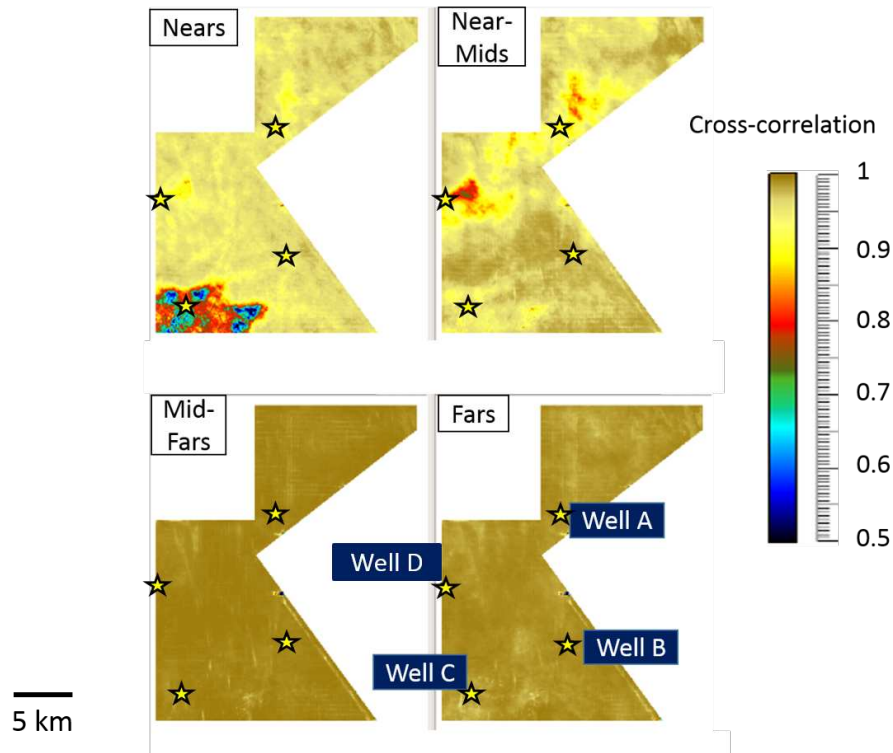


Figure 3.27: Maps of average seismic-synthetic correlation for the inversion window (Quintuco and Vaca Muerta) on each partial angle stack.

An important QC is the band-limited component of the inversion. This is the seismic data contributing, and this results speaks directly to the quality of the data and of the wavelet. Figure 3.28 shows vertical sections of the band-limited results on P-impedance for both post-

stack and pre-stack inversions. They show vertical and lateral contrasts in relative acoustic impedance. Also, they yield an excellent match with the filtered well log from Well A. The match is better for the post-stack in the lower Vaca Muerta, and in the upper Vaca Muerta and Lower Quintuco, the pre-stack results shows a somewhat more robust correlation.

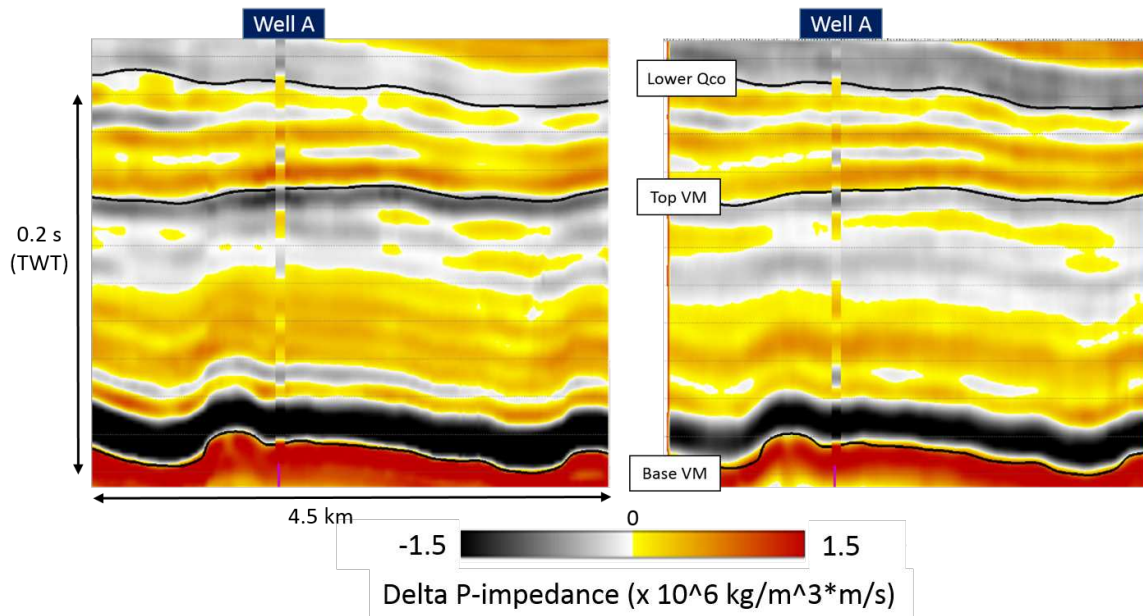


Figure 3.28: Inline of band-limited inverted P-impedance (10-70 Hz). Left: post-stack. Right: pre-stack. The well log has a 10-70 Hz bandpass filter.

Figure 3.29 shows the band-limited results for S-impedance. They are slightly more noisy than the P-impedance, because the pseudo-shear wave information from pre-stack inversion is more sensitive to noise. Nevertheless, the results show an excellent match with the filtered well log from Well A.

The full-bandwidth result of the inversion contains the combination of the seismic data and the low-frequency model. This result is key as it allows quantitative interpretation and estimation of geomechanical and reservoir properties. Figure 3.30 shows the full-bandwidth results on P-impedance for both post-stack and pre-stack inversions. They show the vertical trend of decreasing P-impedance with depth, and also lateral variations in certain layers. They show an excellent match with the filtered well log from Well A. Just as the band-

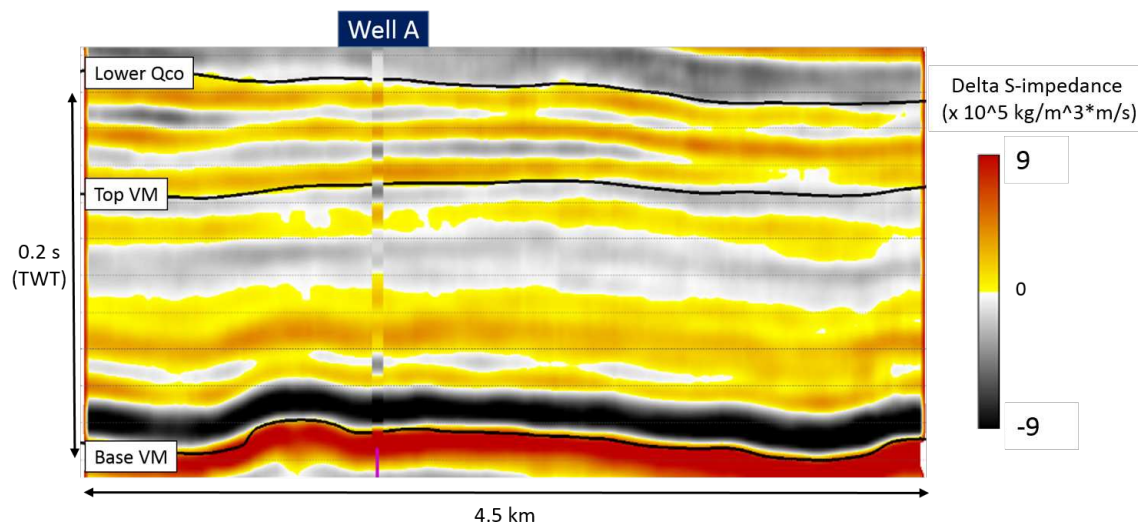


Figure 3.29: Inline section of band-limited inverted S-impedance (10-70 Hz). The well log has a 10-70 Hz bandpass filter.

limited results, the match is better for the post-stack in the lower Vaca Muerta, and in the upper Vaca Muerta and Lower Quintuco, the pre-stack has better correlation.

Figure 3.31 shows the full-bandwidth results for S-impedance. They also appear slightly noisier than the P-impedance results, but still with good quality and a good match with the filtered well log from Well A. The vertical decrease in S-impedance and the lateral variability is evident.

A more detailed comparison between log and inversion-derived impedance can be performed by extracting a pseudo-log of the inverted volume at the well location. Figure 3.32 shows the full-bandwidth P-impedance pseudo-logs, compared with the high-cut filtered well logs. Figure 3.33 shows the band-limited P-impedance pseudo-logs, together with the band-pass filtered log data. The matches are excellent for both post-stack and pre-stack in all wells except Well C, where there are important mismatches, especially in the Vaca Muerta.

The same analysis can be applied for the inverted S-impedance. Figure 3.34 and Figure 3.35 show comparisons for both full-bandwidth and band-limited results, respectively. As expected, the matches are not as excellent as the ones for P-impedance, but still are good. Some mismatch can be observed particularly in the Lower Vaca Muerta at wells B

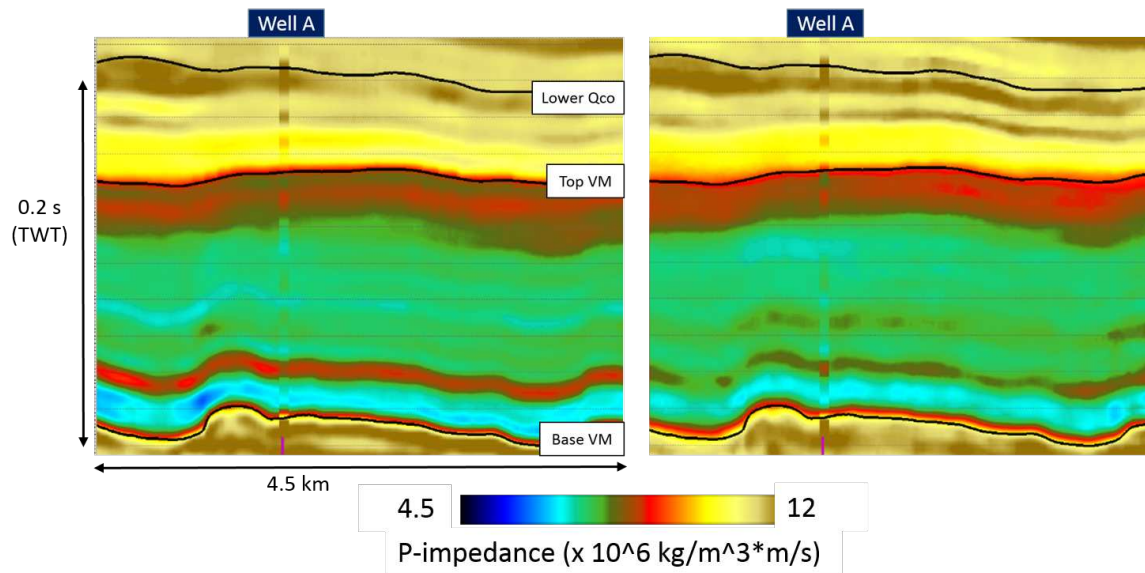


Figure 3.30: Inline of full-bandwidth inverted P-impedance (0-70 Hz). Left: post-stack. Right: pre-stack. The well log has a 70 Hz high-cut filter.

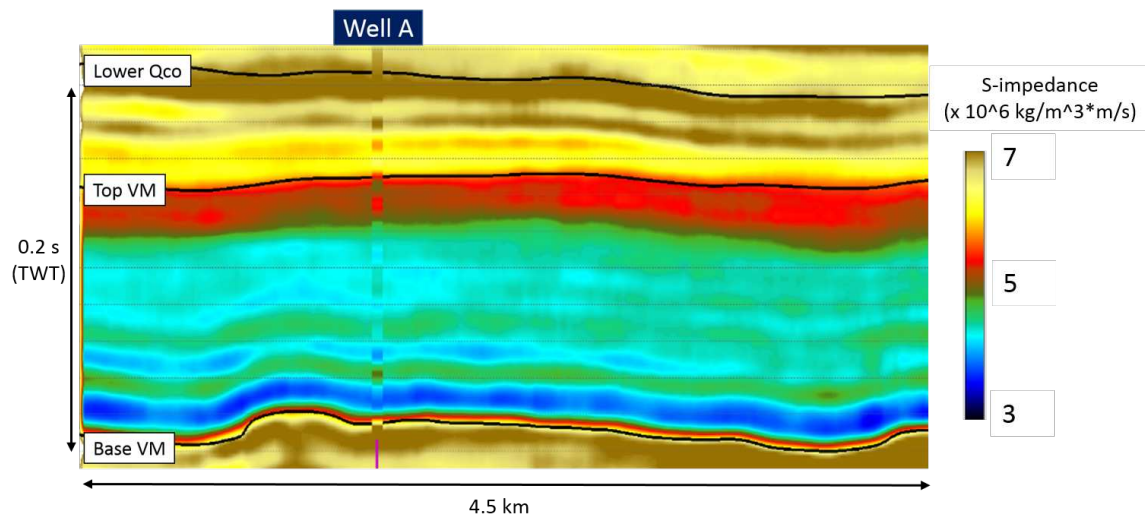


Figure 3.31: Inline of full-bandwidth inverted S-impedance (0-70 Hz). The well log has a 70 Hz high-cut filter.

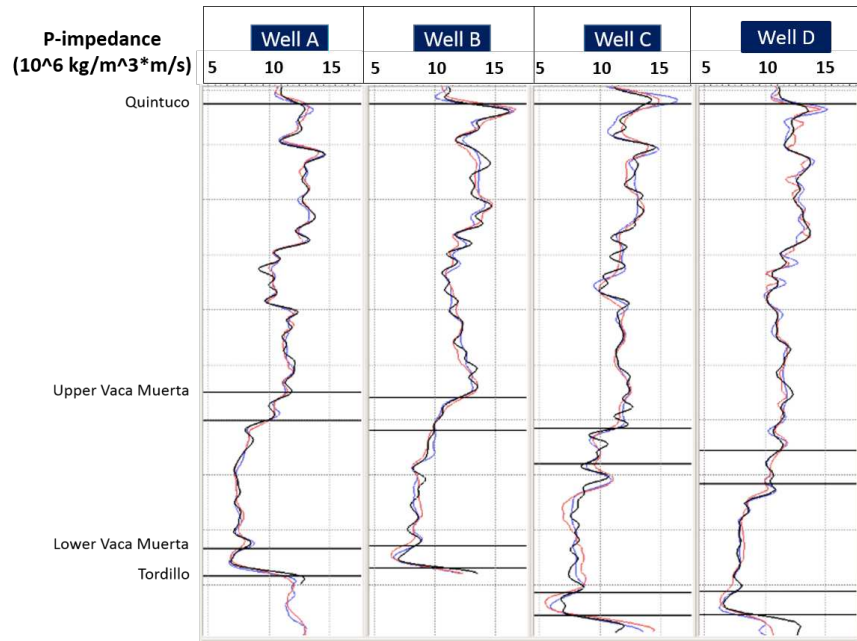


Figure 3.32: Pseudo-logs extracted from the full-bandwidth P-impedance post-stack (blue curves) and pre-stack inversion (red curves), compared with the high-cut (70 Hz) filtered well logs (black curves) for all wells.

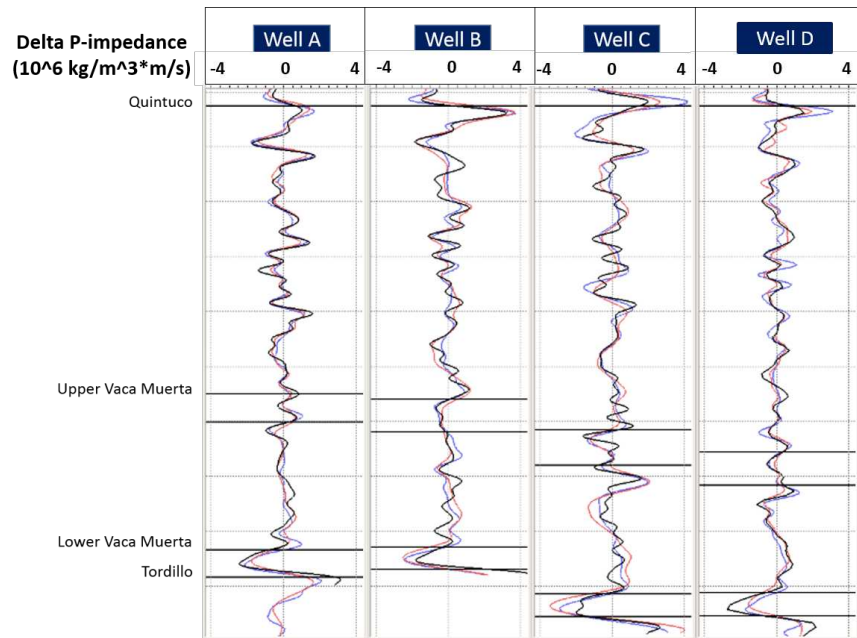


Figure 3.33: Pseudo-logs extracted from the band-limited P-impedance post-stack (blue curves) and pre-stack inversion (red curves), compared with the bandpass(10-70 Hz) filtered well logs (black curves) for all wells.

and D, where the inversion results underestimate the log values. Once again, Well C shows a poor correlation and therefore unreliable results in this area.

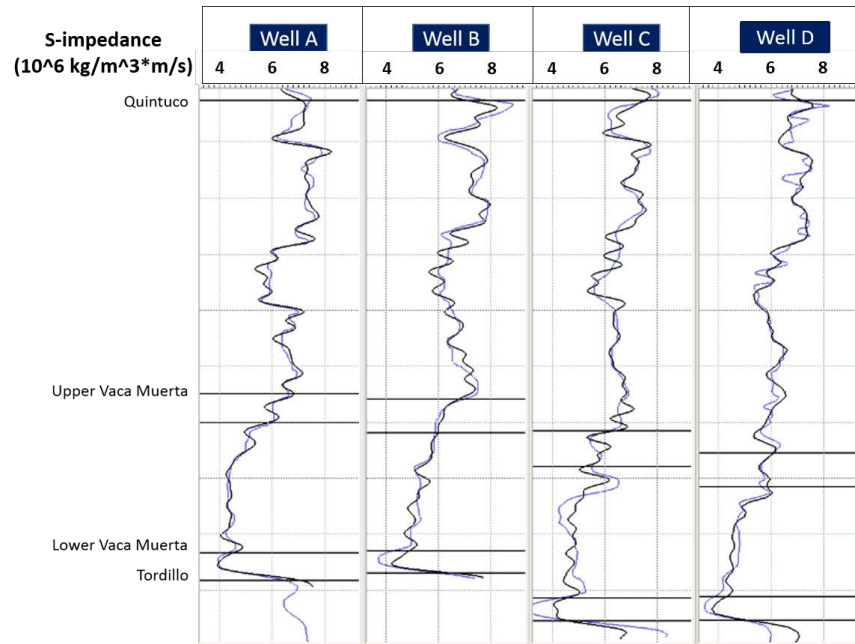


Figure 3.34: Pseudo-logs extracted from the full-bandwidth S-impedance inversion (blue curves), compared with the high-cut (70 Hz) filtered well logs (black curves) for all wells.

The lateral variability of the elastic properties derived from inversion is best observed in map view. RMS values of the P-impedance inverted volumes were extracted using small windows (10 ms), for three important levels: below the Top Vaca Muerta horizon, centered in the Middle Vaca Muerta horizon, and above the Base Vaca Muerta horizon. Figure 3.36 shows the horizon slices. The trends for both post-stack and pre-stack inversion results are similar, but the absolute values vary, especially in the Upper Vaca Muerta at the northeast area.

When comparing the P-impedance distribution at the different levels, important differences can be observed. The focus of the analysis is the area of interest to the northeast. In the Upper Vaca Muerta, the P-impedance is decreasing towards the north, while in the Middle Vaca Muerta, it is clearly increasing. The Lower Vaca Muerta does not show such a defined trend, with many smaller-scale variations in P-impedance.

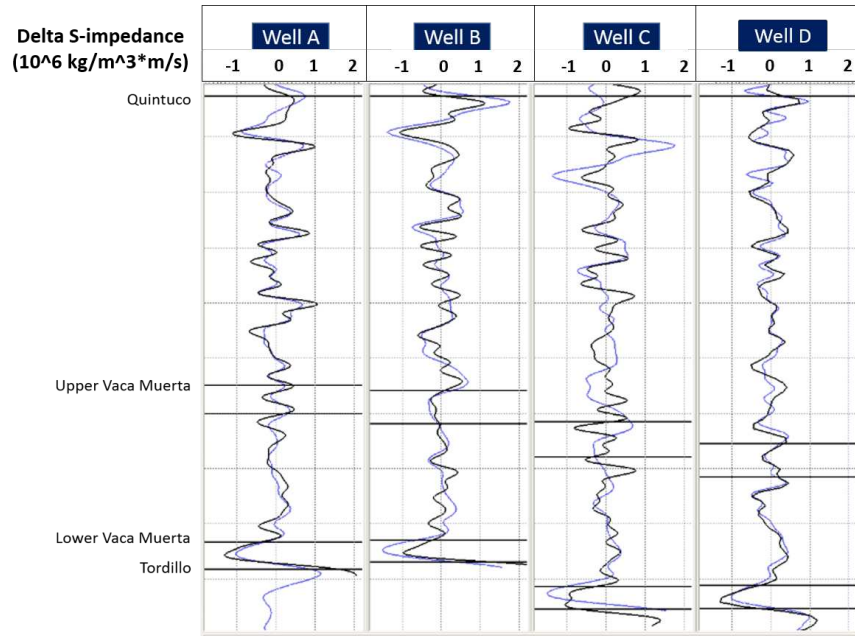


Figure 3.35: Pseudo-logs extracted from the band-limited S-impedance inversion (blue curves), compared with the bandpass(10-70 Hz) filtered well logs (black curves) for all wells.

Figure 3.37 shows the maps for S-impedance. The trends are similar to the results of the pre-stack P-impedance. This suggests that P and S-impedance are strongly correlated, resulting in a  $V_p/V_s$  ratio that might have small variability throughout the area. The implications for this will be analyzed in Chapter 5.

### 3.7 Summary

Post-stack and pre-stack inversions were performed for the regional 3D seismic survey focused on the Quintuco and Vaca Muerta. Two very different approaches for creating a low frequency model were implemented: a standard model using kriging interpolation, and a complex model using lateral trends of attributes and combining them through stepwise regression. These different methods provide the foundation for a more quantitative analysis that will be presented in Chapter 4.

The high quality of the data allowed for a successful inversion, as confirmed by the high seismic-synthetic correlation and the excellent match of the inversion results with the well logs. Exceptions for these were found in the southwest of the survey, where Well C is located.

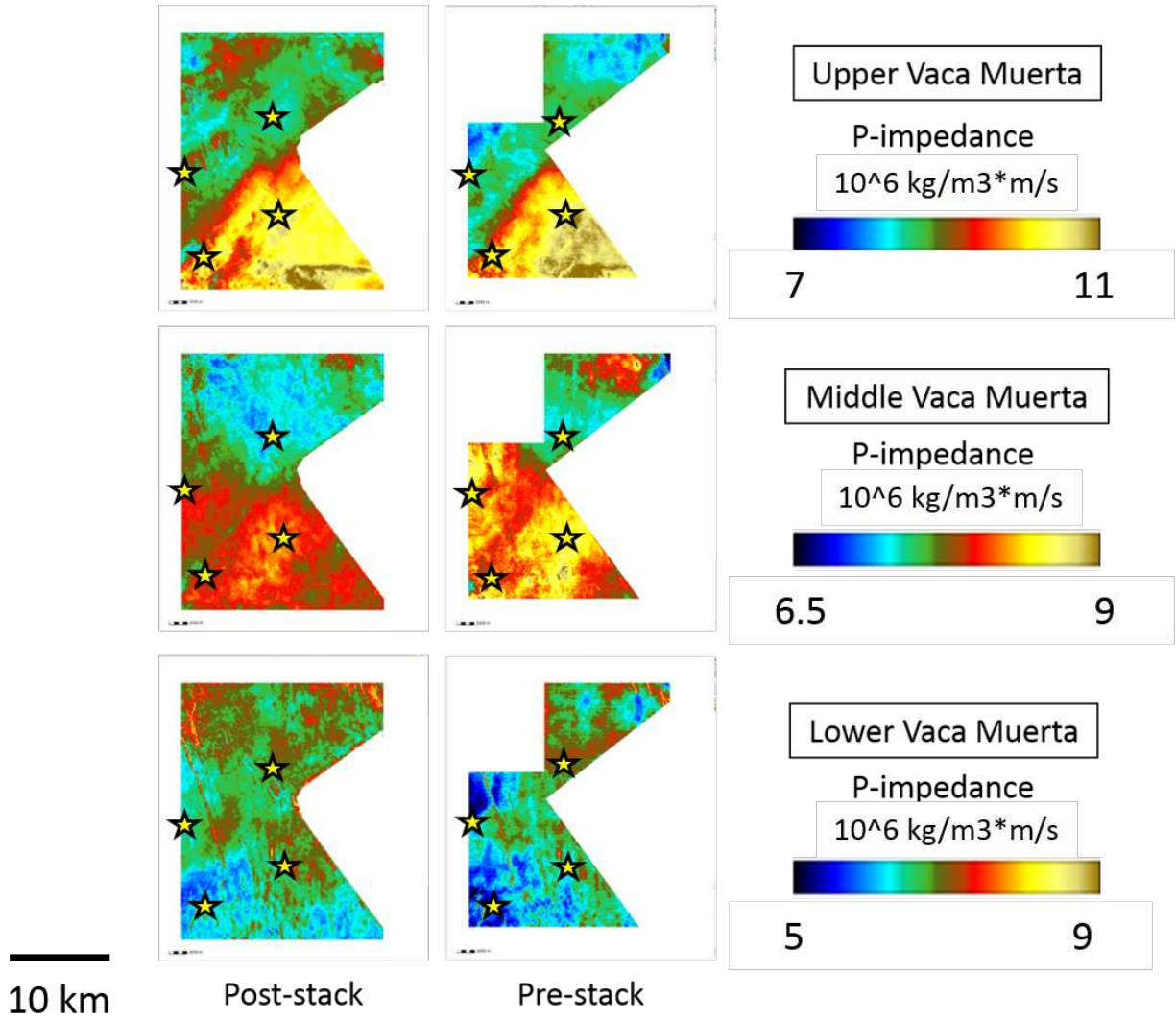


Figure 3.36: Maps of extracted P-impedance from post-stack and pre-stack inversion, for three main levels of the Vaca Muerta.

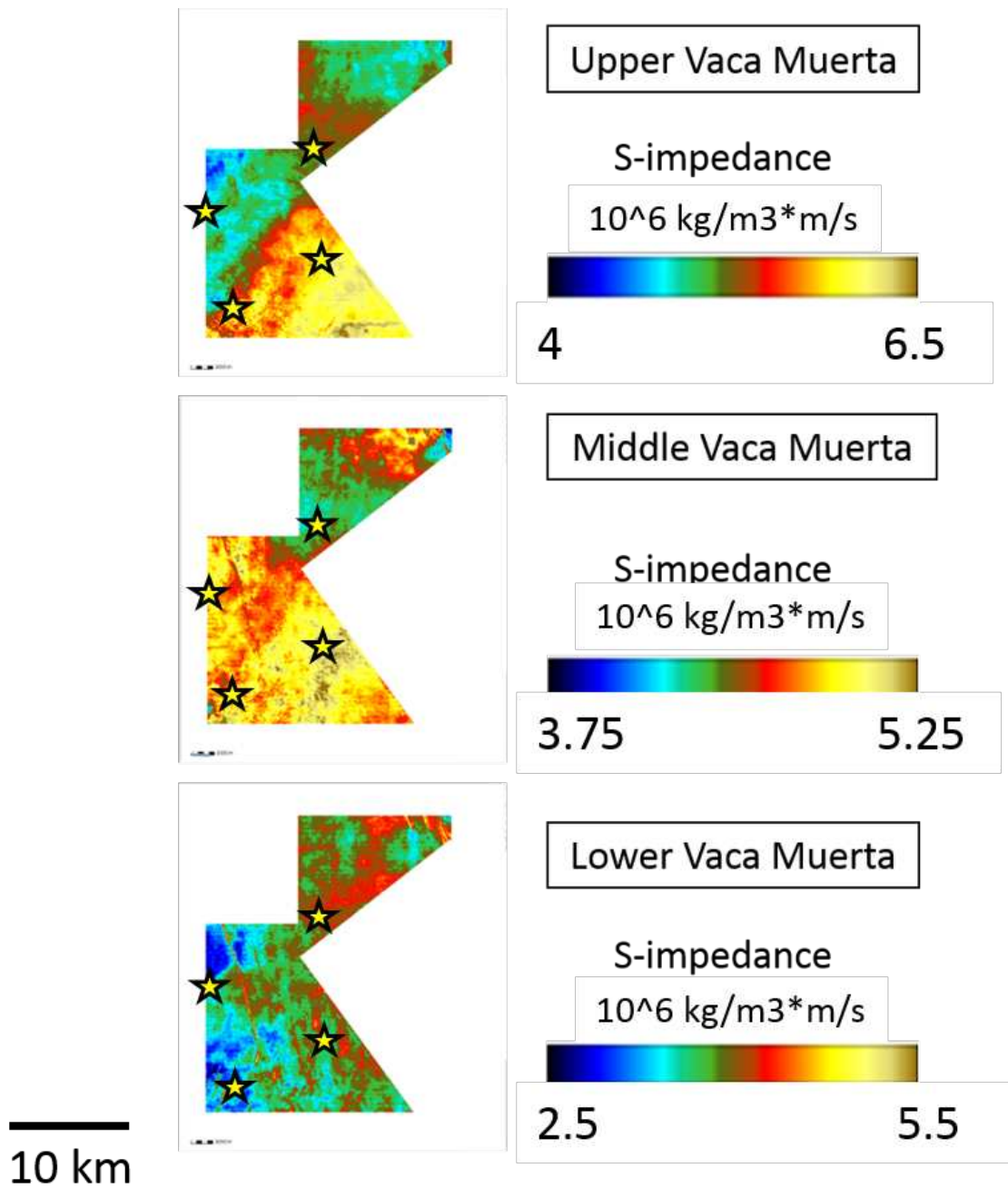


Figure 3.37: Maps of extracted S-impedance for three main levels of the Vaca Muerta.

This area has poor data quality, and therefore the inversion results here are unreliable. But for the rest of the survey, the inversion volumes can be confidently used for estimation of geomechanical and reservoir properties.

The differences in lateral trends of the elastic properties between the three main levels of the Vaca Muerta is seen in map view (Figure 3.36 and Figure 3.37). This is not surprising as the Vaca Muerta is a thick interval, influenced by different depositional cycles, where these variations are expected. The meaning of this variability in terms of reservoir characterization will be addressed in the interpretation and integration discussion in Chapter 5.

## CHAPTER 4

### SENSITIVITY ANALYSIS OF INVERSION RESULTS

Considering the characteristics of the data available, the results are subject to large uncertainties. A quite large seismic volume was inverted with very little well control, using an isotropic AVO approximation for pre-stack inversion in what clearly is an anisotropic formation.

This chapter has the objective of quantitatively comparing the results from the various inversion approaches and input data used. The calculation of the possible errors and their dependence on the model or algorithm is a fundamental step in this stage, where we are reducing uncertainty and starting to build predictive power in the reservoir and a geomechanical model of the study area.

#### **4.1 Post-stack versus pre-stack P-impedance**

As explained in the inversion theory section, pre-stack derived acoustic impedance has theoretical advantages with respect to post-stack. It is necessary, however, to quantitatively compare both results and draw conclusions on the practical aspects of using one or the other method. In subsection 3.3.2, the methodology for blind well testing was explained on the low-frequency model. Here, the same principle is applied, but now on the inverted volumes. The differences between the blind pseudo-logs extracted from the volume and the high-cut filtered well logs are computed for the RMS error calculation.

Figure 4.1 shows the comparison of the blind well tests for post-stack and pre-stack P-impedance. Note that Well C is not included in the tests because the inversion results in this area are not reliable, as was observed in Chapter 3. For Wells A and D, both pseudo-logs show a similar behavior, but in Well A they overestimate the values of the field-data log in most of the Upper Vaca Muerta, whereas for Well D the match is much better, with a slight overestimation in the Lower Quintuco. In Well B is where we can observe the greatest

differences for both logs; the post-stack pseudo-log shows a larger error in the Lower Vaca Muerta. Both logs underestimate the impedance values of the field-data log in the Lower Quintuco and the Upper Vaca Muerta.

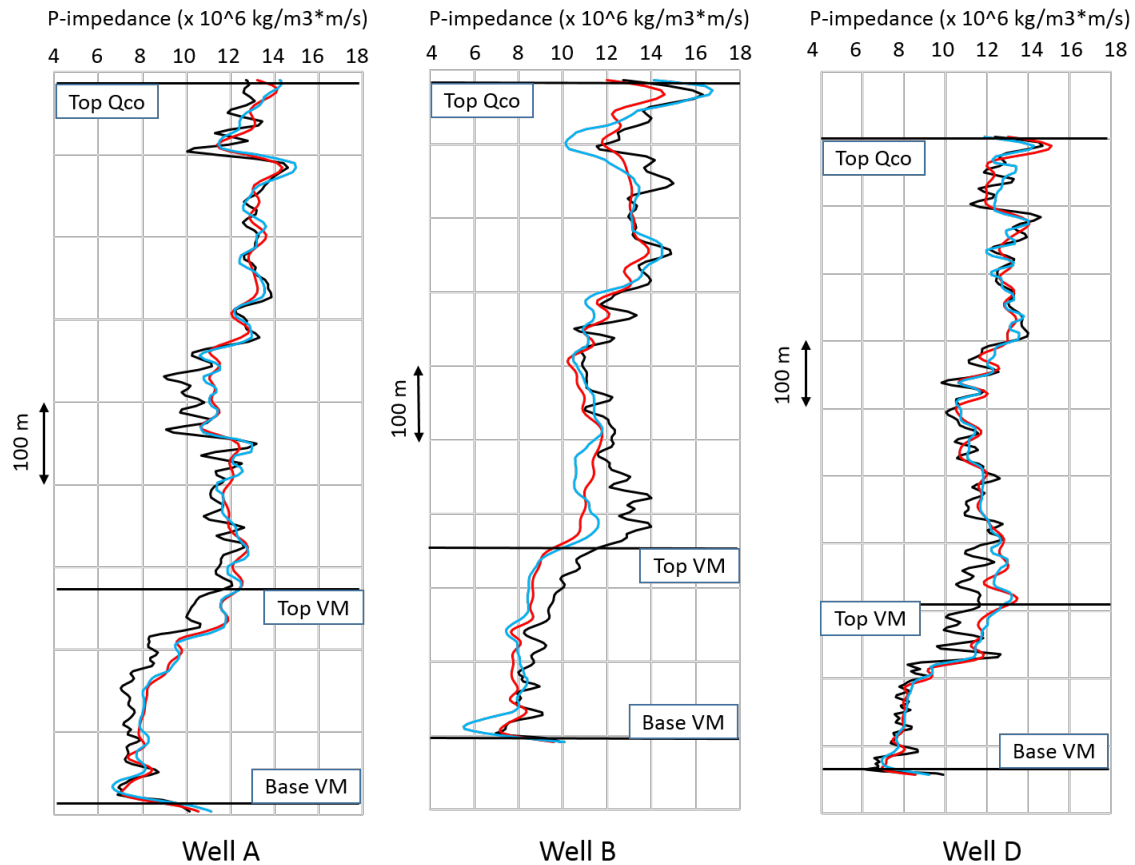


Figure 4.1: Blind well tests for post-stack P-impedance inversion (blue curves) and pre-stack P-impedance inversion (red curves) compared with the high-cut filtered P-impedance from the well logs (black curves).

In order to compare the RMS errors, it is more useful to do it in terms of percentage error, rather than absolute values. The percentage error simply comes from the ratio between the RMS error and the average impedance value for the interval. In Figure 4.2, the percentage error is quite low (less than 10 %) and similar for both methods. The higher error for post-stack P-impedance comes mostly from Well B.

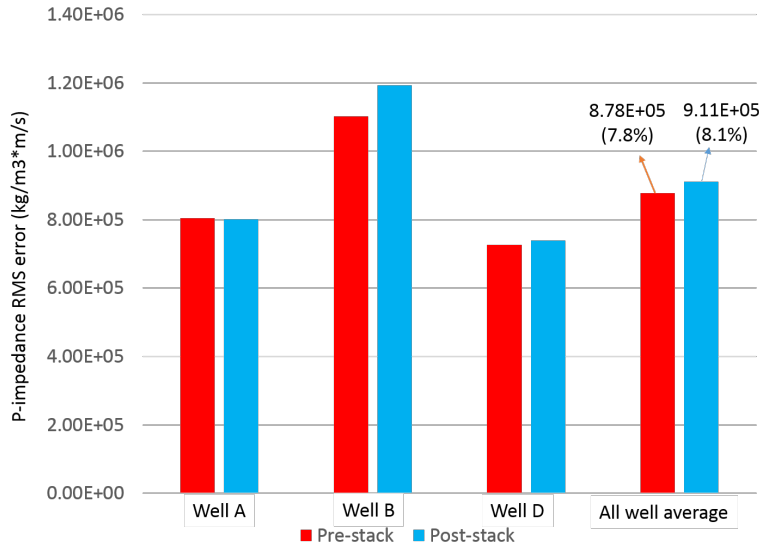


Figure 4.2: RMS errors of blind well tests for post-stack and pre-stack P-impedance inversion.

Both post-stack and pre-stack P-impedance derived from inversion yield good results for the study area. The advantage of pre-stack inversion is that the pseudo-shear information can be used for the estimation of geomechanical properties. But if the goal were only to characterize reservoir properties that correlate well with acoustic impedance, such as TOC or pore pressure, post-stack inversion would provide a robust tool to do it, being much less time-consuming and computer-intensive.

## 4.2 CSSI versus model-based inversion

Model-based pre-stack inversion was performed on the seismic dataset using Hampson-Russell™ software. The process will not be described in detail because all the important inputs for the CSSI were brought into the model-based inversion process. The same angle-dependent wavelets, time-depth curves (so the well ties are identical) and low frequency model were used. The difference is essentially in the algorithm and the inversion parameters. CSSI allows for more control on these parameters, whereas for the model-based process a few basic QCs were performed.

Since the interest is in the geomechanics of the Vaca Muerta, the comparison of these results is better done in the domain of these geomechanical properties rather than in the impedance domain. Poisson's ratio can be easily computed from the pre-stack inversion volumes using the following equation:

$$\nu = \frac{0.5 \left[ \frac{Z_P}{Z_S} \right]^2 - 1}{\left[ \frac{Z_P}{Z_S} \right]^2 - 1} \quad (4.1)$$

where  $Z_P$  and  $Z_S$  are the P and S-impedances, respectively.

Young's modulus is more complicated: to compute this property, the density is needed. As we saw in Chapter 3, this dataset does not allow for a reliable density solution. Sharma and Chopra (2012), however, propose an attribute called  $E\rho$ , which is nothing but the product of Young's modulus and density. The advantage of this property is that no density is needed for its calculation; it can be computed from the inversion results by the following equation:

$$E\rho = 2(Z_S)^2(1 + \nu) \quad (4.2)$$

Figure 4.3 shows the comparison of the blind well tests for Poisson's ratio. The main difference between the two pseudo-logs can be observed in the lower Vaca Muerta (Wells A and D) and the upper part of the Quintuco (Well B). Aside from localized differences in the high-frequency character of the curves, the behavior of both pseudo-logs is similar in general terms. The RMS percentage error is almost the same for both methods, with only a slight advantage in the model-based inversion (Figure 4.4).

Figure 4.5 shows the comparison of the blind well tests for the product  $E\rho$ . The behavior of both pseudo-logs is similar. The difference is mainly in the frequency content of the curves, the model-based derived pseudo log being of higher frequency. The RMS percentage error is also almost identical for both methods, this time with a slight advantage of the CSSI inversion (Figure 4.6).

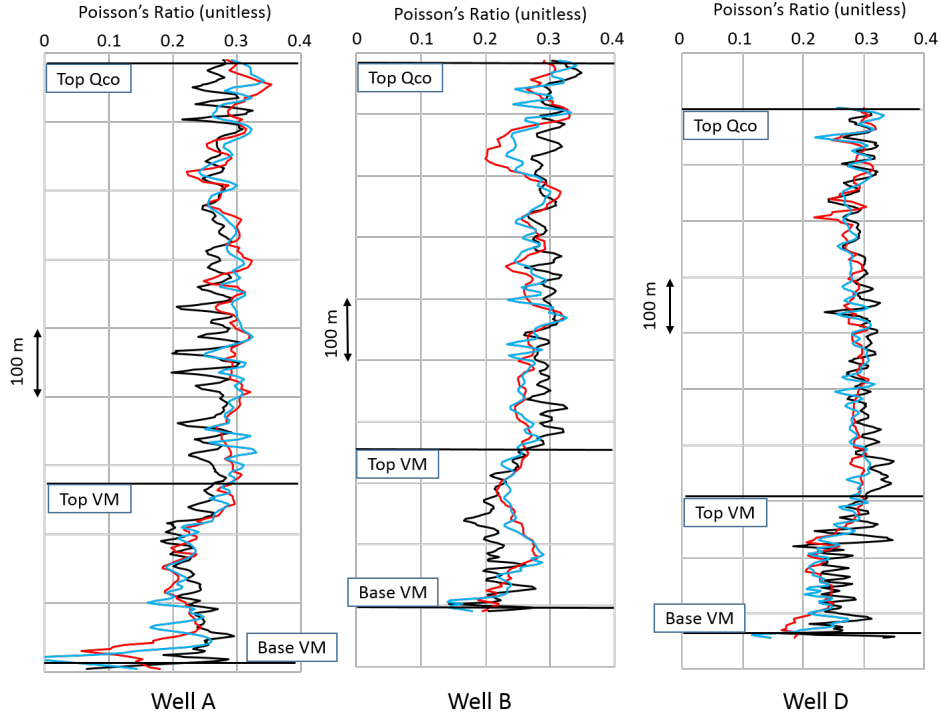


Figure 4.3: Blind well tests for model-based Poisson's ratio (blue curves) and CSSI Poisson's ratio (red curves) compared with the high-cut filtered Poisson's ratio from the well logs (black curves).

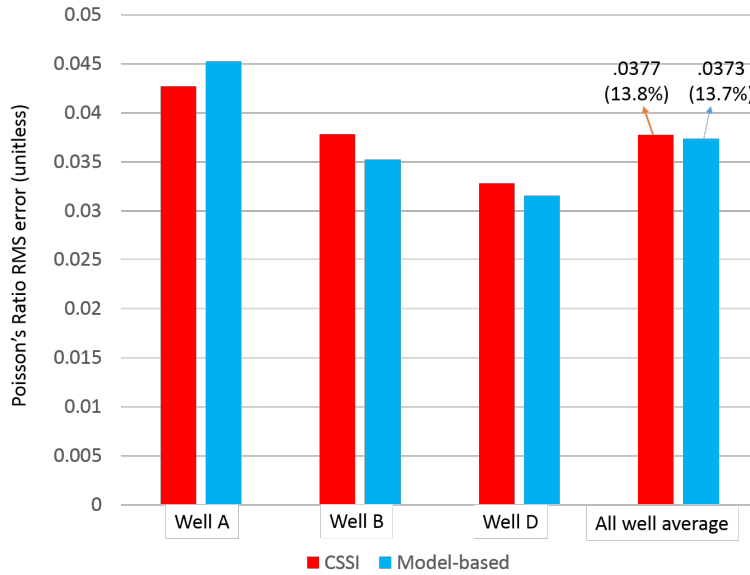


Figure 4.4: RMS errors of blind well tests for model-based and CSSI derived Poisson's ratio.

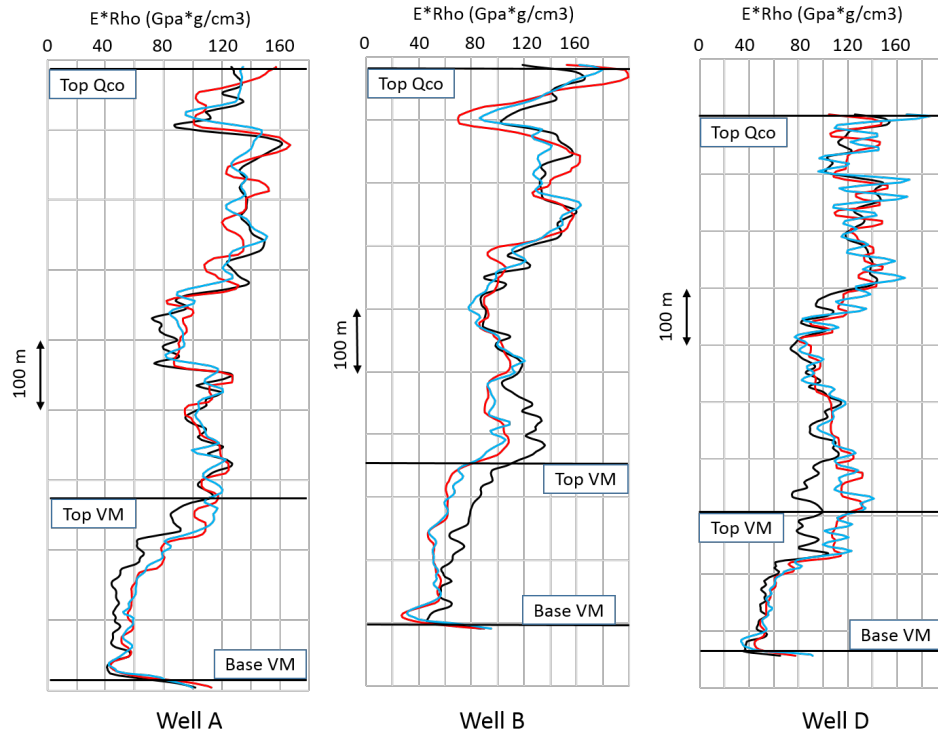


Figure 4.5: Blind well tests for model-based  $E\rho$  (blue curves) and CSSI  $E\rho$  (red curves) compared with the high-cut filtered  $E\rho$  from the well logs (black curves).

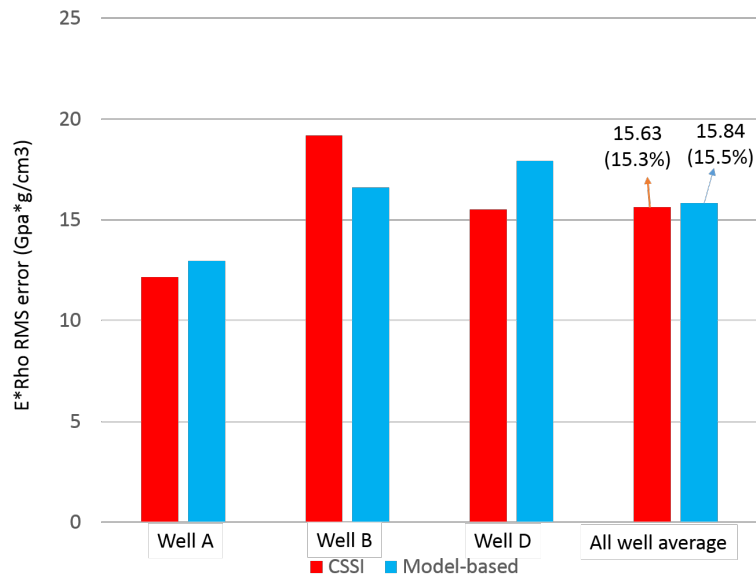


Figure 4.6: RMS errors of blind well tests for model-based and CSSI derived  $E\rho$ .

The geomechanical properties derived from pre-stack inversion for this study area, are not highly sensitive to the inversion algorithm used. Either one could be employed depending on user preference or software availability, and the results will be suitable for a geomechanical model.

### 4.3 Standard LFM versus Complex LFM

As in the previous section, the domain of comparison is the geomechanical properties. In here, the results of pre-stack CSSI using two different low-frequency models are compared. The wavelets, well ties and inversion parameters are kept identical for both cases.

Figure 4.7 shows the comparison of the blind well tests for Poisson's ratio. The pseudo-logs from the standard model show a good match with the well logs for most parts on the well, except in the upper Quintuco and middle Vaca Muerta in Well B, and the lower Quintuco in wells A and D. The pseudo-logs from the complex model show more mismatch. They drastically underestimate the Poisson's ratio values from the well logs in the Lower Vaca Muerta for wells A and D, and overestimate these values in the middle Vaca Muerta for Well B, with a noticeably higher error than the standard model. The RMS percentage error is more than 1% lower for the standard than for the complex model, and the errors are more evenly distributed for the three wells (Figure 4.8).

Figure 4.9 shows the comparison of the blind well tests for  $E\rho$ . The differences between the pseudo-log for the standard model and the complex model are much less than for Poisson's ratio. Both pseudo-logs overestimate the values in the upper Vaca Muerta for Well A, and the lower Quintuco for Well D, and underestimate them for both the lower Quintuco and upper Vaca Muerta for well B. The largest error in the complex model can be seen in Well B at the upper Quintuco. The RMS percentage error is also more than 1% lower for the standard model than for the complex model, the difference coming mostly from the errors on Well B (Figure 4.10).

Based on these results, the low frequency model has the largest impact on the geomechanical properties derived from seismic inversion. The LFM has control on the absolute

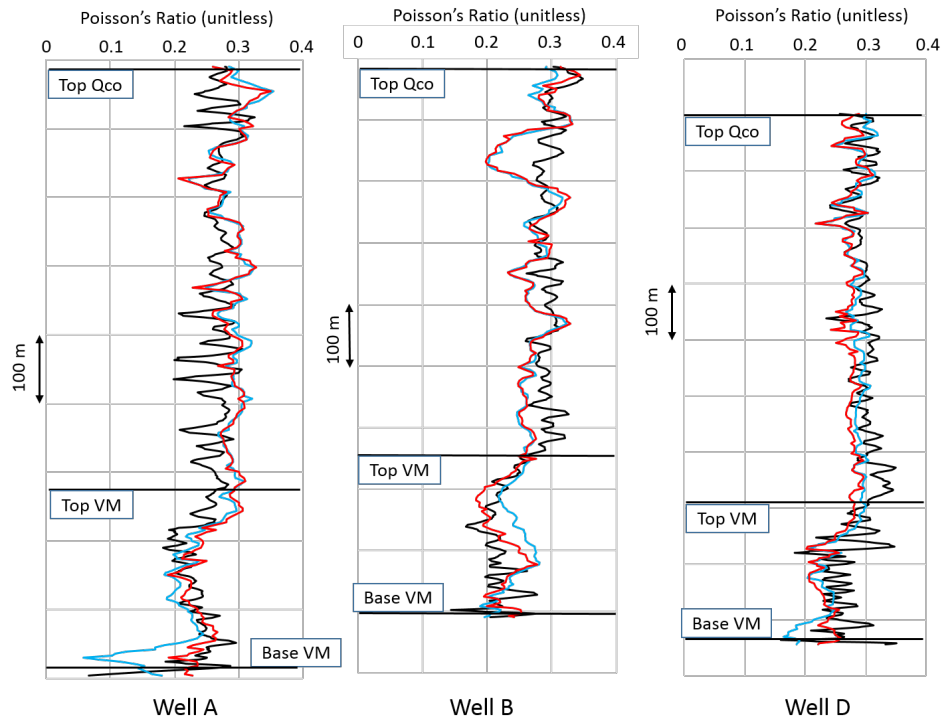


Figure 4.7: Blind well tests for Poisson's ratio obtained from inversion with the standard LFM (red curves) and the complex LFM (blue curves) compared with the high-cut filtered Poisson's ratio from the well logs (black curves).

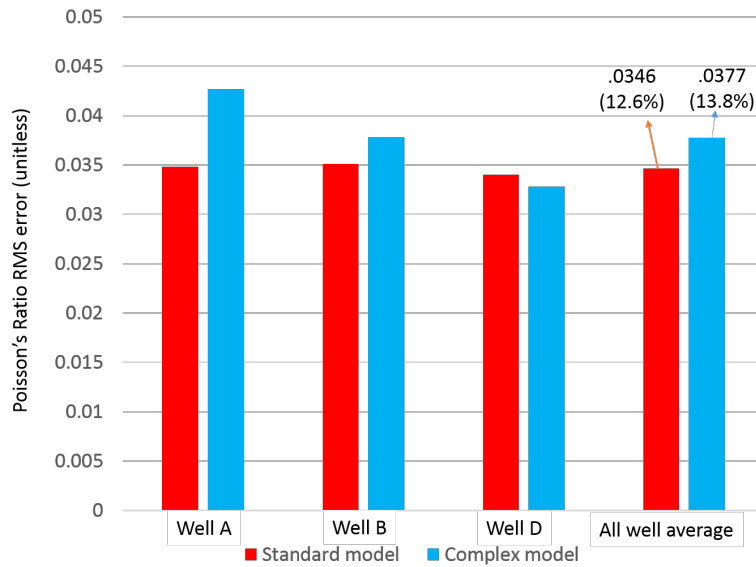


Figure 4.8: RMS errors of blind well tests for Poisson's ratio from the standard and complex low frequency models.

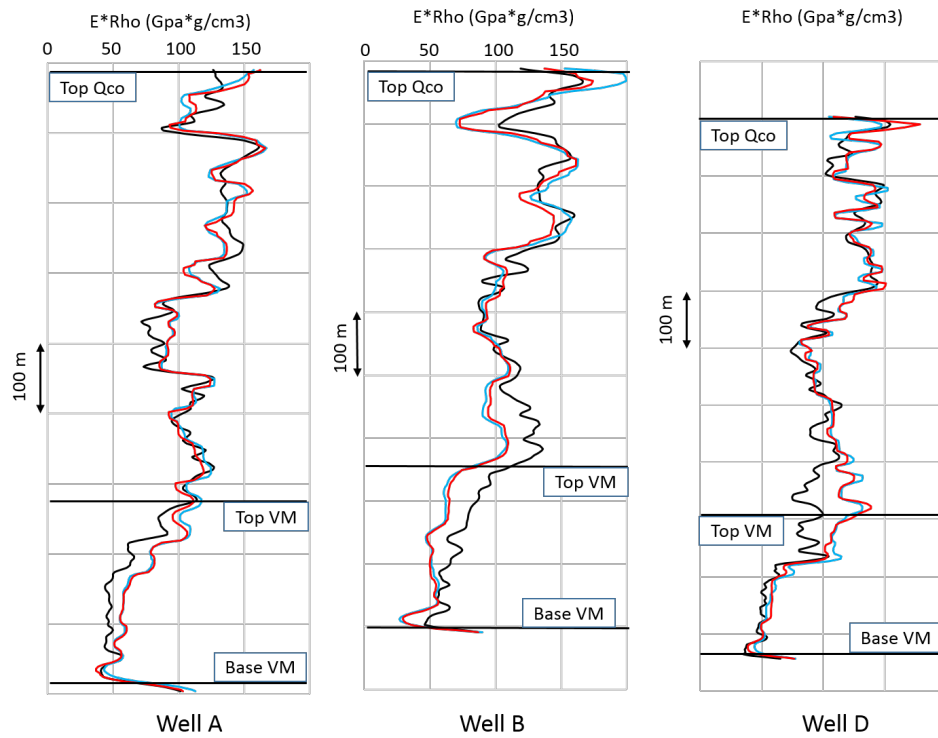


Figure 4.9: Blind well tests for  $E\rho$  obtained from inversion with the standard LFM (red curves) and the complex LFM (blue curves) compared with the high-cut filtered  $E\rho$  from the well logs (black curves).

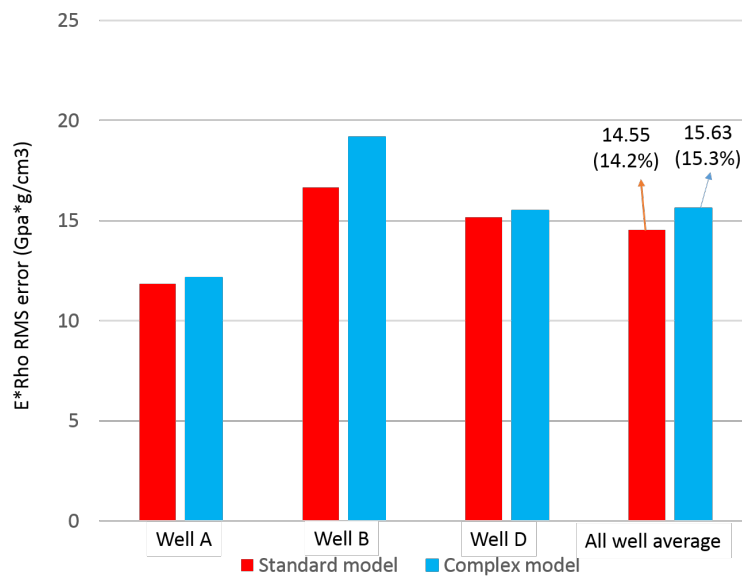


Figure 4.10: RMS errors of blind well tests for  $E\rho$  from the standard and complex low frequency models.

values of the impedances. Therefore, it is vital to QC the well log data and do these blind well tests to assess the effectiveness of the interpolation between wells, in order to reduce risk and handle uncertainty.

The stepwise regression approach is robust, but in this particular situation where there is little knowledge of the reservoir, it is perhaps best to keep the LFM simple, and let the seismic data control the variations in the inversion. A more complex model can be applied when there is more well control and a more developed geological and petrophysical model of the reservoir.

#### 4.4 Effect of VTI anisotropy in AVO inversion

Organic-rich shales normally exhibit strong vertical transverse isotropy (VTI), with the axis of symmetry perpendicular to the bedding-parallel lamination and clay-particle preferred orientation (Vernik and Milovac, 2011). The horizontal P-wave velocity is faster than the vertical P-wave velocity. This has important implications in AVO analysis for these formations. Rüger (2002) showed that the reflection coefficients for P-waves as a function of angle of incidence for a VTI medium can be expressed as:

$$R_P^{VTI}(i) = R_P^{iso}(i) + R_P^{ani}(i) \quad (4.3)$$

where  $i$  is the angle of incidence,  $R_P^{iso}(i)$  is the reflection coefficient in the absence of anisotropy, and  $R_P^{ani}(i)$  is the anisotropic term, given by:

$$R_P^{ani}(i) = \frac{1}{2}(\delta_2 - \delta_1) \sin^2 i + \frac{1}{2}(\epsilon_2 - \epsilon_1) \sin^2 i \tan^2 i \quad (4.4)$$

where  $\delta$  and  $\epsilon$  are the Thomsen parameters (Thomsen, 1986), and the subscripts 1 and 2 denote values for the upper and lower interfaces, respectively.

From the above equations, some important insights can be drawn (Rüger, 2002):

- The parameter  $\delta$  controls the  $\sin^2 i$  term, which influences the reflection coefficient at small angles, while  $\epsilon$  controls the  $\sin^2 i \tan^2 i$  term, which becomes important at larger incident angles.

- If there is no contrast in  $\delta$  and  $\epsilon$  between two interfaces, the reflection coefficient approximates that of purely isotropic media, even if both layers may be VTI.
- Changes in anisotropy have a strong influence on reflection coefficients if the changes in isotropic elastic parameters are comparable to the differences in anisotropic parameters.

Considering the fact that the software used for the pre-stack inversion uses isotropic AVO equations, it is necessary to evaluate the quality of these isotropic approximations when dealing with the anisotropic behavior of the Vaca Muerta shales. To do this, approximate values of Thomsen parameters for the Vaca Muerta interval are estimated using well logs, data from published studies, and certain assumptions. Then, simple AVA modelling is performed to evaluate the impact of anisotropy contrasts given the uncertainty of estimating elastic properties from isotropic inversion.

#### 4.4.1 Estimation of Thomsen parameters

The methodology employed by Willis (2013), who uses the symmetry of the stiffness tensor for VTI media, is followed to calculate the necessary stiffness coefficients. Five independent elastic moduli exist for TI media (Mavko et al., 2009). Three of these stiffness coefficients can be calculated with density and full-waveform dipole sonic tools:

$$C_{33} = \rho_b V_P^2 \quad (4.5)$$

$$C_{44} = \rho_b V_S^2 \quad (4.6)$$

$$C_{66} = \rho_b V_{\text{Stoneley-shear}}^2 \quad (4.7)$$

where  $\rho_b$  is the bulk density,  $V_P$  is the P-wave velocity,  $V_S$  is the S-wave velocity, and  $V_{\text{Stoneley-shear}}^2$  is the horizontal shear velocity. This velocity can be calculated using the following equation:

$$DTSM_{\text{Stoneley-shear}} = \frac{\sqrt{DTST^2 - DT_{mud}^2}}{\sqrt{\frac{\rho_{mud}}{\rho_b}}} \quad (4.8)$$

where  $DTST$  is the Stoneley sonic log,  $\rho_{mud}$  is the drilling mud density, which can be found in the log headers, and  $DT_{mud}$  is the slowness of the drilling mud. This parameter can be estimated by assuming an isotropic match in the underlying Tordillo sandstone using Equation 4.8 (that is, setting the horizontal shear slowness  $DTSM_{Stoneley-shear}$  equal to the vertical shear slowness)(Willis, 2013).

The two remaining independent stiffness coefficients,  $C_{12}$  and  $C_{13}$ , can be estimated using the MANNIE approach developed by Suarez-Rivera and Bratton (2012), shown in the following equations:

$$C_{13} = \zeta C_{33} - 2C_{44} \quad (4.9)$$

$$C_{12} = \xi C_{13} \quad (4.10)$$

where the coefficients  $\zeta$  and  $\xi$  are experimentally determined from cores taken in multiple orientations to the bedding (Willis, 2013).

An equation of symmetry is used for the final coefficient (Mavko et al., 2009):

$$C_{11} = C_{12} + 2C_{66} \quad (4.11)$$

Willis (2013) determined the  $\zeta$  and  $\xi$  coefficients for the Vaca Muerta in an area that is not so far away from the study area for this thesis. The values found were 1.218 and 1.25, respectively. These values were used for estimation of the anisotropy parameters. Thomsen parameters can be calculated as a function of the stiffness coefficients (Thomsen, 1986):

$$\epsilon = \frac{C_{11} - C_{33}}{2C_{33}} \quad (4.12)$$

$$\gamma = \frac{C_{66} - C_{44}}{2C_{44}} \quad (4.13)$$

$$\delta = \frac{1}{2C_{33}^2} [2(C_{13} + C_{44})^2 - (C_{33} - C_{44})(C_{11} + C_{33} - 2C_{44})] \quad (4.14)$$

Using Equations 4.5 to 4.14, the Thomsen parameters were computed for the Vaca Muerta interval using wells C and D, which were the only ones with reliable Stoneley well logs. (Figure 4.11 shows the logs for  $\delta$  and  $\epsilon$ . Aside from short wavelength variations in the Upper

Vaca Muerta, the values for both  $\delta$  and  $\epsilon$  remain fairly constant throughout the whole interval, at mean values of approximately 0.1 and 0.2, respectively.

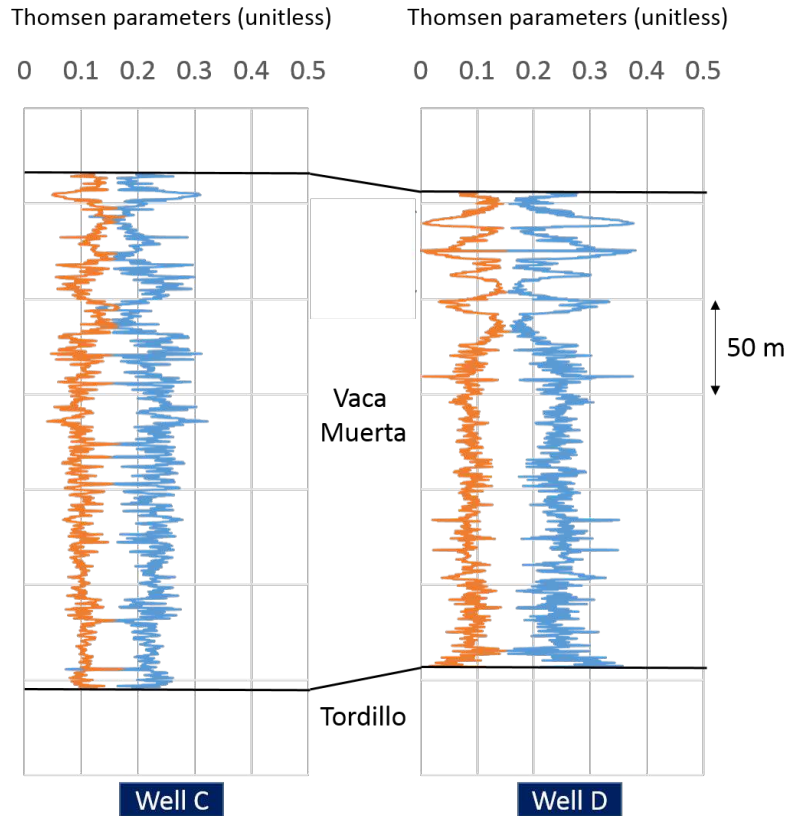


Figure 4.11: Logs of Thomsen parameters for wells C and D. Orange: delta. Blue: epsilon.

Looking at these results, and based on Equations 4.3 and 4.4, it can be concluded that, since the anisotropic parameters do not have big contrasts within the Vaca Muerta, the isotropic AVA equations used for pre-stack inversion, are a good approximation to the VTI behaviour of the Vaca Muerta, giving further confidence in the inversion results. The exception for this case is the Lower Vaca Muerta, which overlies the Tordillo Formation. Being a massive sandstone, the Tordillo is not expected to exhibit any strong anisotropy. While this may be a gross assumption, we can say that the anisotropic parameters for this formation are close to zero. There is a strong anisotropy contrast between the Lower Vaca Muerta and the Tordillo, which will be the issue to address in the AVA reflectivity model explained in

next section.

#### 4.4.2 Reflectivity modelling for the Lower Vaca Muerta-Tordillo interface

Equations 4.3 and 4.4 are used, where the isotropic reflection coefficients are calculated using the Aki-Richards approximation presented in Equation 3.1. Table 4.1 shows the reservoir properties of the Lower Vaca Muerta and the Tordillo used for this simple reflectivity modelling:

Table 4.1: Average properties of the Lower Vaca Muerta and Tordillo obtained from the well logs.

Property	Lower Vaca Muerta	Tordillo
$\rho$ (g/cc)	2.36	2.61
$V_P$ (m/s)	3170	4700
$V_S$ (m/s)	1870	2710
$\epsilon$	0.2	0
$\delta$	0.1	0

Isotropic reflection coefficients are used in the inversion to determine elastic parameters that provide the best match to the input AVA response (MacFarlane, 2014). Figure 4.12 compares the isotropic and anisotropic reflection coefficients for the properties described above. The isotropic approximation (blue curve) does not yield a good match with the anisotropic AVA character expected for this interface (orange curve). By scaling the S-wave velocity of the Lower Vaca Muerta in the isotropic equation by a factor of 0.9, however, the match with the anisotropic curve becomes acceptable for the angle ranges up to 36 degrees (black curve).

This simple model suggests that the inversion will tend to underestimate the S-impedance values for the Lower Vaca Muerta (by a factor of 10% or more), which might explain the mismatch seen in Figure 3.35 in wells B and D. This means that the  $V_p/V_s$  ratio, and therefore the Poisson's ratio extracted from the inversion is expected to be higher than it actually is in this interval.

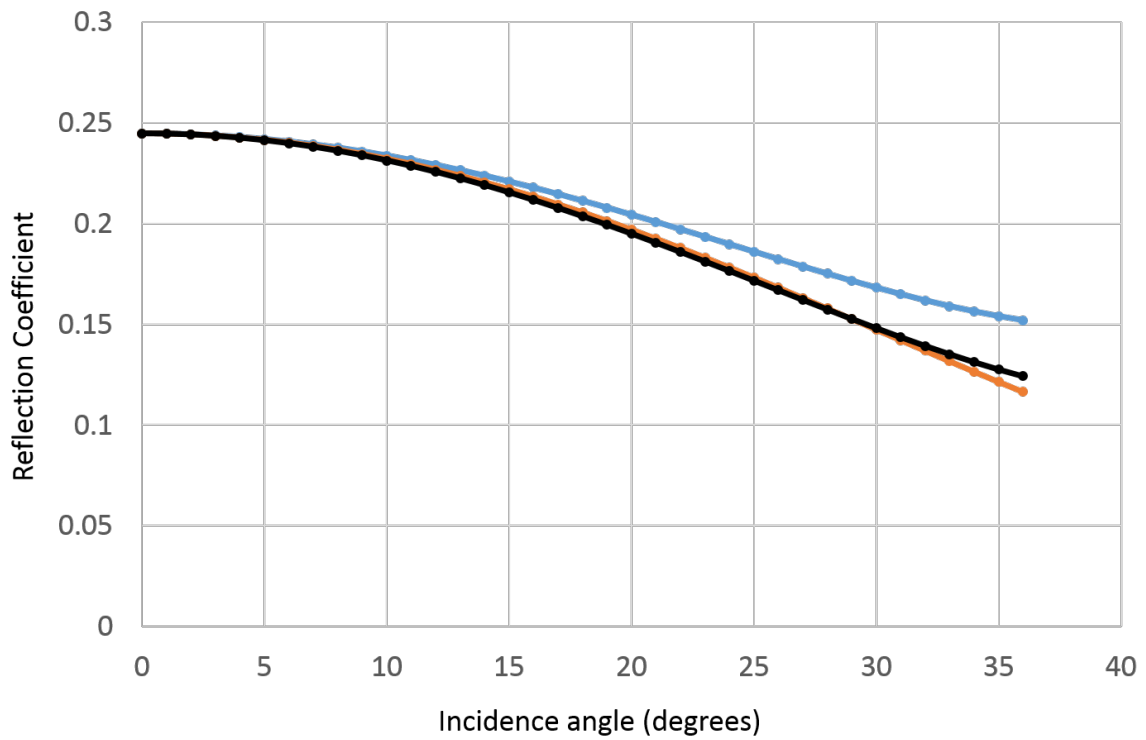


Figure 4.12: Comparison between reflection coefficient curves for the Lower Vaca Muerta-Tordillo interface model. Blue: isotropic. Orange: anisotropic. Black: isotropic with  $0.9 \cdot V_s$ .

Using isotropic equations to approximate an anisotropic AVA response will generate additional uncertainty in the estimation of elastic properties in the Lower Vaca Muerta.

## CHAPTER 5

### INTERPRETATION AND INTEGRATION OF INVERSION RESULTS

Understanding the relationships between the elastic parameters derived from pre-stack inversion and some of the key properties that control productivity in shale plays, such as mineral composition, TOC, and pore pressure, can be a fundamental step in the reservoir characterization of the Vaca Muerta. This approach enhances the value of seismic data beyond conventional structural interpretation and attribute analysis.

This chapter focuses on the petrophysical analysis and rock physics modelling that provide the crucial link between seismic inversion and the reservoir parameters needed to identify potential sweet spots and to guide future well placement. The mechanical stratigraphy work performed by Kyla Bishop is integrated into the inversion results in a probabilistic framework. It provides the possibility to derive rock physics relationships in terms of rock classes, while helping to gain insights into the compositional influence on the geomechanical behavior of the reservoir, as well as the effective stress linkage to velocities for the Vaca Muerta. The validation data from production logging are also integrated into the analysis.

#### **5.1 Relationships between elastic parameters, mineralogy and organic content**

The three main minerals that compose the inorganic framework of the Vaca Muerta rocks in the study area are calcite, quartz, and illite. The XRD data produce a direct measurement for the mineral volumetrics, but it is sparsely sampled from the cuttings. Therefore, wireline logs calibrated with the XRD measurements were used to compute these mineral fractions at log resolution, and consequently link them with the elastic properties at the well locations.

Wells B, C, and D have Schlumberger's Elemental Capture Spectroscopy (ECS) wireline data for the Vaca Muerta, which after specialized processing gives weight lithology fractions for quartz-feldspar, carbonate (calcite), and clay (illite). These were transformed from weight fractions to volume fractions. An excellent correlation was found between these volumes

derived from the ECS and the XRD data from Wells B and C (Figure 5.1(a)). Well D does not have XRD data available to calibrate, so the volume fractions derived from the ECS log are taken as a good representation of the mineralogy in this well.

Well A does not have an ECS log available, but it does have XRD data from cuttings. Therefore, for this well the following petrophysical relationships are used, calibrating the parameters to find a best fit with the XRD data in the interval of interest:

- Volume of clay is defined from Steiber's method, using the following equations (Steiber, 1973)

$$I_{GR} = \frac{GR_{log} - GR_{min}}{GR_{max} - GR_{min}} \quad (5.1)$$

$$V_{clay} = \frac{I_{GR}}{3 - 2I_{GR}} \quad (5.2)$$

where  $GR_{log}$  is the Gamma Ray value from the log (in API units),  $GR_{min}$  and  $GR_{max}$  are the minimum and maximum values, respectively, of GR in the interval of interest. It is important to note that the Gamma Ray log used has been corrected for uranium, which is considered to be influenced more by the organic content than by the clay content.

- Volume of quartz is defined by an empirical correlation developed by Wintershall, given by:

$$V_{quartz} = \left[ \frac{GR_{log} + 102}{2.63} \right] * x \quad (5.3)$$

where  $x$  is a calibration parameter used to fit the XRD data. The GR log used is also the one corrected for uranium.

- Volume of carbonate is given by:

$$V_{carbonate} = 1 - [V_{quartz} + V_{clay}] \quad (5.4)$$

Figure 5.1(b) shows the logs of mineral volumes for Well A, which show a good correlation with the XRD data for most of the target interval.

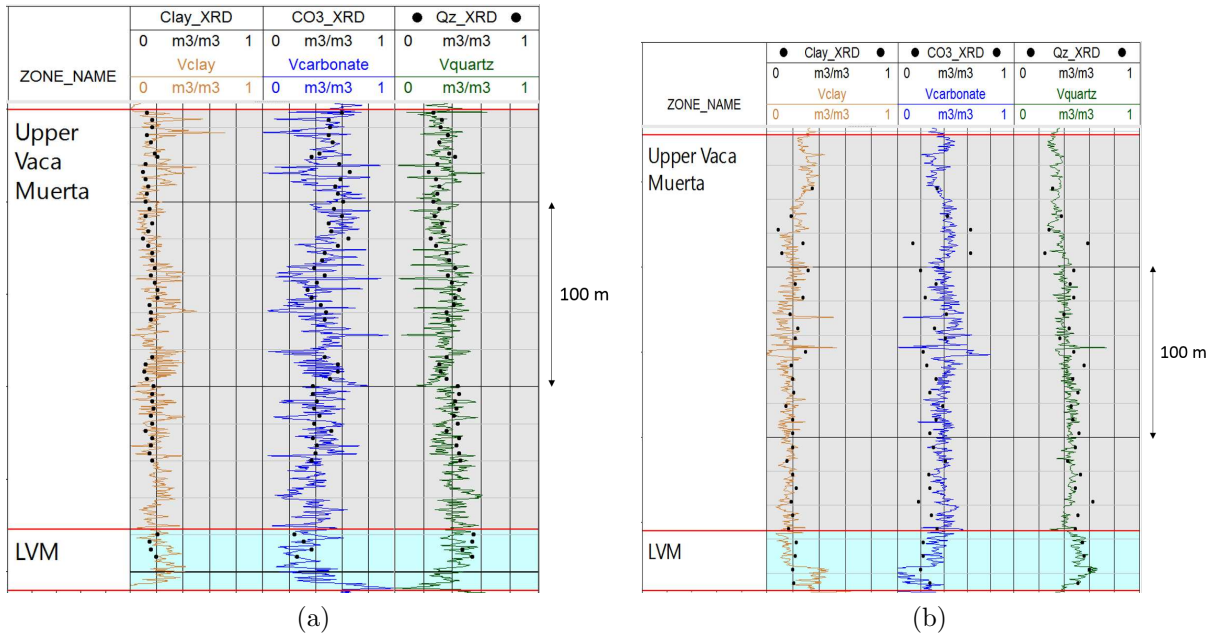


Figure 5.1: Logs of clay, carbonate and quartz mineral volumes, with calibration data from XRD (black dots). (a) Well B (from ECS logs). (b) Well A (from petrophysical relationships).

For the calculation of the TOC within the Vaca Muerta, Schmoker's empirical formula was used (Schmoker and Hester, 1983). It is given by:

$$TOC = \left[ \frac{A}{\rho_B} \right] - B \quad (5.5)$$

where the TOC is computed in weight %,  $\rho_B$  is the bulk density from the logs, and  $A$  and  $B$  are fitting parameters.

Wells B and C have Rock-Eval data from cuttings, allowing for calibration of the TOC values for these wells. No Rock-Eval data are available for wells A and D, so the same fitting parameters found for wells B and C are used for these wells. Figure 5.2 shows the TOC logs. Note the excellent match with the calibration data in the wells where these data are present.

The way to find relationships between elastic parameters and these petrophysical properties is by cross-plotting data from the well logs. Figure 5.3(a) shows a crossplot in a typical domain to evaluate pre-stack inversion results:  $V_p/V_s$  vs P-impedance. The color code is

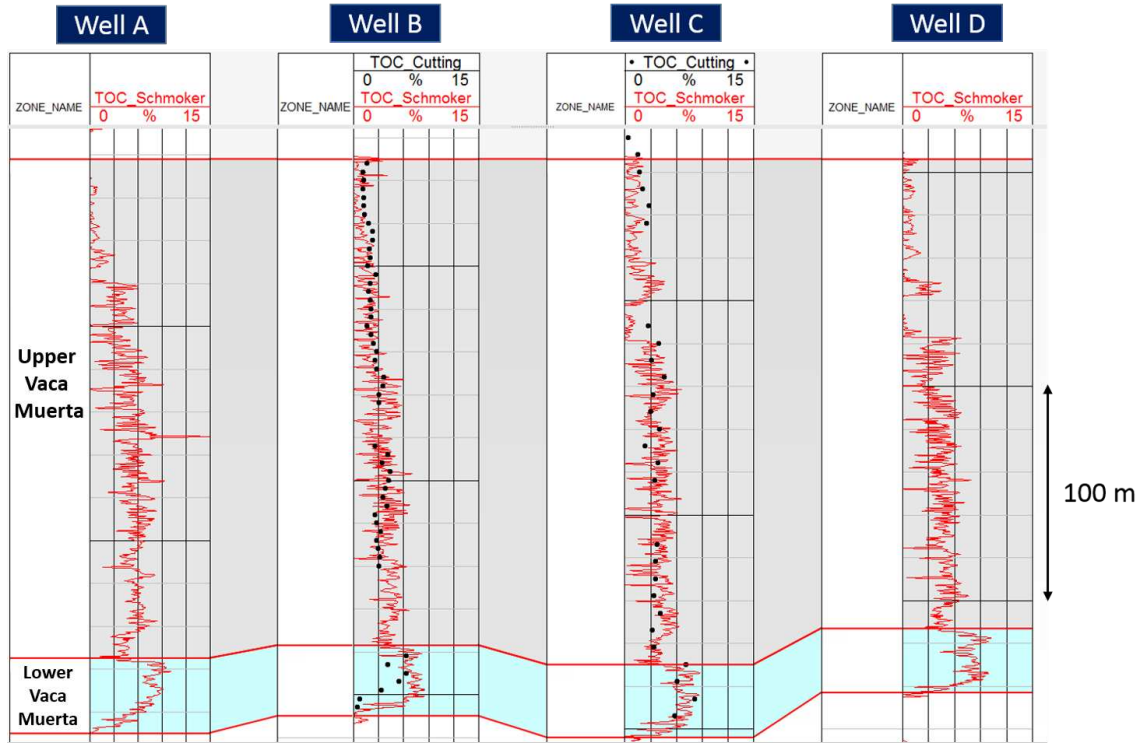


Figure 5.2: TOC logs with rock-eval calibration data (black dots).

volume of carbonate. It can be clearly seen that the acoustic impedance increases with increasing carbonate content.  $V_p/V_s$  ratio does not show a clear sensitivity to the change in  $V_{carbonate}$ .

The cross-plot in Figure 5.3(b) also features  $V_p/V_s$  versus P-impedance, but now color coded by volume of quartz. Contrary to the case for carbonate, the increase in acoustic impedance is related to a *decrease* in quartz content. Again, the  $V_p/V_s$  attribute does not respond clearly to variations in  $V_{quartz}$ . Clay volume does not show any clear correlation to either P-impedance or  $V_p/V_s$  (Figure 5.3(c)).

An expected inverse relationship between acoustic impedance and TOC is captured in Figure 5.3(d). Kerogen, being a much less stiff material than the inorganic minerals has slower seismic wave velocities. The increase in TOC towards the base of the Vaca Muerta is correlated well with the decrease in P-impedance, but no relationship is seen for the  $V_p/V_s$  ratio.

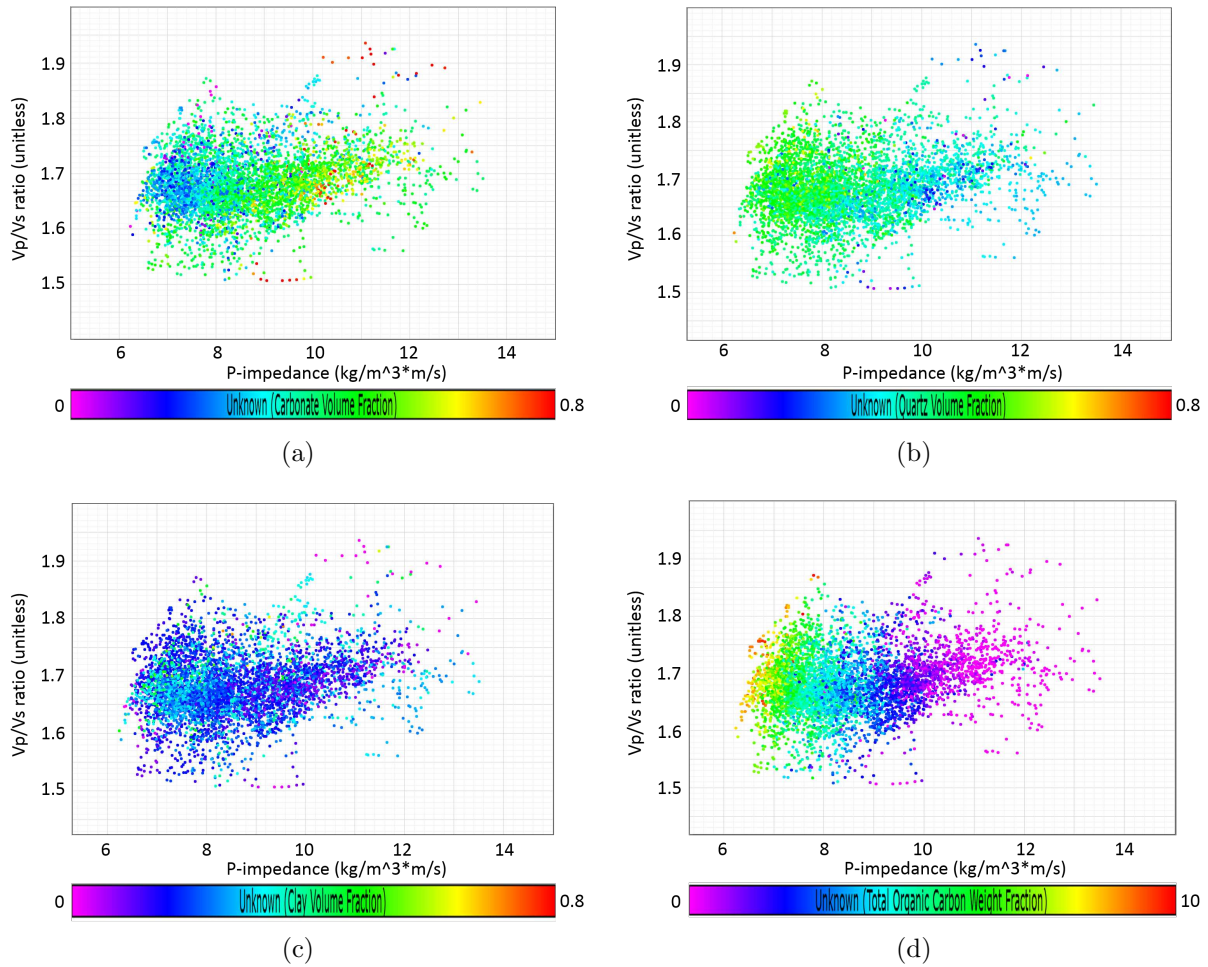


Figure 5.3: Cross-plots of  $V_p/V_s$  (y-axis) vs P-impedance (x-axis), color coded by (a) carbonate volume, (b) quartz volume, (c) clay volume, and (d) TOC.

Figure 5.4 shows the cross-plots between the P-impedance and the rock properties that show sensitivity to this elastic parameter. The direct relationship with carbonate content and the inverse relationship with quartz content and TOC can be clearly detected, and demonstrates that P-impedance is a robust attribute that can be used to map the distribution of mineral fractions and organic content in the reservoir from seismic inversion volumes. The clay content, although not sensitive directly from acoustic impedance, can be easily calculated using Equation 5.4, if there is knowledge of  $V_{carbonate}$  and  $V_{quartz}$ .

An important observation can be made from the cross-plots in Figure 5.4. To transform P-impedance into any of these properties by using a simple regression technique to fit the

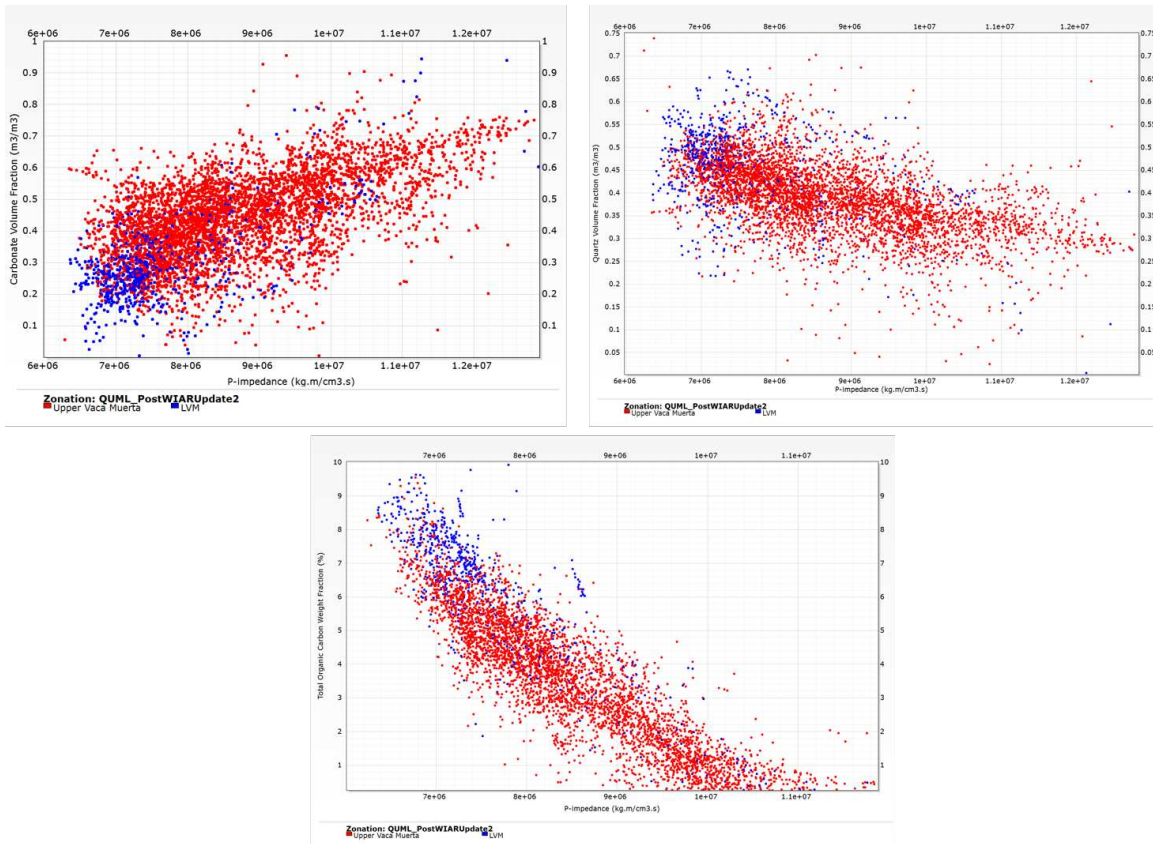


Figure 5.4: Top left: P-impedance vs carbonate volume. Top right: P-impedance vs quartz volume. Bottom: P-impedance vs TOC. The colour code is red for the Upper Vaca Muerta and blue for the Lower Vaca Muerta.

whole data would not be the best way to approach the problem. There seems to be more than one single slope, implying that the relationship between these parameters is most likely facies-dependent. Conventional petrophysics and seismic analysis techniques lack the necessary focus on the heterogeneous nature of shale plays, and often define models and predictions that, while adequately representing the mean behavior of the system, may have substantial errors at the local level (Suarez-Rivera et al., 2013).

An illustration of this problem can be seen on Figure 5.5. Cluster analysis provides a useful tool to evaluate the variability of the Vaca Muerta by separating it into *rock classes* from which more focused property predictions can be made.

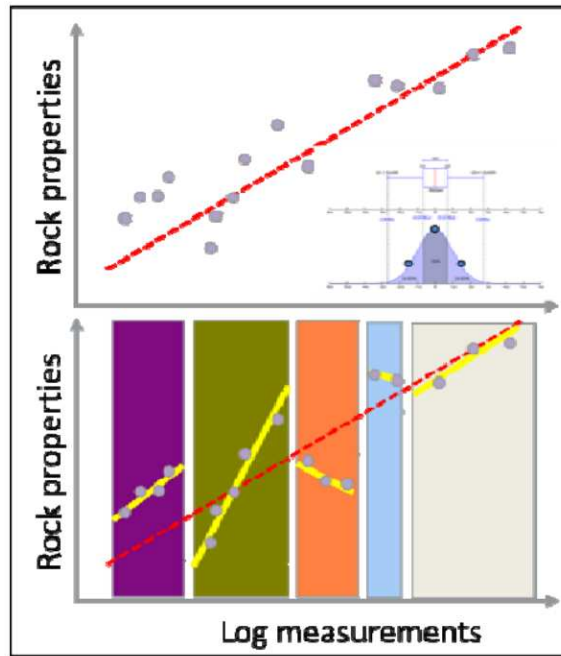


Figure 5.5: Graphical representation of the advantage of using rock class classification for property predictions vs global correlations (Suarez-Rivera et al., 2013).

## 5.2 Integration with mechanical stratigraphy

Fellow RCP researcher Kyla Bishop performed comprehensive work on cluster analysis for the Vaca Muerta, using all wells in the study area. She used as input the log suites considered to best capture the *mechanical* variability of the reservoir: bulk density, Gamma Ray, dynamic Young's Modulus, and  $V_p/V_s$ . Bishop chose Well B, which is considered to contain the most complete and best quality log dataset, as the master well for the cluster analysis. Based on many QC plots and sensitivity analysis, she found that using nine clusters gives a good representation of the heterogeneity of the reservoir. After the master classification was established for Well B, the rest of the wells were tagged.

Figure 5.6 shows the cluster analysis results. Three main zones can be identified, with fairly consistent patterns across the wells. The lower Vaca Muerta appears to be quite homogeneous, with a predominance of clusters 7, 8, and 9. The upper part of the Vaca Muerta is less homogeneous but still some relatively thick layers can be identified, mostly

of clusters 1 and 3. The middle part of the Vaca Muerta shows the greatest heterogeneity. Small-scale variability of clusters 4, 5, 7 and 8 is detected for all four wells.

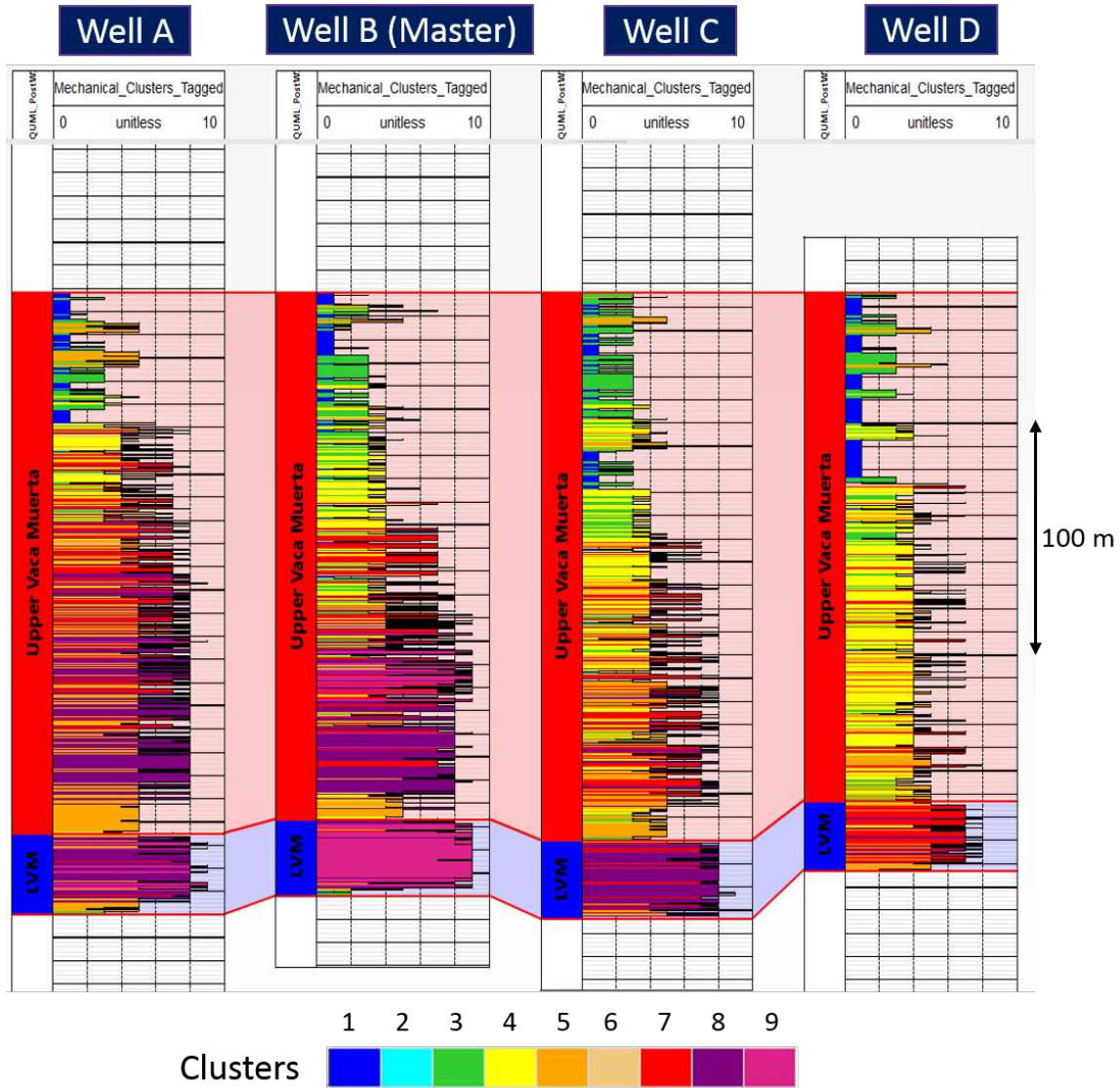


Figure 5.6: Cluster analysis results for the Vaca Muerta (Bishop, 2015).

### 5.2.1 Rock class properties

To establish the link between mechanical stratigraphy and the inversion results, the rock classes defined by Bishop’s cluster analysis need to be analyzed in a quantitative manner in terms in geomechanical properties, mineralogical composition, and organic content. The

subsequent analysis includes only the most representative six of the nine clusters. Cluster 2, 6 and 9 do not have a large enough sampling size, especially when these rock classes will be upscaled to seismic resolution.

Figure 5.7 shows histograms of the distributions of  $E\rho$  for each cluster. The values consistently decrease with increasing cluster number. This means that clusters 1 and 3 are the stiffest rocks. This is not surprising as these are mostly located in the upper Vaca Muerta, while clusters 7 and 8, which are the least stiff, generally are found in the middle to lower Vaca Muerta. The distributions of Poisson's ratio do not show this consistency with cluster number. The peak values for all clusters fall between 0.20 and 0.25, suggesting small variability in this parameter, although clusters 4 and 7 exhibit slightly lower values (Figure 5.8).

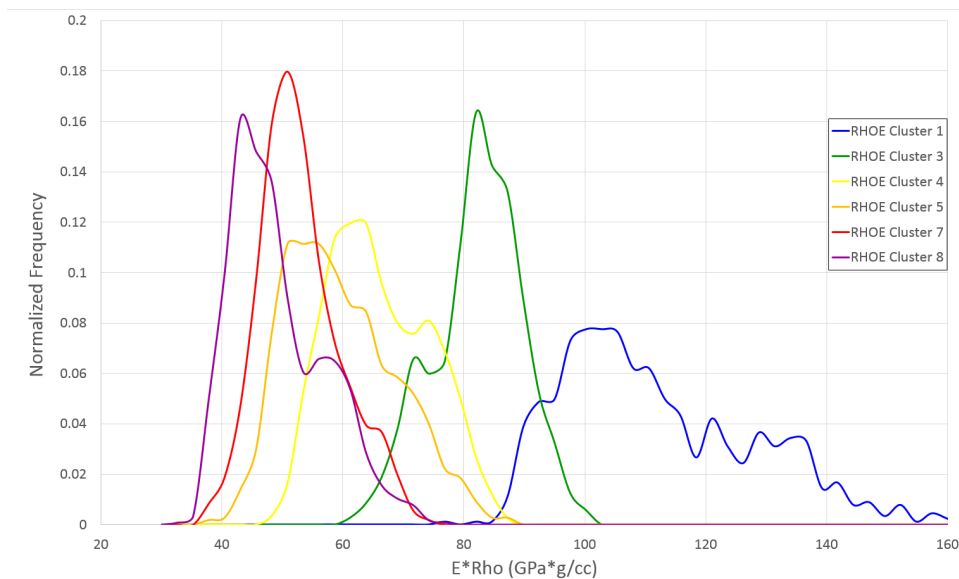


Figure 5.7: Distributions of  $E\rho$  by rock class.

In terms of mineral composition, there is a definite trend of increasing quartz content with increasing cluster number (Figure 5.9). The opposite occurs for carbonate content, although the trend is not nearly as consistent as that for quartz, yielding more overlap and higher standard deviations in the distributions (Figure 5.10). These histograms confirm that the quartz-to-carbonate ratio decreases towards the base of the Vaca Muerta, and that the

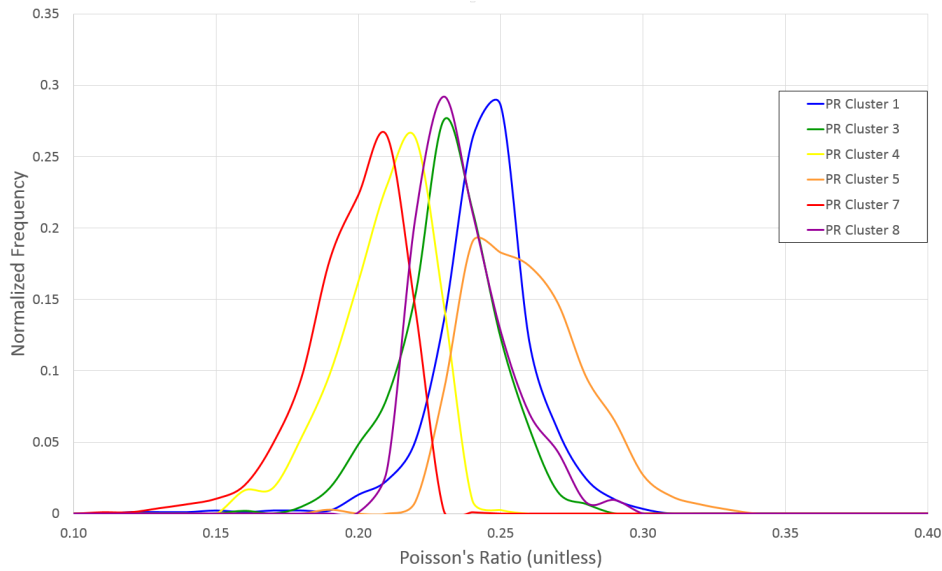


Figure 5.8: Distributions of Poisson's ratio by rock class.

rock classes are capturing this composition variability.

The clay volume yields very similar distributions (Figure 5.11). With the exception of clusters 1 and 8 that have slightly smaller values, all clusters peaks at around 20% clay volume, meaning that the Vaca Muerta has relatively low clay content throughout all of the interval. This suggests favourable conditions for hydraulic fracturing. Aside from possible drilling problems caused by clay swelling, rocks with high clay content are more ductile and therefore less prone to generate and sustain fracture networks.

TOC also shows a consistent pattern of increasing organic richness with increasing cluster number (Figure 5.12). Again, this an expected results since TOC increases downwards in the Vaca Muerta. But it is interesting to confirm that the mechanical rock classes are sensitive to this composition effect. Clusters 4, 5, 7, and 8 have TOC values mostly higher than 2-3 wt %, making them rocks with excellent hydrocarbon generation potential.

### 5.2.2 Rock class probability from seismic inversion volumes

A deterministic interpretation does not take into account the uncertainties in the data such as property overlap of lithology, resolution, or seismic noise. It is only a likely interpre-

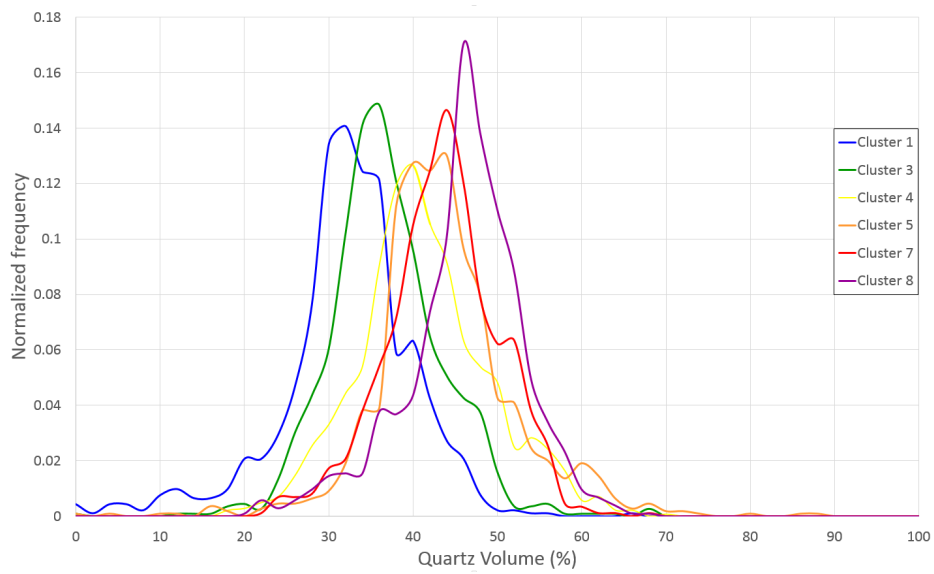


Figure 5.9: Distributions of quartz volume by rock class.

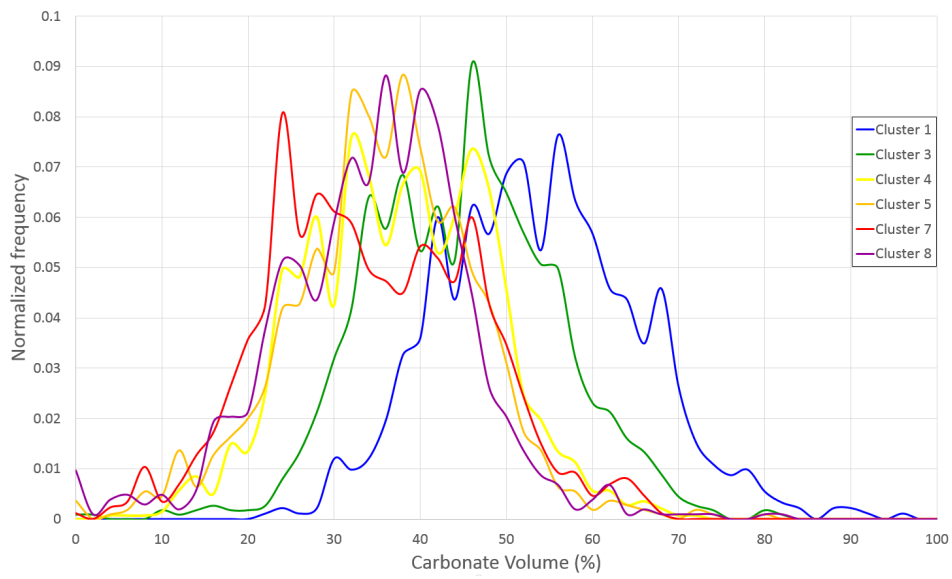


Figure 5.10: Distributions of carbonate volume by rock class.

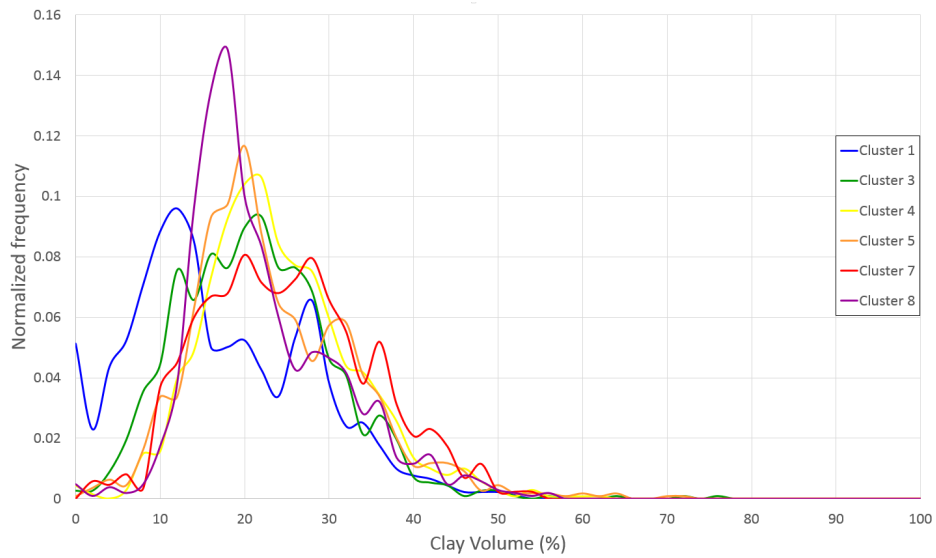


Figure 5.11: Distributions of clay volume by rock class.

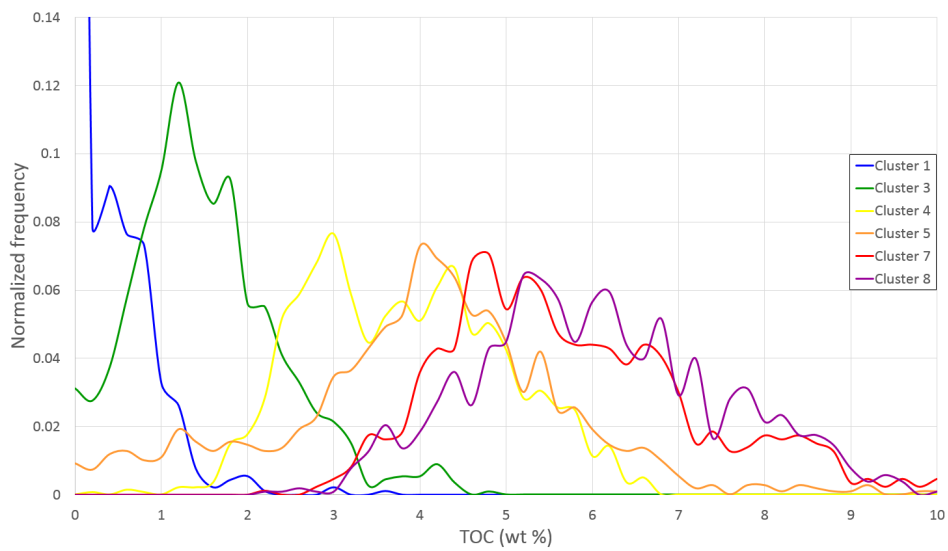


Figure 5.12: Distributions of TOC by rock class.

tation, at best. Typical workflows such as adjusting polygons in cross-plots arbitrarily, do not give a quantitative estimate of uncertainty. The Facies and Fluid Probability (FFP) module in Jason<sup>TM</sup> software uses Bayesian theory to generate probability volumes from deterministic inversion results and lithology logs, indicating the likelihood that a certain lithology is present at a data point in the seismic grid.

The following steps were applied for FFP:

1. Create lithology logs, using the rock classes derived from Bishop's mechanical cluster analysis.
2. Determine a combination of properties derived from seismic inversion that creates a good enough discrimination of rock classes. After some experimentation, P-impedance and  $V_p/V_s$  were found to be a suitable pair.
3. Calculate the prior probability for each rock class using the known geological information from the wells. This is an important input according to Bayesian theory (Table 5.1):

Table 5.1: Prior probabilities for each rock class.

Rock class	Probability
1	0.09
3	0.16
4	0.19
5	0.18
7	0.15
8	0.23

4. Fit 2D Probability Density Function Functions (PDF) to every rock class. Figure 5.13 shows the calculated PDF's for each rock class. Although there is still some overlap, the rock classes are fairly well separated, and the PDF's honor this discrimination.
5. Apply the weighted lithology PDF's to the inversion volumes.

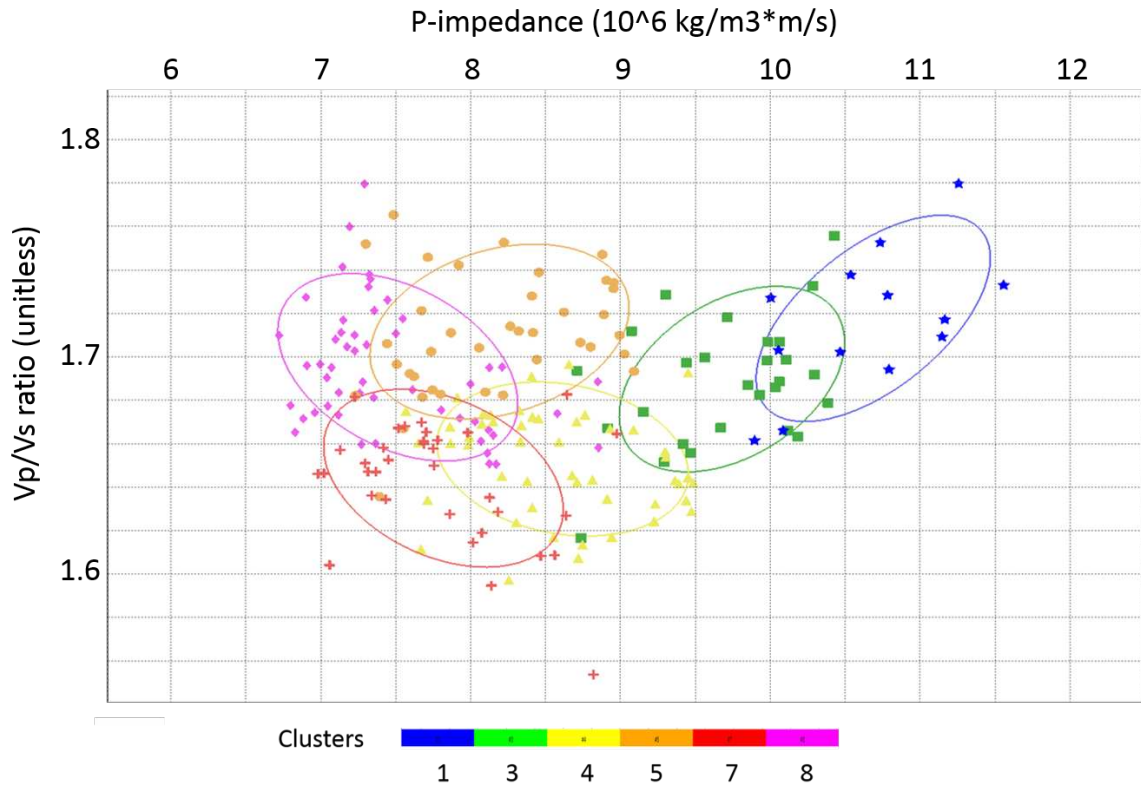


Figure 5.13: Cross-plot of P-impedance vs  $V_p/V_s$  at seismic resolution, color coded by rock class, and associated PDF's for each rock class.

The software outputs probability volumes for each rock classes, as well a most probable rock class volume. Figure 5.14 shows a section of most probable rock class. A good match exists with the rock classes from cluster analysis at Well A, considering of course the significant difference in resolution (well logs are sampled at less than 20 cm, while a seismic wavelength can be up to tens of meters). The vertical and lateral variability of the rock classes is seen very clearly.

FFP provides a robust workflow to handle uncertainty in interpretation. The most probable rock volume can be used to help guide placement of future wells, once a sound interpretation is complete and the best rock classes in terms of reservoir quality and potential for efficient hydraulic stimulation are identified. It can even be a useful tool for geosteering purposes.

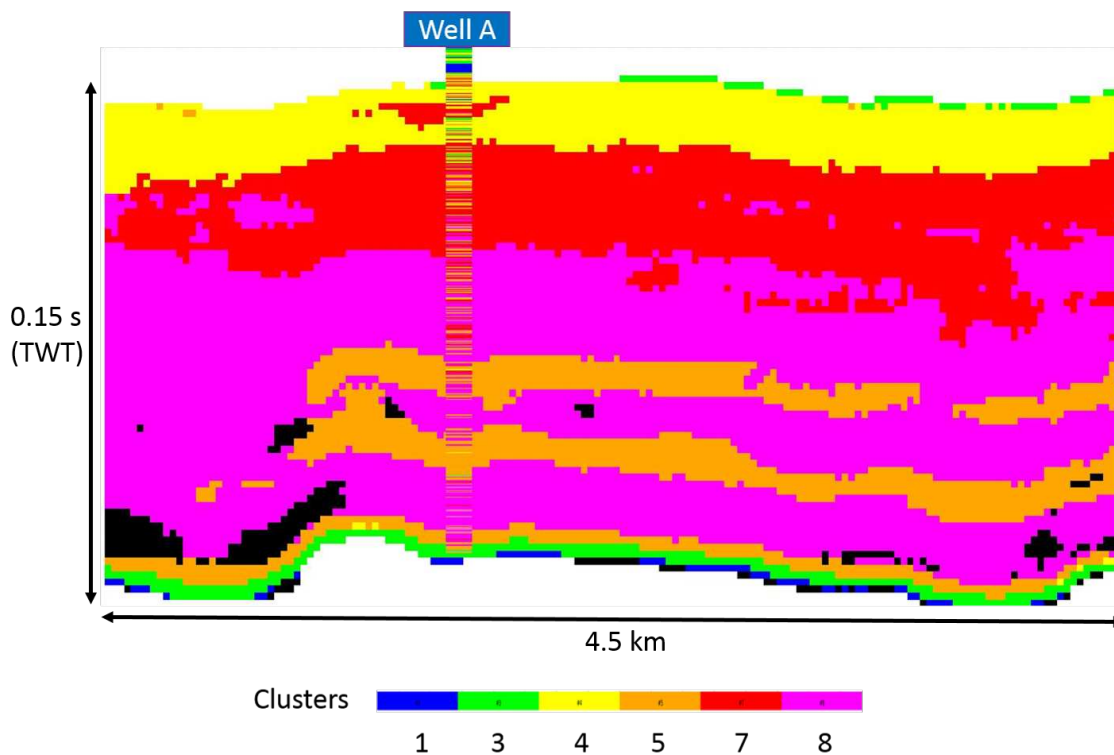


Figure 5.14: Inline section showing most probable rock class volume and comparison with Well A lithology log. Areas in black are unclassified.

### 5.3 Link of velocities with effective stress/pore pressure

Rock physics forward modelling can be used to estimate theoretical values for elastic properties from combinations of porosity, fluid saturations, and mineral volumes, which can then be compared with the actual measured values of  $V_p$ ,  $V_s$ , and density.

The blocky Xu-Payne module in Ikon Science's RokDoc™ software was used, which is based on the methodology developed by Xu and Payne (2009). In essence, the Xu-Payne rocks physics model starts by mixing the various matrix components (inorganic minerals and kerogen in this case) using Reuss-Voigt-Hill average. Then, various pores (interparticle as well as wet clay water-bound pores) are included in the system using differential effective medium theory. Finally, the pore fluids are added using Gassmann's theory.

For each rock class, the mean mineral (calcite, quartz, and illite) and kerogen (TOC) volumes derived from petrophysical analysis were calculated. The log-derived porosities

calculated by Wintershall correlate well with core porosity measurements, so these values are used for the estimation of the mean porosity for each rock class. In terms of fluids, the model assumes full water saturation as a base case. Replacing brine with oil has a very small effect on the velocities in low-porosity rocks such as the ones found in the Vaca Muerta.

Table 5.2 shows the results of comparing the modelled values with the measured values of elastic properties. The densities show an excellent agreement between model and data. For every rock class, the measured values of  $V_p$  and  $V_s$ , however, are significantly lower than the values obtained from the Xu-Payne model. Another interesting observation is that for clusters 4 and 7, the  $V_p/V_s$  ratio of the data is noticeably lower than that of the model.

Table 5.2: Comparison of measured and modelled elastic parameters for each rock class. Density is in g/cc and velocities are in m/s.

Rock class	$\rho_{data}$	$\rho_{model}$	$V_{p_{data}}$	$V_{p_{model}}$	$V_{s_{data}}$	$V_{s_{model}}$	$V_p/V_{s_{data}}$	$V_p/V_{s_{model}}$
1	2.63	2.61	4340	5315	2539	3118	1.71	1.7
3	2.55	2.55	3782	4821	2247	2843	1.68	1.7
4	2.47	2.45	3432	4287	2091	2509	1.64	1.71
5	2.46	2.45	3410	4290	1956	2521	1.74	1.7
7	2.39	2.39	3148	4025	1940	2335	1.62	1.72
8	2.37	2.38	3140	4049	1855	2358	1.69	1.72

The large deviations of the measured velocities with respect to the modelled velocities, cannot be explained by lithology, porosity, and/or fluid content. These differences should be attributed to *effective stress*. If the effective stress is reduced, the velocities will deviate from the Normal Compaction Trend (NCT), meaning velocity decreasing with depth (Bowers, 1995). According to Terzaghi’s equation, a reduction in effective stress means an increase in pore pressure.

Pore pressure prediction in unconventional reservoirs is a challenging endeavor, worthy of a whole thesis (Herzog, 2014). For the purposes of this work, an extremely simplified pore pressure calculation was performed, based on the methodology proposed by Herzog (2014). The objective is to confirm the overpressured nature of the Vaca Muerta, and explore possible

relationships with the rock classes. The summarized workflow is as follows:

1. Define overburden stress by integration of the density logs. The extrapolation of the density to surface was done based on offset wells.
2. Select area of normal compaction, defined as the normally pressured interval. This was defined as the overburden above the Quintuco (Herzog, 2014). Obtain best fit parameters for the NCT.
3. Perform lithology and porosity substitution on the compressional velocity in the Quintuco and Vaca Muerta using a simple petrophysical model. That way only the effects of stress on the velocities are left (Herzog, 2014).
4. Calculate pore pressure using these velocity curves corrected for lithology and porosity.

As interpreted in Figure 5.15, the onset of overpressure for all wells is located in the upper to middle Quintuco. Entering the Tordillo, the pressure appears to sharply return to normal.

Pore pressure calculation with the Bowers equation yielded values that appeared to be unrealistically high (almost consistently above 1 psi/ft). On the other hand, the Eaton equation (Eaton, 1975) gave values much closer to what is expected and has been found in the Vaca Muerta (mostly between 0.7 and 0.95 psi/ft). The results are shown in Figure 5.16. These results confirm that the Vaca Muerta is highly overpressured through the entire interval, and this overpressure is causing the large reduction in the velocities.

Examining the pore pressure distributions per rock classes will help determine if there is any correlation between overpressure and the lower  $V_p/V_s$  ratio seen in clusters 4 and 7. Figure 5.17 shows these distributions. Clusters 1 and 3 have lower pore pressure than the others. A clear link between overpressure and  $V_p/V_s$  cannot be established, as cluster 7 is the most overpressured along with cluster 5, which has a higher  $V_p/V_s$  ratio, whereas cluster 4 appears to be less overpressured.

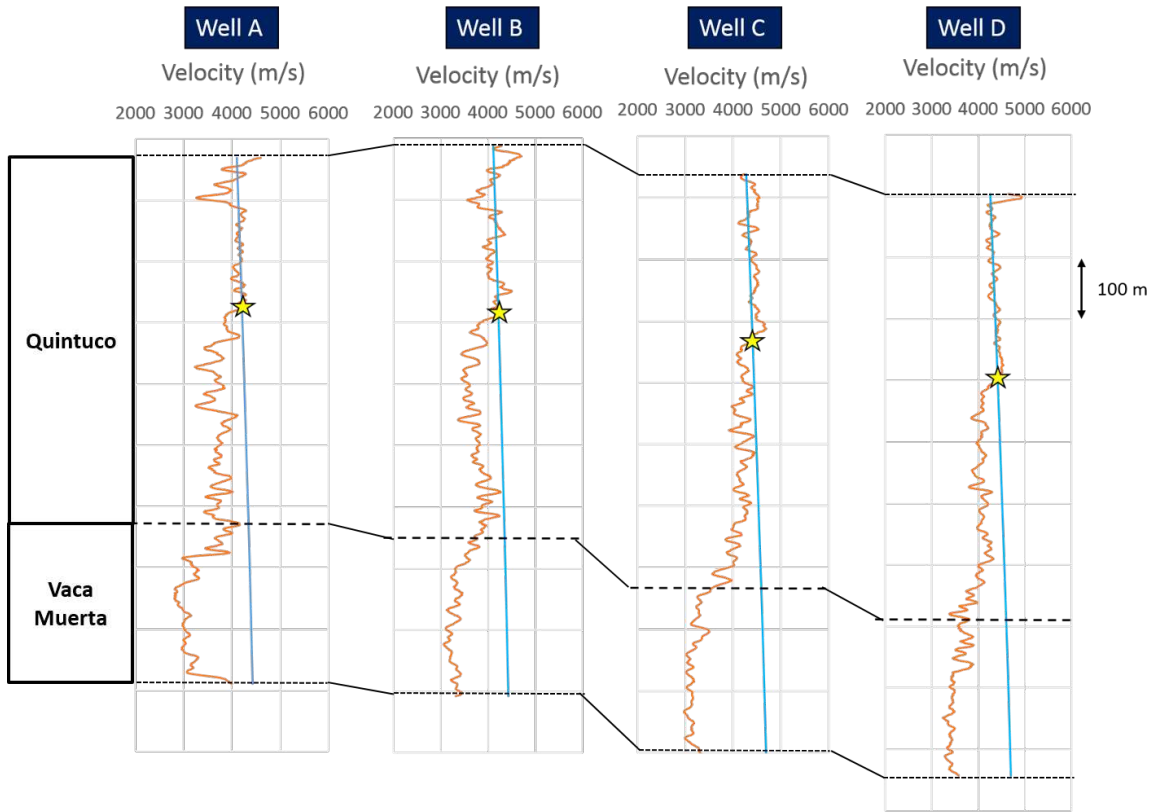


Figure 5.15: NCT (blue curve) with lithology and porosity corrected P-wave velocity (orange curve). The stars point to the interpreted onset of overpressure. The dashed black line represent the Quintuco-Vaca Muerta boundary.

Gas saturation is likely to be the biggest control on  $V_p/V_s$  variation in this case. Using the Xu-Payne model, and doing fluid substitution with a small amount of gas (10%) the modelled  $V_p/V_s$  ratio decreases, matching the measured  $V_p/V_s$  for clusters 4 and 7 (Table 5.3).

#### 5.4 Interpretation of good quality rock classes

Based on the analysis presented in the previous sections, clusters 5 and 7 exhibit a good set of characteristics to be considered for potential drilling targets. These favorable properties are:

- Low clay content (23% average), and hence a high proportion of brittle minerals (calcite and quartz).

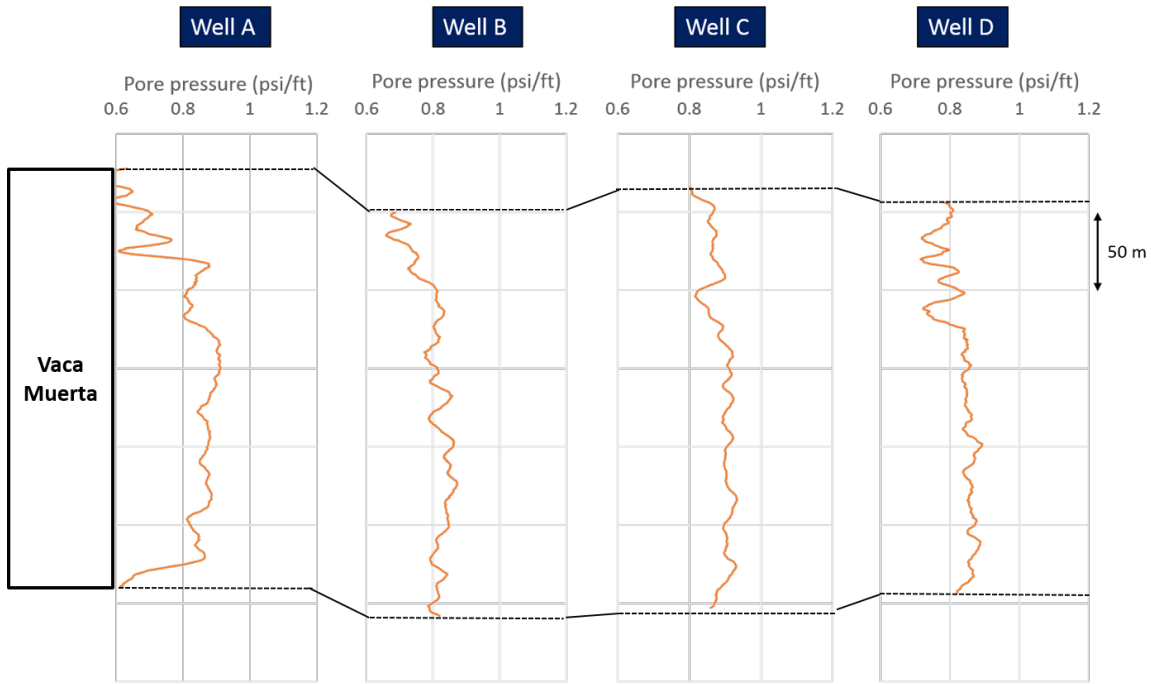


Figure 5.16: Calculated Eaton pore pressure profiles for the Vaca Muerta interval.

Table 5.3:  $V_p/V_s$  ratio of data compared with modelled and fluid substituted  $V_p/V_s$  for clusters 4 and 7.

Rock class	$V_p/V_s$ (data)	$V_p/V_s$ (model, $S_w=1$ )	$V_p/V_s$ (model, $S_w=0.9$ , $S_g=0.1$ )
4	1.64	1.73	1.64
7	1.62	1.72	1.63

- High TOC (6 wt.% average).
- High overpressure (0.86 psi/ft average).
- Low Poisson's ratio (0.19 average). In a passive basin and under the isotropic stress assumption, the minimum horizontal stress is estimated with the following equation (Close et al., 2012):

$$\sigma_{xx} = \frac{\nu}{1 - \nu}(\sigma_{zz} - P) + P \quad (5.6)$$

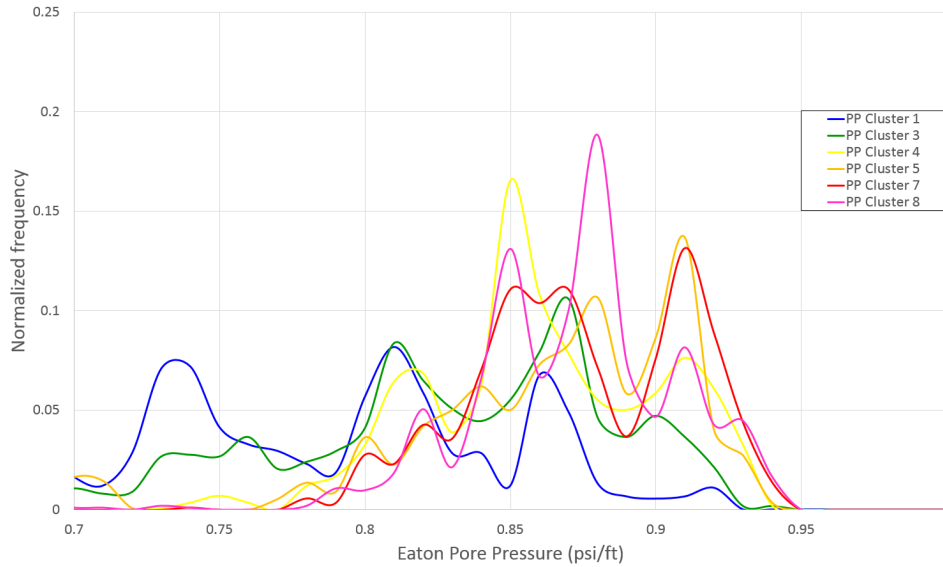


Figure 5.17: Distributions of Eaton pore pressure by rock class.

where  $\sigma_{zz}$  is the vertical overburden stress,  $P$  is the pore pressure, and  $\nu$  is Poisson’s ratio.  $\frac{\nu}{1-\nu}$  is defined by Goodway et al. (2010) as the closure stress scalar (CSS). Low Poisson’s ratio, and therefore low CSS values, means that the minimum pressure required to open and sustain pre-existing fractures or planes of weakness is lower, which is favorable from a hydraulic fracturing and completions standpoint (Close et al., 2012).

- Good correlation with areas of high production from the Production Logging Tool (PLT) in well A (Figure 5.18).

The uncertainty analysis derived from FFP can be used as a guide to propose landing zones for horizontal wells. As mentioned in the introduction, two vertical wells were drilled in the study area. These wells will be used as drilling pads for the horizontals. Figure 5.19 shows proposed well trajectories using the first drilled vertical well (Well E) as pad. Likewise, Figure 5.20 shows proposed plans for the horizontals using the second vertical well (Well F) as pad. Both cases assume that:

- The well trajectories follow the highest probability of occurrence of either cluster 5 or 7.

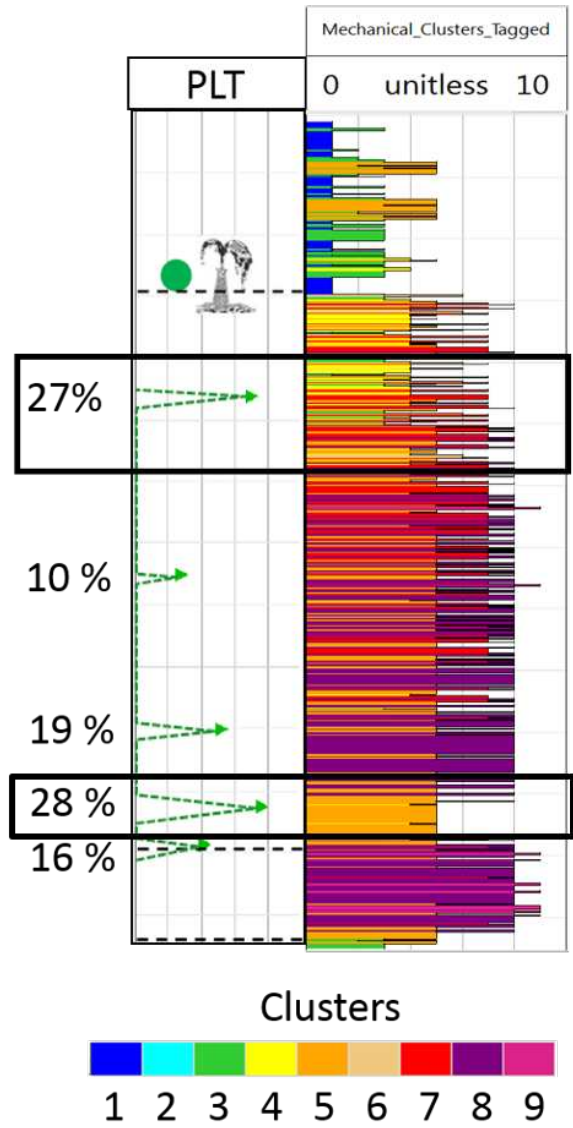


Figure 5.18: PLT data with oil production percentages per stage (left track), and rock classes from cluster analysis (right track) for Well A. Note the high proportion of cluster 7 (red) in the upper stage, and the predominance of cluster 5 (orange) in the lower stage with high production, both highlighted by the black boxes.

- The trajectories are parallel to the direction of the minimum horizontal stress interpreted for the study area.
- The lengths shown are approximately 1,000 m, which is the typical length of a Vaca Muerta horizontal well (Atkins, 2014).

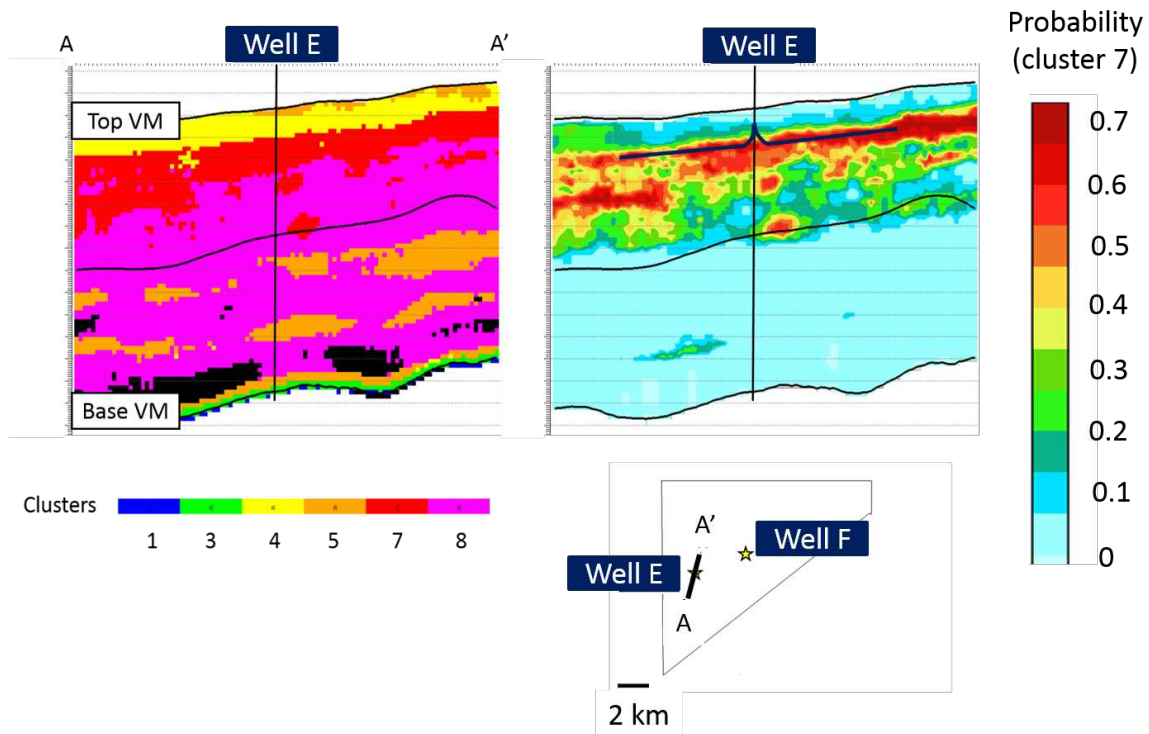


Figure 5.19: Left: arbitrary line of most probable rock class intersecting Well E, aligned with the interpreted minimum horizontal stress direction. Right: probability of rock class 7, with proposed well trajectories in dark blue.

Due to the large thickness of the Vaca Muerta, it is perhaps insufficient to land horizontal wells in only one level. The whole interval, which has excellent reservoir rock for the most part, will likely not get stimulated efficiently. Another alternative for hydraulic stimulation of the Vaca Muerta, which is proving to be efficient for this play, is slant wells. This strategy allows accessing the multiple good rock quality intervals found, at a lower cost than horizontal wells.

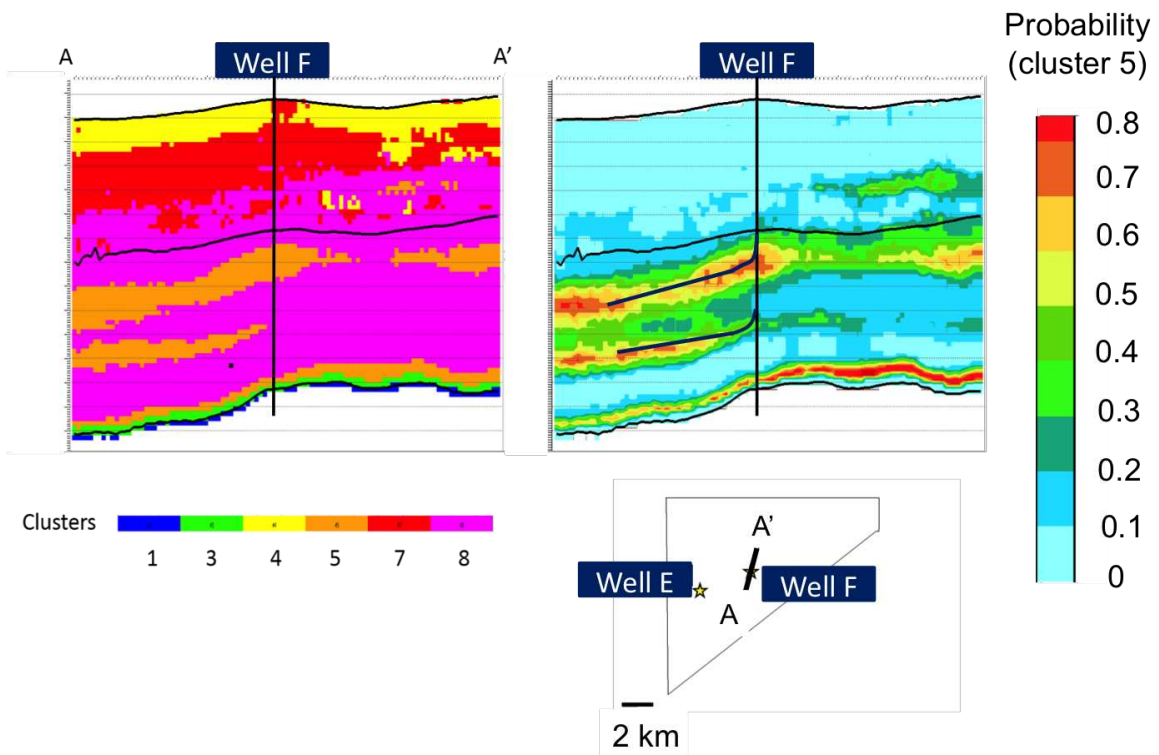


Figure 5.20: Left: arbitrary line of most probable rock class intersecting Well F, aligned with the interpreted minimum horizontal stress direction. Right: probability of rock class 5, with proposed well trajectories in dark blue.

## CHAPTER 6

### CONCLUSIONS AND RECOMMENDATIONS

The Vaca Muerta project has provided RCP with a unique opportunity to investigate a world-class unconventional reservoir from the beginning of the life of a field. A comprehensive workflow has been presented, that shows the value of using a narrow-azimuth, regional P-wave seismic volume with sparse well control, and integrating it with high-quality data from wireline logs and cuttings, to generate a rock property model that incorporates and quantifies the uncertainties inherent at this stage. This workflow is applicable in other frontier shale plays around the world, where reducing risk is vital given the limited data available.

The work presented in this thesis lays the groundwork for a continuing reservoir characterization effort that in time should help optimize completion strategies and improve overall field development.

From this study, the following conclusions can be drawn:

- In the absence of wide-azimuth data, inversion for elastic properties remains the best tool for seismic reservoir characterization in shale plays. The inversion results were successful, with low seismic-synthetic residuals and high correlation with the well logs for the whole area, except in the southwestern portion of the study area.
- Both post-stack and pre-stack derived P-impedance results yield similar low RMS errors from blind well tests. The excellent quality of post-stack acoustic impedance suggests that it can be used to monitor changes in properties such as pore pressure, if time-lapse seismic data were to be acquired.
- The choice of inversion algorithm (model-based or CSSI) does not have a relevant impact in the estimation of geomechanical properties from seismic inversion, but the low-frequency model does. In this case, a simple model gives better predictability away

from the wells. A more complex LFM using the workflow presented in this thesis could be beneficial once more wells are drilled and a better geological model of the reservoir is available.

- In a VTI medium such as the Vaca Muerta, an isotropic inversion gives a good approximation to the anisotropic AVA character of the reservoir, because of the small contrast in Thomsen parameters within the Vaca Muerta. An exception is found at the interface between the Lower Vaca Muerta and the Tordillo sandstone, where simple AVA modeling shows an overestimation of  $V_p/V_s$  ratio by 10% or more. Hence, care should be taken when interpreting the inversion results in the Lower Vaca Muerta.
- The mineralogy and TOC have a high correlation with the patterns observed in the mechanical clusters, suggesting that rock composition has a strong influence on the geomechanical behavior of the Vaca Muerta.
- Rock physics modeling shows that effective stress is a major factor in the velocity trends in the reservoir. Pore pressure calculations confirm that the Vaca Muerta is overpressured, but no clear correlation was found between pore pressure and mechanical stratigraphy.
- The inversion results are interpreted using Bayesian probability and joint PDF's for a quantitative measure of uncertainty. Clusters 5 and 7 were found to show potential as horizontal drilling targets, and tentative landing zones for horizontal wells were proposed based on these rock classes and the probabilistic interpretation of the seismic inversion volumes.

## 6.1 Recommendations for future research

Multiple avenues for future work are available, or will become available as new data are acquired:

- The deterministic inversion can be updated incorporating data from the two new vertical wells. In doing so, uncertainty in the area of interest to the northeast should be significantly reduced. On the other hand, commercial tools are becoming available that do not rely on the low-frequency model (e.g., Ikon Science's Ji-Fi® inversion).
- A detailed sequence stratigraphic interpretation is necessary to assess the relationship between the elastic properties from seismic inversion and the sequence geometry and position of the prograding clinoforms.
- The FFP work is a basic estimate of uncertainty. This work can be extended into a geostatistical inversion using Jason™ software's RockMod module. Moving into stochastic space will allow for a full measure of uncertainty and increased vertical resolution for the reservoir model.
- A more comprehensive petrophysical model should be developed, using advanced tools such as Techlog™ Quanti-Elan. The model should not only incorporate improved values for mineralogy and TOC, but also porosities and fluid saturations. This work will help enhance the rock physics modelling linking elastic properties with reservoir parameters.
- Overpressure is a major driver of productivity in the Vaca Muerta. More detailed work on pore pressure prediction is necessary. In this study, the top of overpressure has been interpreted in a vertical sense using the well logs. Future studies should aim to map the lateral extent of the over-pressured zones using seismic data.
- The pressure seals and seal capacity of the Quintuco and its implications in the stress state of the Vaca Muerta need to be investigated and modelled.
- A feasibility study of the possible value of acquiring multi-component data is a must. Also, rock physics modelling to assess the value of time-lapse seismic should be conducted. The well log data and the pre-stack inversion of P-wave seismic data has shown subtle differences in  $V_p/V_s$  ratio. Multi-component seismic can help improve

the  $V_p/V_s$  estimation through converted-wave, shear wave, or joint inversion. On the other hand, well log data has shown small anisotropy in S-wave velocity. Anisotropy in shear wave pre-stack amplitudes might be present, however. This type of analysis from multi-component data can help characterize fracture density at the seismic scale.

- In the case that time-lapse and/or multi-component seismic are not economically justifiable, a wide azimuth, long-offset modern P-wave seismic dataset should be acquired in the study area. The azimuthal variations in P-wave velocities and/or amplitudes will help understand the horizontal in-situ stress anisotropy, or lack thereof. Azimuthal seismic inversion could also be performed in this dataset. Additional to stress and fractures, anisotropy in rock strength and geomechanical properties can be derived from this analysis, which can have a big impact on well planing and completion design.
- Integration of surface seismic with image logs, core, VSP, and microseismic data when it becomes available will be instrumental for field development as the project moves forward.

## REFERENCES CITED

- Aki, K., and P. Richards (2002), *Quantitative seismology*, 2nd ed., University Science Books.
- Askenazi, A., P. Biscayart, M. Caneva, S. Montenegro, and M. Moreno (2013), Analogía entre la Formación Vaca Muerta y Shale Gas / Oil Plays de EEUU, *Society of Petroleum Engineers, Argentine Section*(Young Professionals Committee).
- Atkins, L. (2014), Argentina's Vaca Muerta shale, <http://www.epmag.com/argentinas-vaca-muerta-shale-718661>, accessed October 13, 2015.
- Badessich, M., and V. Berrios (2012), Integrated Dynamic Flow Analysis To Characterize an Unconventional Reservoir in Argentina: The Loma La Lata Case, in *SPE Annual Technical Conference and Exhibition, San Antonio, Texas, 8-10 October*, SPE 156163, doi:10.2118/156163-MS.
- Bishop, K. (2015), Mechanical stratigraphy of the Vaca Muerta Formation, Neuquen Basin, Argentina, Master's thesis, Colorado School of Mines.
- Bowers, G. (1995), Pore Pressure Estimation from Velocity Data: Accounting for Overpressure Mechanisms Besides Undercompaction, *SPE Drilling and Completion*, 10(2), 89–95.
- Chopra, S., and K. J. Marfurt (2007), *Seismic attributes for prospect identification and reservoir characterization*, Geophysical Development Series No. 11, Society of Exploration Geophysicists, Tulsa, Oklahoma, doi:10.1190/1.9781560801900.
- Chopra, S., K. J. Marfurt, and S. Misra (2011), Acquisition Footprint Removal for Better Fault and Curvature Attributes, *Search and Discovery*, 40719.
- Close, D., M. Perez, B. Goodway, and G. Purdue (2012), Integrated workflows for shale gas and case study results for the Horn River Basin, British Columbia, Canada, *The Leading Edge*, 31(5), 556–569, doi:10.1190/tle31050556.1.
- Dueñas, C. (2014), Understanding rock quality heterogeneity of Montney shale reservoir, Pouce Coupe Field, Alberta, Canada, Master's thesis, Colorado School of Mines, doi: 10.1007/s13398-014-0173-7.2.
- Eaton, B. (1975), The equation for geopressure prediction from well logs, in *Fall Meeting of the SPE of AIME, Dallas, Texas, 28 September-1 October*, SPE 5544.

- EIA/ARI (2013), World Shale Gas and Shale Oil Resource Assessment, *Tech. rep.*, U.S. Energy Information Administration.
- Ejofodomi, E. A., G. D. Cavazzoli, J. Estrada, and J. Peano (2013), Investigating the Critical Geological and Completion Parameters That Impact Production Performance, in *Unconventional Resources Technology Conference, Denver, Colorado, 12-14 August*, URTeC 1576608, pp. 669–679, doi:10.1190/urtec2013-070.
- Ejofodomi, E. A., R. A. Varela, G. Cavazzoli, E. I. Velez, and J. Peano (2014), Development of an Optimized Completion Strategy in the Vaca Muerta Shale with an Anisotropic Geomechanical Model, in *SPE/EAGE European Unconventional Conference and Exhibition, Vienna, Austria, 25-27 February*, SPE 167806.
- Garcia, M. N., F. Sorenson, J. C. Bonapace, F. Motta, C. Bajuk, and H. Stockman (2013), Vaca Muerta Shale Reservoir Characterization and Description: The Starting Point for Development of a Shale Play with Very Good Possibilities for a Successful Project, in *Unconventional Resources Technology Conference, Denver, Colorado, 12-14 August*, URTeC 1508336, pp. 863–899, doi:10.1190/urtec2013-090.
- Garcia, M. N., F. Sorenson, H. Stockman, and C. Zavala (2014), Shale and Tight Reservoirs: A Possible Geomechanical Control in the Success of Producing Wells, Neuquen Basin, Argentina, in *SPE/EAGE European Unconventional Conference and Exhibition, Vienna, Austria, 25-27 February*, SPE 167707.
- Goodway, B., M. Perez, J. Varsek, and C. Abaco (2010), Seismic petrophysics and isotropic-anisotropic AVO methods for unconventional gas exploration, *The Leading Edge*, 29(12), 1500–1508.
- Herrero, F., L. Maschio, and S. Maria (2014), Production Analysis and Forecasting of Vaca Muerta Shale in Argentina: Case History-Based Approach, in *Unconventional Resources Technology Conference, Denver, Colorado, 25-27 August*, URTeC 1965548, doi:10.15530/urtec-2014-1965548.
- Herzog, M. (2014), Pore pressure, and the interdependency between lithology, porosity and acoustic log response targeting the Vaca Muerta Formation, Master’s thesis, Colorado School of Mines, doi:10.1007/s13398-014-0173-7.2.
- Hogg, S. (1993), Geology and Hydrocarbon Potential of the Neuquen Basin, *Journal of Petroleum Geology*, 16(4), 383–396, doi:10.1306/0C9B052B-1710-11D7-8645000102C1865D.

- Howell, J. A., E. Schwarz, L. A. Spalletti, and G. D. Veiga (2005), The Neuquen Basin: an overview, in *The Neuquen Basin, Argentina: A Case Study in Sequence Stratigraphy and Basin Dynamics*, vol. 1, edited by G. Veiga, L. Spalletti, J. Howell, and E. Schwarz, pp. 1–14, The Geological Society of London, Special Publications, London.
- Hurley, N., H. Tanner, and C. Barcat (1995), Unconformity-related porosity development in the Quintuco Formation (Lower Cretaceous), Neuquen Basin, Argentina, in *Unconformities and Porosity in Carbonate Strata: AAPG Memoir 63*, edited by D. Budd, A. Salle, and P. Harris, pp. 159–175, American Association of Petroleum Geologists, Tulsa, Oklahoma.
- Keys, R., and D. Foster (1998), *Comparison of Seismic Inversion Methods on a Single Real Data Set*, Society of Exploration Geophysicists, Tulsa, Oklahoma, doi:doi:10.1190/1.9781560802082.
- Kietzmann, D. A., R. M. Palma, A. C. Riccardi, J. Martín-Chivelet, and J. López-Gómez (2014), Sedimentology and sequence stratigraphy of a Tithonian–Valanginian carbonate ramp (Vaca Muerta Formation): A misunderstood exceptional source rock in the Southern Mendoza area of the Neuquen Basin, Argentina, *Sedimentary Geology*, 302, 64–86, doi: 10.1016/j.sedgeo.2014.01.002.
- Kosset, T. (2014), Wellbore integrity analysis for wellpath optimization and drilling risks reduction: the Vaca Muerta Formation in Neuquen Basin, Master’s thesis, Colorado School of Mines, doi:10.1007/s13398-014-0173-7.2.
- Latimer, R. B., R. Davidson, and P. van Riel (2000), An interpreter’s guide to understanding and working with seismic-derived acoustic impedance data, *The Leading Edge*, 19(3), 242–256, doi:10.1190/1.1438580.
- Legarreta, L., and M. Uliana (1991), Jurassic-Cretaceous marine oscillations and geometry of back-arc basin fill, central Argentine Andes, in *Sedimentation, Tectonics and Eustasy*, edited by D. McDonald, International Association of Sedimentologists Special Publication.
- Legarreta, L., and H. J. Villar (2011), Geological and Geochemical Keys of the Potential Shale Resources, Argentina Basins, *Search and Discovery*, 80196.
- MacFarlane, T. (2014), Amplitude inversion of fast and slow converted waves for fracture characterization of the Montney Formation in Pouce Coupe Field, Alberta, Canada, Master’s thesis, Colorado School of Mines, doi:10.1007/s13398-014-0173-7.2.
- Mallick, S., and P. Ng (1995), A comparison of poststack and prestack inversion of seismic data, in *SEG Annual Meeting, Houston, Texas, 8-13 October*, pp. 651–654.
- Martins, L. M. R. (2013), From OBC seismic to porosity volume: a pre-stack analysis of a turbidite reservoir, deepwater Campos Basin, Brazil, Master’s thesis, Colorado School of Mines.

- Mavko, G., T. Mujerki, and J. Dvorkin (2009), *The Rock Physics Handbook*, Cambridge University Press, New York, doi:10.1007/s13398-014-0173-7.2.
- Monti, L., M. Suarez, L. Vega Velasquez, and anthony robert Thompson (2013), Modeling Vertical Multifractured Wells in Vaca Muerta Shale Oil Play, Argentina, in *SPE Unconventional Resources Conference, The Woodlands, Texas, 10-12 April*, SPE 164537, doi:http://dx.doi.org/10.2118/164537-MS.
- Ouenes, A. (2012), Seismically Driven Characterization of Unconventional Shale Plays, *CSEG Recorder*, 2(February), 18–24.
- Pendrel, J. (2015), Low frequency models for seismic inversions: strategies for success, in *SEG Annual Meeting, New Orleans, Louisiana, 18-23 October*, pp. 2703–2707.
- Rüger, A. (2002), *Reflection Coefficients and Azimuthal AVO Analysis in Anisotropic Media*, Society of Exploration Geophysicists, Tulsa, Oklahoma.
- Russell, B. (1988), *Introduction to Seismic Inversion Methods*, Course Notes Series; No. 2, Society of Exploration Geophysicists, Tulsa, Oklahoma, doi:10.1190/1.9781560802303.
- Russell, B. H. (2014), Prestack seismic amplitude analysis: An integrated overview, *Interpretation*, 2(2), 19–36, doi:10.1190/INT-2013-0122.1.
- Sagasti, G., M. Foster, D. E. Hryb, A. Ortiz, and V. Lazzari (2014), Understanding Geological Heterogeneity to Customize Field Development: An Example from the Vaca Muerta Unconventional Play, Argentina, in *Unconventional Resources Technology Conference, Denver, Colorado, 25-27 August*, URTEC 1923357, doi:10.15530/urtec-2014-1923357.
- Schmoker, J., and T. Hester (1983), Organic carbon in Bakken Formation, United States portion of the Williston Basin, *AAPG Bulletin*, 67, 2165–2174.
- Sharma, R. K., and S. Chopra (2012), New attribute for determination of lithology and brittleness, in *SEG Annual Meeting, Las Vegas, Nevada, 4-9 November*, pp. 1–5, doi:10.1190/segam2012-1389.1.
- Sheriff, R. (2002), *Encyclopedic Dictionary of Applied Geophysics*, 4th ed., Society of Exploration Geophysicists, Tulsa, Oklahoma.
- Steiber, R. (1973), Optimization of shale volumes in open hole logs, *Journal of Petroleum Technology*, 31, 142–162.
- Suarez-Rivera, R., and T. Bratton (2012), Estimating horizontal stress from three-dimensional anisotropy, US Patent No. 8,175,807 B2.

- Suarez-Rivera, R., G. V. Dahl, H. G. Borgos, D. R. Paddock, and D. Handwerger (2013), Seismic-Based Heterogeneous Earth Model Improves Mapping Reservoir Quality and Completion Quality in Tight Shales, in *SPE Unconventional Resources Conference, The Woodlands, Texas, 10-12 April*, SPE 164544.
- Thomsen, L. (1986), Weak elastic anisotropy, *Geophysics*, 51(10), 1954–1966, doi:10.1190/1.1442051.
- Truman Holcombe, H., T. Hong, B. Zhao, E. Salguero, J. Hallin, M. Wallace, S. Chi, M. E. Muzzio, and E. Zunino (2014), Integrated seismic reservoir characterization of Vaca Muerta shale, in *SEG Annual Meeting, Denver, Colorado, 26-31 October*, pp. 2392–2396.
- Urien, C. M., and J. J. Zambrano (1994), Petroleum Systems in the Neuquen Basin, Argentina, in *The petroleum system - from source to trap: AAPG Memoir 60*, edited by L. Magoon and W. Dow, pp. 513–534, American Association of Petroleum Geologists, Tulsa, Oklahoma.
- Vega, A. (2012), Time-lapse density prediction for reservoir characterization using probabilistic neural networks at Postle Field, Texas County, Oklahoma, Master's thesis, Colorado School of Mines, doi:10.1007/s13398-014-0173-7.2.
- Vernik, L., and J. Milovac (2011), Rock physics of organic shales, *The Leading Edge*, 30(3), 318–323.
- Willis, M. (2013), Upscaling anisotropic geomechanical properties using Backus averaging and petrophysical clusters in the Vaca Muerta Formation, Master's thesis, Colorado School of Mines, doi:10.1007/s13398-014-0173-7.2.
- Xu, S., and M. Payne (2009), Modeling elastic properties in carbonate rocks, *The Leading Edge*, 8(1), 66–74.
- Yilmaz, Ö. (2001), *Seismic Data Analysis: Processing, Inversion and Interpretation of Seismic Data*, vol. 1, Society of Exploration Geophysicists, Tulsa, Oklahoma.
- Yrigoyen, M. (1993), The history of hydrocarbon exploration and production in Argentina, *Journal of Petroleum Geology*, 16(4), 371–382, doi:10.1306/bf9ab72b-0eb6-11d7-8643000102c1865d.
- Zunino, J., and J. Soldo (2014), Rock Mechanics template In a Shale Oil Play, Vaca Muerta Fm, Argentina and Their Impact in the Exploratory Strategy, in *EAGE Conference and Exhibition, Amsterdam, The Netherlands, 16-19 June*.